Nanobubbles in Bulk

Muidh Hamed Alheshibri

May 2019

A thesis submitted for the degree of Doctor of Philosophy in Physics

Research School of Physics and Engineering

The Australian National University

Australian National University

Declaration

This thesis is an account of my own original research work, undertaken between March 2015 and May 2019 at the Department of Applied Mathematics in the Research School of Physics and Engineering at the Australian National University.

To the best of my knowledge, this thesis contains no material previously published or written by another person, except where due reference is made in the text.

Muidh Alheshibri
May 2019

Acknowledgement

First and foremost, I am greatly thankful to my supervisor Professor Vincent Craig for his support, enthusiasm, and encouragement throughout my PhD studies. This thesis would have not been completed without his guidance, critical comments, and fruitful ideas. Working in his group has been a rewarding experience and I am eternally grateful to him for this opportunity.

I would also like to thank the Imam Abdulrahman Bin Faisal University and the Saudi Arabian Cultural Mission for the financial support I have received from them during my PhD studies.

I am grateful to Mr. Tim Sawkins at the Department of Applied Mathematics for his contribution in designing the external pressure apparatus presented in this thesis.

I am also grateful to Dr. Victoria Coleman of the Nanometrology group in the Australian National Measurement Institute for access to Archimedes apparatus and assistance during early stages of this project.

I would like to further extend my thanks to my fellow students and post-docs including Marie Jehannin, Namsoon Eom, Virginia Mazzini, Matthew Quinn, Zhu Xiaolong, Jane Qian and E-Jen Teh.

Finally, and most importantly thank you to my mother (Fatima Alotaibi) and my father (Hamed Alheshibri) for their unconditional love and support throughout my life. Words cannot adequately express my gratitude for what you have done for me. Thank you for everything. Thank you to my wife (Maha) who has sacrificed so much for me. Thank you for being on my side at all times. Thank you to my brothers (Jamal, Mansour, Turki, and Bander) for their endless support.

Abstract

Currently, the existence of long-lived sub-micron bubbles in solution is not widely accepted as they should dissolve on a timescale of 1-100 microseconds, calculated through the use of a widely accepted theory of bubble dissolution. Despite this, bulk nanobubbles are reported to have applications in different fields, such as water treatment and remediation, seed germination, surface cleaning, froth flotation, and ultrasound imaging. It is therefore important to develop methods to test if nanoparticle dispersions contain nanobubbles.

Here, two methods are developed that are able to distinguish long-lived nanobubbles from nanoparticles. Firstly, the mean particle density of nanoparticles in a dispersion is determined. Secondly, the influence of external pressure on the size of nanoparticle dispersions is measured. As the density and compressibility of a gas are very different to the density and compressibility of liquids and solids, these methods can differentiate between nanobubbles and other nanoparticles.

The first part of my thesis focuses on nanobubbles that are armoured with a coating of insoluble surfactants. A novel technique for particle characterization that has the ability to distinguish positively buoyant particles (less dense than the solvent) from negatively buoyant particles (more dense than the solvent) was adapted to assess the density of nanoparticles. It revealed a significant population of lipid-coated gas nanobubbles in a commercial ultrasound contrast agent. These nanobubbles are proven to be gas entities by their response to application of pressure. These armoured nanobubbles have a complex response to the application of pressure due to the robust shell formed by the insoluble surfactants. The temperature at which the gas filled nanobubbles condenses to liquid filled nanodroplets is shifted to lower temperature, corresponding to a condensation at higher pressure due to the mechanical resistance of the lipid

shell, which shields the bubble contents from some of the external pressure up to ~ 0.8 atm. The presence of lipids of low solubility at the nanobubble-solution interface effectively results in a negative Laplace pressure, which stabilizes these nanobubbles against dissolution.

Having developed protocols that can be used to demonstrate the existence of bulk nanobubbles, these methods were then applied to different systems reported to contain nanobubbles. These include nanoparticles produced by mechanical means, the mixing of ethanol and water and nitrogen supersaturation by chemical reaction. It was confirmed that nanoparticles were produced in these systems. However, the measured density of these nanoparticles was inconsistent with the nanoparticles being gas filled. Furthermore, the external pressure had only a minimal effect on the size of these nanoparticles. These experiments reveal that processes that lead to bubble formation can produce nanoparticles that result from the accumulation of material at the interface of the dissolving bubbles.

The results of this study demonstrate that the candidate nanoparticles investigated here are not nanobubbles unless they are coated with insoluble materials and casts doubt on many reports of long-lived nanobubbles in bulk. Many researchers have reported the production of stable long-lived nanobubbles in bulk without providing direct evidence that the nanoparticles being measured are indeed nanobubbles. It is recommended that the methods developed here be used as tests to determine if candidate nanoparticles are nanobubbles.

Publications and Presentations

Publications included as part of this thesis

1- **M. Alheshibri**, J. Qian, M. Jehannin, V.S.J. Craig, A History of Nanobubbles, Langmuir. 32 (2016) 11086–11100. doi:10.1021/acs.langmuir.6b02489.

2- **M. Alheshibri**, V.S.J. Craig, Differentiating Between Nanoparticles and Nanobubbles by Evaluation of the Compressibility and Density of Nanoparticles, J. Phys. Chem. C. 122 (2018) 21998–22007. doi:10.1021/acs.jpcc.8b07174.

3- **M. Alheshibri**, V.S.J. Craig, Armoured nanobubbles; ultrasound contrast agents under pressure, J. Colloid Interface Sci. 537 (2019) 123–131. doi:10.1016/j.jcis.2018.10.108.

4- **M. Alheshibri**, V.S.J. Craig, Generation of nanoparticles upon mixing ethanol and water; Nanobubbles or Not?, J. Colloid Interface Sci. 542 (2019) 136–143. doi:10.1016/J.JCIS.2019.01.134.

5- **M. Alheshibri**, M. Jehannin, V. Coleman, V.S.J. Craig, Does Gas Supersaturation by a Chemical Reaction Produce Bulk Nanobubbles?, J. Colloid Interface Sci. 554 (2019) 388–395. doi: 10.1016/j.jcis.2019.07.016.

Publications not included as part of this thesis

1- J. Zhu, H. An, **M. Alheshibri**, L. Liu, P.M.J. Terpstra, G. Liu, V.S.J. Craig, Cleaning with Bulk Nanobubbles, Langmuir. 32 (2016) 11203–11211. doi:10.1021/acs.langmuir.6b01004.

2- **M.H. Alheshibri**, N.G. Rogers, A.D. Sommers, K.F. Eid, Spontaneous movement of water droplets on patterned Cu and Al surfaces with wedge-shaped gradients, Appl. Phys. Lett. 102 (2013) 174103. doi:10.1063/1.4802926.

Oral Conference Presentations

1- **M. Alheshibri** and V.S.J. Craig. "The Puzzling Existence of Nanobubbles in Aqueous Solution". The 8th Biennial Australian Colloid Interface Symposium 2017. Coffs Harbour, NSW, Australia.

2- **M. Alheshibri** and V.S.J. Craig. "Novel Approaches for the Characterization of Bulk Nanobubbles: A Step towards Solving the Puzzling Existence of Nanobubbles in Aqueous Solution ". The 31st Australian colloid and surface science student conference 2018. Warrnambool, Victoria, Australia.

3- **M. Alheshibri** and V.S.J. Craig. "Novel Approaches for the Characterization of Bulk Nanobubbles: A Step towards Solving the Puzzling Existence of Nanobubbles in Aqueous Solution ". Conference on Nanobubbles, Nanodroplets and Their Applications 2018. Suzhou, China.

Table of Contents

List of Symbols and Abbreviation

r	radius
x	distance
μ	chemical potential
P	pressure
γ	surface tension
C	concentration of dissolved gas
K_H	Henry's law constant
T	temperature
ρ	density
f	ratio of the dissolved gas over the saturation concentration
D	diffusion coefficient
t	time
R	ideal gas constant
U_T	terminal rise velocity
g	acceleration due to gravity
v	Brownian velocity
k_B	Boltzmann constant
η	viscosity

$G(\tau)$	correlation function
τ	delay time
q	magnitude of the scattering vector
n_D	refractive index
Δf	frequency shift
m_B	buoyant mass
S_r	sensitivity of the Archimedes resonator
m	dry mass
ρ_f	density of fluid
ρ_p	density of the suspended particles
d	diameter
P_{ext}	external pressure
P_{total}	total pressure inside a nanobubble
n	number of moles
L_{mass}	lower limit of mass detection
d_{min}	size of the smallest detectable particle
E`	Arrhenius activation energy
A	frequency factor
S	solubility
Π	surface pressure
DLS	Dynamic Light Scattering

NTA	Nanoparticle Tracking Analysis
RMM	Resonant Mass Measurement
z-average	Intensity weighted mean diameter obtained from DLS measurements

Chapter 1 Introduction

Most of the material in this chapter is reproduced with major changes from:

M. Alheshibri, J. Qian, M. Jehannin, V.S.J. Craig, A History of Nanobubbles, Langmuir. 32 (2016) 11086–11100. doi:10.1021/acs.langmuir.6b02489.

1.1 Introduction to Bulk Nanobubbles

Bulk Nanobubbles are gas-filled bubbles with dimensions in the submicron range that are moving freely in solution. They are of particular interest, as they are expected to dissolve over a timescale of 1–100 μs , as dictated by the classical theory of bubble dissolution[1,2]. Despite this, they are being applied in different fields, such as ultrasound imaging[3–8], therapeutic drug delivery [6,9–11], water remediation[12–17], froth flotation[18–29], plant growth and seed germination[30–37], surface cleaning[38], and in fuels[39,40]. The formulations used in ultrasound contrast agents and therapeutic drug delivery typically employ a gas of very low solubility (e.g., fluorocarbon) and include a range of lipids and other surface-active materials to stabilize the bubbles. Thus, the nanobubbles are 'armoured' with a substantial coating of poorly soluble material. Later in this thesis we investigate how this armour contributes to their stability. On the contrary, unarmoured long-lived bulk nanobubbles formed in the absence of added surface-active materials, have been

the subject of multiple reports, which have been motivated by a number of potential applications. For some applications, lifetimes of seconds or minutes will suffice, whilst in some possible applications it is necessary that the nanobubbles survive for hours or days. However, even a few seconds is far longer than their expected lifetime.

The field of bulk nanobubbles has also attracted growing interest from industry. This is reflected in the established ISO standard (ISO/TC281) for fine bubble technologies, which has 9 participating countries and 12 observing members working on the standardization of technologies in industries related to bubbles with typical diameters of less than 100 μm. This includes ultrafine bubbles of diameter less than 1 μm.

The apparent mismatch between the lifetime of unarmoured nanobubbles and their practical and commercial applications has led to scepticism among researchers[41,42], who question their existence. This scepticism also originated from the indirect and inconclusive methods reported in the literature to demonstrate their existence[43–51]. A reliable test that characterizes the constitution of bulk nanobubbles would address the ambiguity in this field and develop a deeper understanding of their formation and stability. This challenge is addressed in this thesis.

If long-lived unarmoured nanobubbles are proven to exist, they are expected to facilitate a fundamental study in colloid science, namely, determination of the electrical potential at the gas–solution interface. The potential at the surface of a particle is often determined from a measure of the mobility of the particle in an electric field, which yields the potential at the slip plane[52]. This is known as the zeta potential. However, the buoyancy of larger bubbles causes significant experimental problems in the measurement of zeta potentials. These could be overcome by using nanobubbles, as the rise velocity of nanobubbles due to buoyancy is very much smaller. Moreover, commercial light scattering instruments now offer the ability to measure the zeta potential as well as the size of nanoparticles, potentially making measurements of the zeta potential on nanobubbles routine. The zeta potential is assumed to be a good relative

measure of the actual surface potential. The ability to easily measure zeta potentials in a wide range of solution conditions will facilitate understanding of how the presence of charge at the air–water interface affects the coalescence of bubbles and how they interact with solid particles or oil droplets. This is important for establishing an essential baseline for practical applications in various fields, such as food processing, purification processes, and foam fractionation[53–56]. Further, there has been intense disagreement[57–61] as to whether the water–air interface at a normal pH has a negative surface charge due to the presence of hydroxide ions[57,58] or a positive surface charge due to the presence of hydronium ions[59,60]. This is a complex problem that has not been resolved yet. The reported long lifetime of nanobubbles (i.e. days)[47,49,62] if it is verified, will enable the evaluation of surface charge as a function of pH in a range of electrolytes to be investigated. This will reveal details of the charging mechanism and enable a deeper understanding of this phenomena.

1.2 Terminology

In this thesis, the term *nanoparticles* is used to refer to any nanosized object in solution, regardless of whether it consists of solid, liquid, or gas. The terms *nanobubbles*, *nanodroplets*, and *solid nanoparticles* are used to refer to nanoparticles consisting specifically of gas, liquid, and solid, respectively. The term *armoured nanobubbles* is used to refer to bubbles of diameter less than 1000 nm that have a coating of surface active molecules that have been purposely added to the solution.

1.3 The Fundamentals of Nanobubbles

1.3.1 Introduction

Creating a bubble is an enjoyable activity that we have all experienced during our childhood. A clear example is blowing air into a liquid using a straw. Here, energy or work input (i.e. pressure) is required to overcome the effect of surface tension and create a bubble. Surface tension is the energy cost of creating new interface per unit area. This energy cost is related to the intermolecular forces that hold liquids together[63,64]. This results in a higher surface tension for liquids with strong intermolecular forces and a lower surface tension for liquids with weak intermolecular forces. The higher the surface tension, the higher the work input (i.e. pressure) required to form a bubble. The overall surface energy of the bubble can be lowered by minimizing the surface area, thus small bubbles form spheres, as a sphere is the shape that has the smallest surface area for a given volume of gas.

When bubbles form in a glass of water, an observer would remark that they are unstable. If the bubble rises to the surface and bursts, then the interfacial area is reduced by the surface area of the bubble. Similarly, when two bubbles coalesce, the overall interfacial area is reduced, and the energy of the system is reduced. Further, squeezing the gas inside the bubble leads to a decrease in size, and a reduction in the surface area is obtained. However, as a bubble gets smaller, the pressure inside the bubble increases. The increase in pressure within a bubble with respect to the immediate surroundings is described by the Young–Laplace equation for a sphere:

$$\Delta P = \frac{2\gamma}{r} \tag{1.1}$$

where, γ is the interfacial tension for the bubble interface and r is the radius of the bubble. A simple derivation of this equation is given in Appendix, §A.1.

The Laplace pressure shown in equation 1.1 is inversely proportional to the size of the bubble, and therefore the smaller the bubble, the higher the pressure. Extremely high pressures are reached at nanoscale sizes. For example, the corresponding internal pressure for nanobubbles in pure water with r = 100 nm is ~1.5 MPa.

The pressure inside the bubble increases the solubility of gas, as stated by Henry's law, wherein the equilibrium concentration, C, of a gas in liquid is proportional to pressure (equation 1.2):

$$C = K_H P \tag{1.2}$$

where K_H is Henry's law constant. If the amount of dissolved gas is equal to the equilibrium level of dissolved gas at temperature T and pressure P, a 100% saturation or "saturation" is obtained. "undersaturation" is obtained when the level of dissolved gas is below 100% and "oversaturation" is when it is above 100%.

The increase in solubility results in diffusion of gas molecules from the bubble to the surrounding media, consequently reducing the bubble radius and further increasing the Laplace pressure. Therefore, the ongoing dissolution process amplifies the driving force for dissolution and leads to the disappearance of bubbles. However, a different scenario is expected when the solution is supersaturated with dissolved gas. If the concentration of gas within the solution is sufficiently high, the direction of gas diffusion will be reversed. In this case gas moves into the bubble causing it to grow. This will reduce the Laplace pressure and thereby reduce the solubility of the gas in the solution surrounding the bubble. Gas will continue to diffuse into the bubble leading to an increase in the size of the bubble, which further lowers the Laplace pressure and solubility of the gas in the solution surrounding the bubble. As a result, the bubble will grow rapidly and rise to the surface due to the increase in buoyancy and then burst and disappear.

The diffusion of gas into or out of a bubble in solution is driven by the difference in chemical potential between the gas molecules inside and outside the bubble. The chemical potential inside the bubble is denoted by $\mu_{Bubble,}$ while the chemical potentials outside the bubble are the chemical potential above the solution μ_{atm} and in the solution μ_{sol} (see Figure 1-1). μ_{sol} is set by the saturation level (eq 1.3), and μ_{atm} is dependent on the external pressure (eq 1.4), while μ_{Bubble} is dependent on the total pressure (the sum of the Laplace pressure and the external pressure) (eq 1.5).

$$\mu_{sol} = \mu^*_{sol} + RT \ln \left(\frac{C}{1M}\right) \tag{1.3}$$

$$\mu_{atm} = \mu^*_0 + RT \ln \left(\frac{P_{ext}}{1\ atm}\right) \tag{1.4}$$

$$\mu_{bubble} = \mu^*_0 + RT \ln \left(\frac{P_{ext} + \Delta P}{1\ atm}\right) \tag{1.5}$$

Where μ^*_{sol} and μ^*_0 are the standard chemical potentials, R is the ideal gas constant, T is the temperature, P_{ext} is the external pressure and ΔP is the Laplace pressure and C is the concentration of dissolved gas.

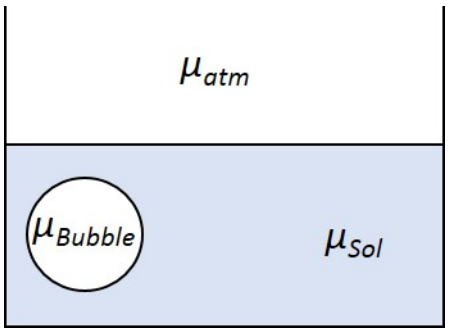

Figure 1-1. Schematic diagram of chemical potentials of the gas inside and outside a bubble in solution.

At 100% saturation, the chemical potential of the dissolved gas in the bulk solution and in the gas above the solution are equivalent. Therefore

$$\mu_{atm} = \mu_{sol} \tag{1.6}$$

Whenever there is a Laplace pressure acting on the bubble, the pressure inside the bubble is greater than the pressure in the surrounding solution and the chemical potential of the gas molecules inside the bubble will be higher than in the gas above the solution. Thus

$$\mu_{Bubble} \neq \mu_{atm} \tag{1.7}$$

unless the Laplace pressure is zero.

So μ_{Bubble} can be in equilibrium with μ_{sol} only if the solution is supersaturated with respect to the external pressure. Thus, the chemical potential for the gas inside the bubble can be at equilibrium with the surrounding solution only if the chemical potential of the dissolved gas in the bulk solution is not at equilibrium with the chemical potential in atmosphere; That is, it is not possible to have overall equilibrium unless the Laplace pressure is zero.

Regardless, let's consider a single bubble that is in local equilibrium with the dissolved gas in solution, where

$$\mu_{Bubble} = \mu_{sol} \tag{1.8}$$

The local equilibrium in equation 1.8 requires a critical level of gas supersaturation with respect to the external pressure. The supersaturation level required for bubble stability (calculated using equation 1.1 and equation 1.2) with respect to bubble size is shown in Figure 1-2. However, even if local equilibrium is initially established between a bubble and the solution, a very small deviation will disrupt the equilibrium and cause the bubble to either grow and be removed from the solution through buoyancy or shrink from existence. Thus, this implies that nanobubbles cannot be stable whenever the Laplace pressure is finite.

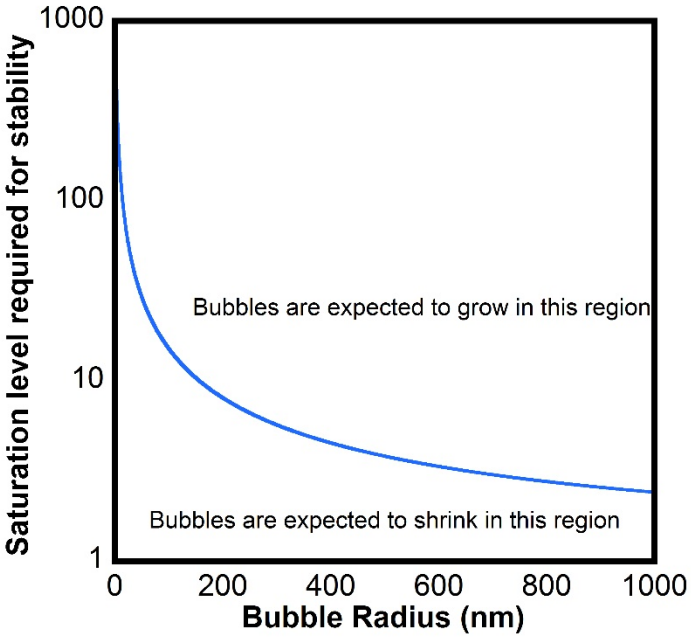

Figure 1-2. Phase diagram of bubble stability based on the Laplace pressure and Henry's Law. Bubbles are expected to shrink if the saturation level is lower than the supersaturation level required for stability or grow if the saturation level is higher. Bubbles on the line are stable, but any fluctuation will disrupt this stability.

1.3.2 Bubble Growth and Dissolution

1.3.2.1 Theory of Bubble Growth and Dissolution

A landmark theory regarding the growth and dissolution of bubbles was proposed in 1950 by Epstein and Plesset[1]. They calculated the diffusion process of gas to and from a bubble. To do so, a number of simplifications were made:

- A single solitary bubble with initial radius (r_0) was assumed to be stationary (not rising due to buoyancy or translating with Brownian motion).
- At initial time $t = 0$, the bubble had already established a steady state with the surrounding solution.

- The motion of the bubble boundary as it grows, or shrinks was ignored. This approximation is valid, as the gas concentration within the bubble is much greater than in the surrounding liquid, and the region surrounding the bubble through which the diffusion takes place is much larger than the bubble itself.

The lifetime of a bubble with a radius *r* was calculated using the diffusion equation for the dissolved gas concentration, *C*, at a point in the solution a large distance, *x,* from the bubble:

$$\frac{\partial C}{\partial t} = D\Delta C \qquad (1.9)$$

where *D* is the diffusion coefficient of the gas at the liquid interface.

To solve for the diffusion, the boundary conditions set for this equation were:

$$C(x,0) = C_i \qquad \text{For } x > r$$

$$\lim_{x\to\infty} C(x,t) = C_i \qquad \text{For } t > 0$$

$$C(r,t) = C_s \qquad \text{For } t > 0$$

These Boundary conditions are:

At time $t = 0$, the concentration of the gas dissolved in the solution is uniform and equal to C_i, and it remains constant at large distances, *x,* from the bubble at time $t > 0$.

The concentration of dissolved gas immediately adjacent to the bubble (C_s) is saturated with respect to the bubble (the pressure being higher in the bubble than in the surrounding solution). Here C_i is the level of the gas in the solution, and C_s is implicitly determined by applying Henry's law (equation 1.2) using the pressure within the bubble.

For a bubble submerged in a solution at a given external pressure and temperature, Epstein and Plesset[1] described the change of radius (r) as a function of time (t) using the general differential equation:

$$\frac{dr}{dt} = \alpha \left[\frac{1}{r} + \frac{1}{(\pi D t)^{\frac{1}{2}}} \right] \qquad (1.10)$$

The coefficient $\alpha = \frac{\mathrm{D}\,(C_i - C_s)}{\rho} = DM(f-1)$, where ρ is the gas density in the bubble. The ratio of the dissolved gas over the saturation concentration is f, and $M = C_s/\rho$.

Here a bubble is expected to shrink when the chemical potential of the gas inside the bubble is greater than the chemical potential of the dissolved gas in the bulk phase and grow when the level of supersaturation is sufficient to raise the chemical potential of the dissolved gas above that in the bubble.

By integrating equation 1.10, the change of size in the shrinking or growing process can be calculated, and the final expression is given in equation[1] 1.11:

$$r(t) \approx \sqrt{{r_0}^2 + 2\alpha\, t} \qquad (1.11)$$

Equation 1.11 represents an approximate solution suitable for larger bubbles, as the increase in the Laplace pressure while the bubble is decreasing was not considered in this equation.

The change in size for a bubble with an initial radius of 100 nm, 500 nm, and 1000 nm were calculated using Equation[1] 1.11 (see Figure 1-3). Here the calculation was done in small time steps and the Laplace pressure and C_s was recalculated at each step to account for the effect of the shrinking radius, allowing for accurate calculations for small bubbles. As shown, the theory predicts that small bubbles will rapidly shrink and disappear in saturated solutions. For example, the lifetime of a bubble of initial radius of 1000 nm is predicted by the Epstein and Plesset theory to be less than 0.02 s. Such bubbles would in most cases dissolve and disappear before they can be detected or measured.

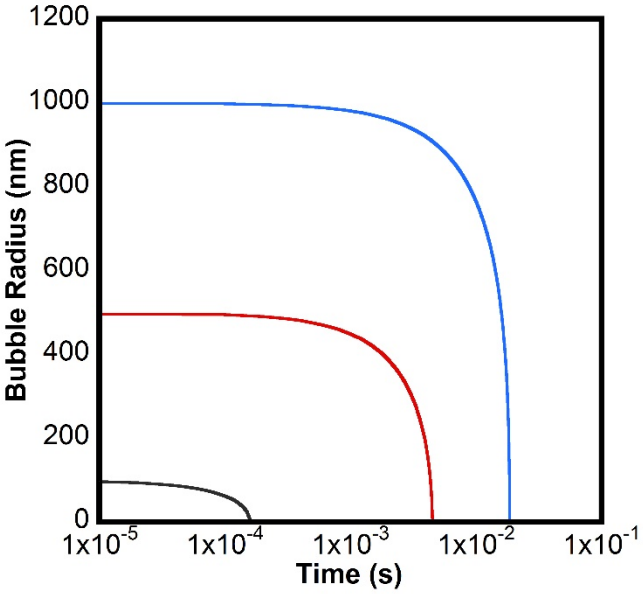

Figure 1-3 Calculated nanobubble radius versus time using the Epstein and Plesset theory[1] for a nitrogen filled nanobubble of initial radius 1000 nm (blue), 500 nm (red), and 100 nm (black) in a solution that is saturated with dissolved nitrogen gas. For this calculation, equation 1.11 was implemented iteratively to take account of the increasing Laplace pressure with decreasing size. The parameters used in this calculation are T = 300 K, γ = 0.072 Jm^{-2}, $D = 2.0 \times 10^{-9}$ m^2 s^{-1}, C_{sat} = 0.6379 moles m^{-3}, and $\rho_{l\ atm}$ = 40.6921 moles m^{-3}.

1.3.2.2 The lifetime of bubbles

In 1997, Ljunggren and Eriksson developed a theory to specifically calculate the Lifetime of bulk nanobubbles[2]. This work was reported in direct response to reports of the existence of surface nanobubbles[65]. Their calculation was in agreement with Epstein and Plesset's theory, and they stated that "bubbles of colloidal size in water have a short lifetime". Their expression for the lifetime for a bubble with initial radius r_0 is given in equation 1.12:

$$t = \frac{K_H r_0^2}{3RTD} \tag{1.12}$$

where t is the lifetime of the bubble, K_H is Henry's law constant, R is the ideal gas constant, T is the temperature, and D is the diffusion constant.

Figure 1-4 shows the expected lifetime for a gas bubble as a function of its initial radius[2] using the Ljunggren and Eriksson model (equation 1.12). It is clearly demonstrated that such a nanoscale bubble will dissolve very quickly. The calculation in Figure 1-4 also considers the effect of the gas type on the lifetime of gas bubbles, where a gas with higher solubility (e.g., CO_2) dissolves more rapidly than a gas with a lower solubility (e.g., O_2, N_2, or H_2).

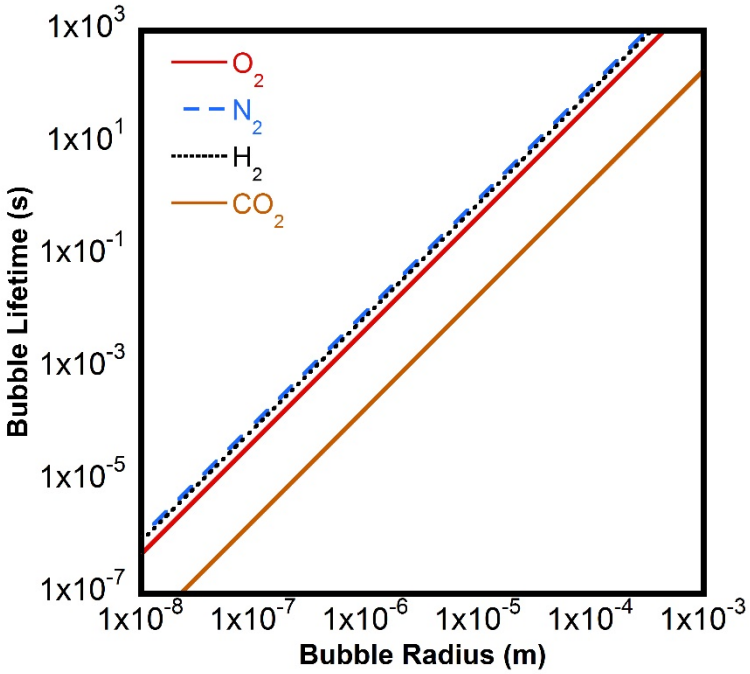

Figure 1-4: Expected lifetime for a bubble in water as a function of the initial radius and gas type using the Ljunggren and Eriksson model (equation 1.12)[2,64]. The parameters used in this calculation are K_H (O_2) = 7.7 $\times 10^4$ J mole^{-1}, K_H (N_2) = 15.6 $\times 10^4$ J mole^{-1}, K_H (H_2) = 13 $\times 10^4$ J mole^{-1}, K_H (CO_2) = 0.3 $\times 10^4$ J mole^{-1}, D = 2.0 $\times$ 10^{-9} m^2 s^{-1}, and T = 298 K.

The findings from Epstein and Plesset and Ljunggren and Eriksson have had a profound influence on nanobubble research, as it has led to reports of long-lived nanobubbles being treated with great caution and dubiosity[1,2].

1.4 Nanobubbles Research

Two types of nanobubbles are reported in the literature. The term *bulk nanobubbles* is used to describe gas filled bubbles in solution that have a diameter less than 1000 nm. *Ultrafine bubbles* is an equivalent term that is also used in the literature. The term *surface nanobubbles* is used to describe gaseous domains attached to surfaces. The height of surface nanobubbles is generally more than 10 nm and less than 100 nm. The radius of the contact line (three-phase line) is generally between 50 and 500 nm. The existence of stable surface nanobubbles has now been established[66,67], although the origin of their stability is still debated[68–74]. However, the focus of this study is bulk nanobubbles and the relationship, if any, between surface and bulk nanobubbles has not be elucidated.

1.4.1 Bulk Nanobubbles

1.4.1.1 Early Reports of Bulk Nanobubbles

Perhaps, the first report of bulk nanobubbles was in 1962 by Sette and Wanderlingh[75]. They demonstrated that high-energy neutrons present in cosmic rays or introduced artificially reduced the sound energy required to initiate cavitation of bulk water. They argued that oxygen recoil nuclei deposit energy that results in the formation of cavitation nuclei which are stabilized by contaminants. Further, they showed that by shielding water from neutrons, the cavitation threshold energy increased over a period of ~5 hours, indicating that the microcavities persisted for at least this long. Later, Hemmingsen[76] studied cavitation in solutions that were supersaturated with gas and found that the supersaturation threshold for cavitation could be increased by prior application of extremely high pressures. This was attributed to the removal of cavitation nuclei in both the bulk and on surfaces by forcing the dissolution of the gas within

the cavities[76]. During the 1990s, Bunkin *et al.*[77–79] reported the existence of stable microbubbles in dilute solutions of electrolytes. These microbubbles were thought to be stabilized by repulsive interactions between ions adsorbed to the interface and provide nuclei for optical cavitation. More details about this mechanism is given in §1.4.1.5.

1.4.1.2 Production and Characterisation of Bulk Nanobubbles

There are several publications on long-lived bulk nanobubbles that have been generated through several techniques. All of these methods rely on the inducement of supersaturation, which could nucleate nanobubbles. These techniques include ultrasonication, electrolysis, solvent exchange, temperature changes and mechanical means.

1.4.1.2.1 Ultrasonication

Kim *et al.* in 2000[43], reported the generation of bulk nanoparticles by sonication (42 kHz, 70W) in the presence of a palladium coated surface, directly in a cuvette placed in a dynamic light scattering (DLS) apparatus. In purified water they produced a bimodal distribution of nanoparticles with peaks around 80 nm and 350 nm. Particles created at pH 3 were slightly larger than particles created at pH 12. The particles were designated to be nanobubbles. The measured zeta potential for the nanoparticles was consistent with reports of the zeta potential measured on larger bubbles[80]. The nanoparticles were stable for at least 60 minutes. In this work, it was not demonstrated that the particles being measured were actually nanobubbles, therefore it is possible that surface cavitation due to ultrasound caused the formation of palladium nanoparticles[81]. However, when the zeta potential was compared to that of palladium nanoparticles[82], it was found to be inconsistent with the particles being palladium. Later work by the same corresponding author, using a different ultrasound frequency (20 kHz) and generator but an otherwise similar method, found that the nanoparticle size increased with ultrasound power and time of application[83]. Particles of 700 nm and larger were produced in

this manner. Ultrasonication has also been used recently by Mo *et al.* [84] to study the generation of bulk nanobubbles[84]. They used nanoparticle tracking analysis to compare the concentration of nanoparticles in i) pure water, ii) water after 1 min ultrasonication and iii) degassed water after ultrasonication. They concluded that the nanoparticles generated by ultrasonication were gas-filled nanobubbles because the concentration of nanoparticles in the water after ultrasonication was higher than the concentration of the nanoparticles in the other two samples. The concentration of the produced nanoparticles was measured to be ~ 7×10^7 particles/ml, which corresponds to less than 5 particles/frame. However, a lower concentration of the particles upon degassing is not necessarily direct evidence of nanobubbles as volatile oil droplets respond to vacuum in a similar way to bubbles[85].

1.4.1.2.2 Electrolysis of Aqueous Electrolyte Solutions

Electrolysis of water evolves gas and supersaturates the solution with hydrogen gas at the cathode and oxygen gas at the anode. Between 2001 and 2009, Kikuchi *et al*. studied the generation of nanobubbles by electrolysis[46,47,86–88]. In the cathodic solution, particles 10 - 600 nm in diameter were detected by Dynamic Light Scattering (DLS) and shown to be stable for at least four hours[87]. In the anodic solution, particles 30 nm in diameter were produced by electrolysis and measured over three days, after which they had increased in size to 250 nm. After five days, particles were no longer detected[47]. According to the authors, the particles in the anodic and cathodic solutions were oxygen and hydrogen nanobubbles, respectively. This work also showed that oxygen contained within the nanoparticles was not detected when using a standard dissolved oxygen meter or the Winkler oxygen titration method. However, if the pH of the solution was reduced by the addition of acid, the Winkler method detected an increase in oxygen concentration, which was attributed to the oxygen liberated from the nanobubbles. In recent work, Postnikov *et al.* [89] used electrolysis to produce and control the size of the nanoparticles by regulating the applied voltage pulses, and claimed the nanoparticles produced

were nanobubbles. The lifetime for these nanoparticles was found to be 15 minutes, which was less than the lifetime for the nanoparticles reported by Kikuchi[47,87]. However, a lifetime of 15 minutes is still much longer than the lifetime expected from the Epstein and Plesset theory[1].

1.4.1.2.3 Mechanical Generation

Another common method that is reported to produce bulk nanobubbles is based on mechanical means[48–51,90–93]. These methods use pressure-cycling techniques where the solution is subject to an increase in pressure to increase the solubility of gas, followed by a reduction in pressure which is expected to result in the formation of bubbles. Many of these techniques also employ gas injection. An example is the study by Ushikubo and his group, who used oxygen gas to produce what they designated to be nanobubble solutions[49]. The average size of the nanoparticles produced was determined to be 137 nm, measured by dynamic light scattering (DLS). The generated nanoparticles were shown to be stable for days, and they attributed their stability to the electric charge at the interface, as the zeta potential was measured to be in the range of -45 mV to -34 mV. In a recent study, Wang *et al*. reported that N_2, O_2 and CO_2 nanobubbles could be produced and maintained stability for at least 24 hours[90]. In this study, they were able to adjust the size of the nanoparticles by adjusting the periodic pressure time interval during generation. They found that the size of the nanoparticles decreased with an increase in the pressure cycling time during generation and assigned these nanoparticles to be nanobubbles. In previous reports, aqueous solutions were used. However, the generation of bulk nanobubbles in organic solvents using mechanical generation has also been reported. Mase *et al.* [91] generated nanoparticles that they claimed to be nanobubbles using a commercial nanobubble generator in organic solvents such as dimethyl sulfoxide, isopropyl alcohol, dimethylformamide, ethanol, methanol, acetonitrile, butyl acetate and hexane. They used nanoparticle tracking analysis to characterise the nanoparticles and observed them in all the

solvents studied, except hexane. They claimed that nanobubbles could be generated mechanically in a range of organic solvents.

1.4.1.2.4 Solvent Exchange

Solvent exchange was first reported in 2000 as a convenient method for producing surface nanobubbles[94]. The process was as follows: the hydrophobic surface was initially immersed in a water-miscible solvent (e.g. ethanol), and then the ethanol was slowly displaced by water. Common atmospheric gases, such as nitrogen and oxygen, have lower solubility in the ethanol-water mixture than prior to mixing. Hence during solvent exchange, supersaturation is occurred and gas precipitates onto the surface, leading to the formation of surface nanobubbles. An *et al*.[95] showed that the saturation level could reach up to 311% upon mixing ethanol and water. This method has been commonly employed to produce surface nanobubbles. Several groups have used solvent mixing to generate bulk nanobubbles[44,96–100]. In a series of publications in 2007, Jin *et al.* [44,96,97] examined aqueous solutions of tetrahydrofuran, ethanol, urea, sugars, surfactants and α-cyclodextrin using dynamic laser light scattering. These measurements, as well as those of other researchers, revealed a 'slow mode' which corresponds to structures ~ 100 nm in diameter. It was found that the slow mode could not be removed by simple filtration through a 20 nm pore-sized filter, but it was gradually removed by numerous repeated filtrations, regardless of the type of solute present. Moreover, the slow mode was restored by the injection of particle-free air. They concluded that the slow mode was a signature of nanobubbles that were stabilized by surface active organic molecules. However, Habich *et al.*[41] and Sedlak *et al*.[101] performed similar experiments using degassed solutions and found that the level of light scattering remained significant. They attributed the scattering to contaminants introduced with the organic solvents or from the vessels holding the solvents rather than to nanobubbles. In contrast to these reports, the nanoparticles generated upon mixing ethanol and water were recently assigned to be nanobubbles[98] or nanobubble-like clusters[99,100]. Qiu *et al*.[98]

generated nanoparticles using ethanol-water mixing. They investigated the effect of the ratio of ethanol to water on the size and concentration of nanoparticles produced as measured by nanoparticle tracking analysis. The maximum concentration of nanoparticles was obtained at 8.3% v/v ethanol solution. Contrary to the works of Habich *et al.* [41], they concluded that these nanoparticles were gas-filled nanobubbles based on their observation of a reduction in the concentration of nanoparticles when mixing degassed solvents.

1.4.1.2.5 Increasing the Temperature of Solution

Najafi *et al.* [45] produced what was claimed to be nanobubbles in a closed cuvette for zeta potential measurement by increasing the temperature. This reduced the solubility of dissolved gases and precipitated nanobubbles, which had a mean size of 290 nm. The measured zeta potentials were consistent with those measured for larger bubbles. Before the temperature change, no scattering was detected. Note a temperature increase leads to an increase in solubility for most materials, particularly candidate contaminants such as hydrocarbons, further supporting their assertion that the nanoparticles were nanobubbles.

1.4.1.3 Additional Methods used to Characterise Bulk Nanobubbles

The above experiments utilized standard techniques for nanoparticle characterization, such as dynamic light scattering, nanoparticle tracking analysis and zeta potential measurements in characterizing nanoparticles. In the following studies, unique techniques have been either developed or implemented to investigate the presence of long-lived bulk nanobubbles.

In 2010, Ohgaki *et al.* [48] employed gas injection of N_2, CH_4 and Ar in water to produce nanobubbles. They claimed extremely high nanobubble concentrations of ~ 10^{13} bubbles per ml that persisted for up to two weeks. Using a well-established technique for biological samples, the nanoparticles were preserved by rapid cryogenic freezing of a droplet, which was subsequently cleaved and coated to form a replica of the surface. The replica was imaged by

scanning electron microscopy, revealing a population of nanoparticles. The images are reproduced in Figure 1-5.

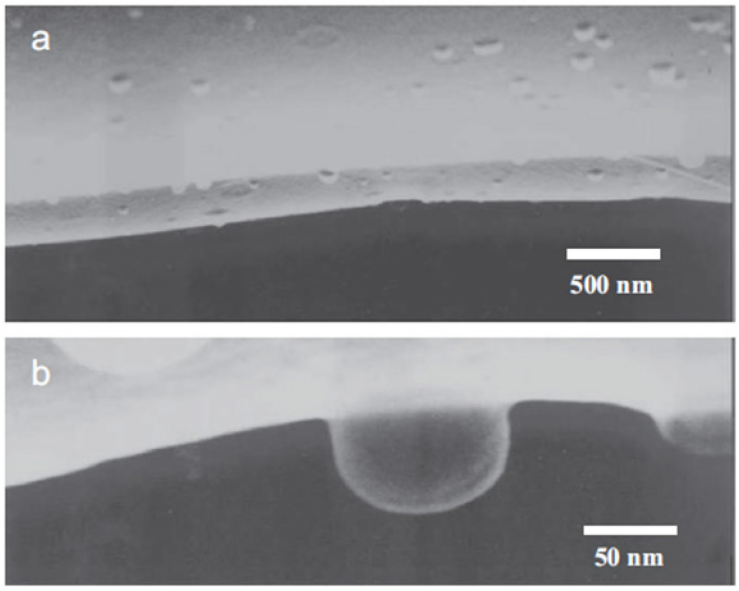

Figure 1-5. Panel A: Scanning electron microscopy image of rapid cryogenic freezing fracture of a solution of nanoparticles that was assigned to be nitrogen nanobubbles with a diameter of ~ 100 nm. Panel B: A higher magnification image of a single nanoparticle. Images are reprinted from [K. Ohgaki, N.Q. Khanh, Y. Joden, A. Tsuji, T. Nakagawa, Physicochemical approach to nanobubble solutions, Chem. Eng. Sci. 65 (2010) 1296–1300. doi:10.1016/j.ces.2009.10.003.] Copyright (2019) with the permission of Elsevier.

In a complementary study, Uchida *et al.* [50] produced nanoparticle solutions by gas injection of ultrapure oxygen. Rapid cryogenic freezing was then used to prepare replicas of the surface of a fractured water droplet, and the resulting replica was imaged by transmission electron microscopy. Nanoparticles ~ 100 nm in size were revealed (see Figure 1-6). In later work, they showed that nanoparticles produced in the same manner increased in size from ~ 400 nm to ~ 750 nm over a period of a week when stored in a sealed bottle[102]. Cryo-EM has been employed to directly image bulk nanobubbles embedded in amorphous ice that was produced by a nitrogen-evolving chemical reaction[103]. A concern is that sample freezing leads to unavoidable perturbation of the sample. It is possible that the observed features are defects induced by the

freezing. Countering this is the extensive use of this technique in biological imaging and the general acceptance of the conclusion that rapid freezing does not generally produce artefacts of this nature.

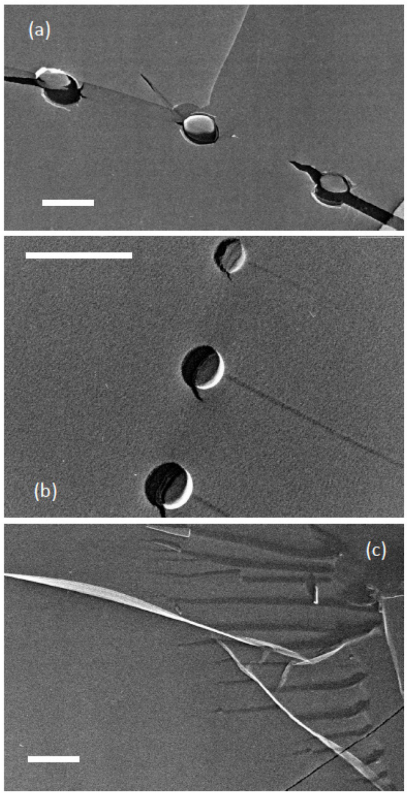

Figure 1-6. Replica transmission electron microscopy images showing spherical objects thought to be O_2 filled nanobubbles with a diameter of ~ 500 nm (a) or 200 nm (b). Panel c shows a control replica sample of pure water. Images are reprinted from [T. Uchida, S. Oshita, M. Ohmori, T. Tsuno, K. Soejima, S. Shinozaki, Y. Take, K. Mitsuda, Transmission electron microscopic observations of nanobubbles and their capture of impurities in wastewater, Nanoscale Res. Lett. 6 (2011) 295. doi:10.1186/1556-276X-6-295] Copyright (2019) with the permission of Springer.

Bunkin *et al.*[104] used a modulation interference microscope to image nanobubbles in sodium chloride solutions. This technique can determine the refractive index of particles with respect to the surrounding medium. The results showed that a silica particle registered a higher refractive index than the surrounding medium, whilst a particle assigned to be a nanobubble

registered a significantly lower refractive index than the surrounding medium. Significantly, unlike most other studies of bulk nanobubbles, the solution was not supersaturated with dissolved gas.

Kobayashi *et al*. were the first to utilize the resonant mass measurement technique in characterizing bulk nanobubbles[51]. An instrument called the Archimedes was used to detect the mass density relative to the solvent of individual nanoparticles as they passed one by one through a microresonator[105]. (The details of this method are reported in §2.3). Measurements on nanoparticles generated by pressure cycling revealed a population of nanoparticles with positively buoyant mass, indicating that they were less dense than the solvent. However, light oil droplets also have a density less than water, and therefore this alone is not sufficient evidence to demonstrate that they are gas filled bubbles.

Oh *et al*.[92] adapted a technique that was previously used on surface nanobubles[66] to investigate the presence of bulk nanobubbles. The infrared spectra of what they attributed to be bulk nanobubbles exhibited a rotational fine structure that was consistent with CO_2 molecules in their gaseous state, whereas their control, CO_2-saturated water exhibited a single peak at 2343 cm^{-1}, indicating the presence of dissolved CO_2. However, there was no direct evidence that the spectra were obtained from the nanobubbles in the bulk of the solution as opposed to surface nanobubbles or larger bubbles. Nirmalkar *et al.* recently used a freeze-thaw technique as a method for differentiating nanobubbles from other nanoparticles[62,106,107]. In their study, they generated nanoparticles that were stable for up to a year, using ultrasound cavitation. They concluded that these were nanobubbles, as these nanoparticles disappeared after the freeze-thaw process. Furthermore, they showed that the addition of surfactant (i.e., SDS) to the nnaoparticles[62] before the freezing process stabilized the nanoparticles, which prevented them from being damaged during the freeze-thaw process. However, the freezing process could have had an impact on the stability of particles, causing them to coalesce and settle if they were dense

nanoparticles or cream out of the solution if they were oil droplets. Significantly they did not investigate the effect of the freeze-thaw treatment on a known nanoparticle sample.

In contrast to the conclusions of all the above studies, Leroy *et al*.[42] have examined solutions treated with a bubble generator for evidence of bulk nanobubbles using ultrasound and found no evidence of bulk nanobubbles. This technique is of interest, as it sensitive to the presence of gas. However, this technique as applied is not sensitive enough to detect the typical reported concentrations of nanobubbles (10^8/mL).

1.4.1.4 Evidence of Bulk Nanobubbles

The above experiments are correctly criticized for a lack of direct evidence that the nanoparticles being observed actually consist of gas. However, a number of experiments provide more direct evidence of long-lived gas filled bulk nanobubbles. Possibly the earliest direct evidence of bulk nanobubbles with diameters less than a micron was reported by Johnson and Cooke in 1981[108]. They reported that bubbles produced by shear in seawater were observed to be stable for long periods (>22 hours) due to the formation of surface films formed from naturally present surfactants. They demonstrated that such encased bubbles were gas-filled, as they expanded when put under tension (negative pressure) and contracted under an applied pressure (see panel 1 in Figure 1-7), and some could even be destroyed by application of positive pressure. As saltwater inhibits bubble coalescence[109–111], the breaking of waves in seawater readily produces large numbers of small bubbles. This study indicated that these bubbles could shrink to form nanobubbles that were stable for up to 24 hours, indicating that the oceanic populations of nanobubbles were likely to be substantial[108]. Similarly, in freshwater with substantial levels of organic material, it would be expected that turbulence due to rapids or waterfalls might also produce significant populations of nanobubbles. In 1984, Yount *et al.* [112] produced gas-filled bubbles in the size range of 200 to 1500 nm, using distilled water and

gelatine. Similar to the work of Johnson and Cooke[108], they showed that the observed objects were gas-filled bubbles that expanded and contracted under the depressurizing and pressurizing process (see panel 2 in Figure 1-7). They pointed out the possibility of forming nanobubbles even in highly purified water.

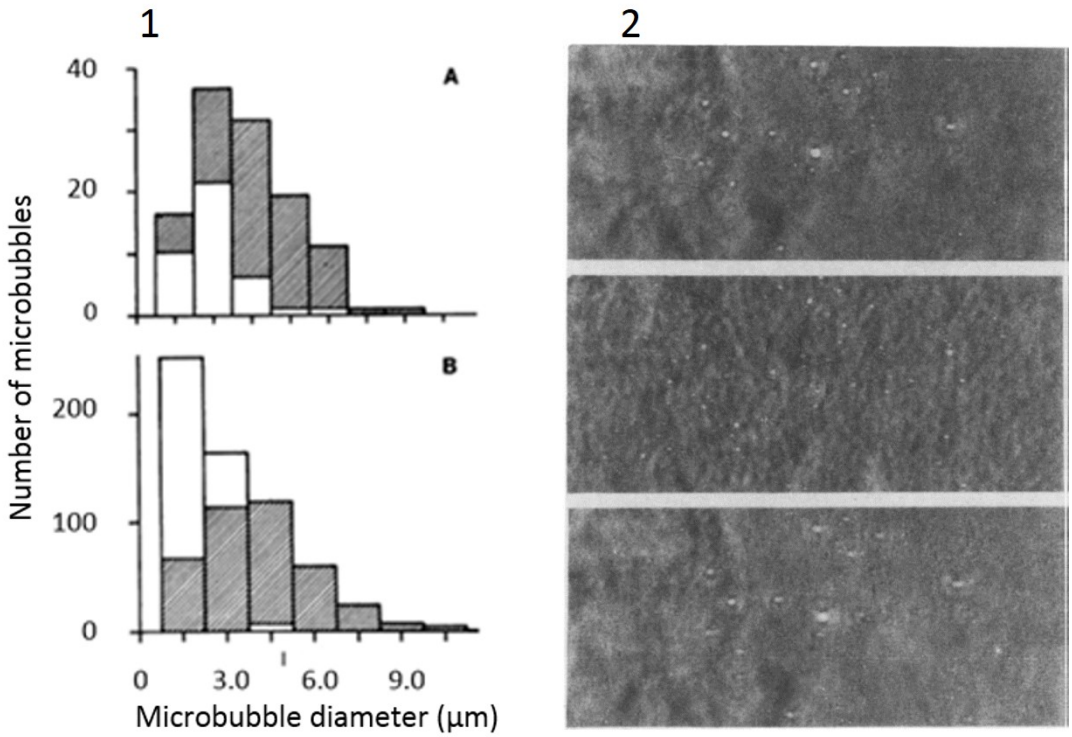

Figure 1-7. Early measurements on the effect of external pressure on the size of small bubbles[108,112]. Panel 1A shows the distribution of bubbles in seawater (shaded region) compared to those subjected to an additional pressure of ~ 0.8 atm (unshaded region). The substantial reduction in bubble size indicates that the surface contamination had reduced the surface tension, and therefore the Laplace pressure, to a low level. Panel 1B shows how an initial bubble distribution (shaded region) shifted to smaller sizes after a period of 22 hours (unshaded region). Panel 2 shows images of bubbles with a size range of 200–1500 nm under the application of negative pressure (i.e., 0.26 atm) (upper and lower images) and under atmospheric pressure (middle image). Images in panel 1 are reprinted from [B.D. Johnson, R.C. Cooke, Generation of stabilized microbubbles in seawater, Science 213 (1981) 209–211. doi:10.1126/science.213.4504.209.] Copyright (2019) with the permission of The American Association for the Advancement of Science, and the images in panel 2 are reproduced from [D.E. Yount, E.W. Gillary, D.C. Hoffman, A microscopic investigation of bubble formation nuclei, J. Acoust. Soc. Am. 76 (1984) 1511–1521. doi:10.1121/1.391434.] Copyright (2019) with the permission of The the Acoustical Society of America.

The strongest evidence for the existence of long-lived nanobubbles comes from their contrast in ultrasound imaging[9,113,114]. Here, bubbles are used to enhance the echo ultrasound signal to improve the contrast during ultrasound imaging. In 2004, Oeffinger and Wheatley employed surfactant stabilized nanobubbles as ultrasound contrast agents[9]. The initial population of surfactant stabilized bubbles was produced by the sonication of a perfluorocarbon gas. This produced a population of bubbles with a mean diameter of > 1 micron. This sample was then centrifuged to promote creaming of the larger bubbles. In doing so, the mean diameter of the dispersion was reduced to ~ 400 nm. The evidence that these objects are indeed nanobubbles is two-fold. Firstly, they were demonstrably less dense than water, as the larger particles creamed more effectively during centrifugation. Secondly, these nanoparticles provide an ultrasound enhancement compared to a control buffer without the nanoparticles. This is consistent with the particles being gas-filled nanobubbles as opposed to oil droplets. In recent work, Hernandez *et al*. produced smaller lipid-stabilized nanobubbles with a mean diameter of 290 nm[115]. Resonant mass measurement was employed in their measurement and showed that these bubbles were less dense than their solvent. The ultrasound contrast enhancement coming from these bubbles was significant, and it was higher than the signal of commercial microbubbles. Additionally, they showed that the number of these nanobubbles decreased significantly after exposing the nanobubbles to high-power ultrasound indicating destruction of the bubbles.

It is notable that all the direct evidence of bulk nanobubbles above is associated with bubbles that were coated with insoluble material, which likely contributed to their stability[68]. In contrast, reports of uncoated bulk nanobubbles remain controversial, and there is no definitive proof of their existence

1.4.1.5 Explanations for the Stability of Unarmoured Bulk Nanobubbles

Although the existence of unarmoured nanobubbles is not yet widely accepted, a number of explanations have been proposed to explain their stability. In some cases, the solution is highly supersaturated, and this will extend their lifetime. If the solution is saturated such that it is in equilibrium with the nanobubble, the predicted bubble lifetime is infinite. However, a very small deviation from the equilibrium condition dramatically influences the stability. Such that a deviation of only 0.0001% below the saturation level would see the nanobubble dissolve in two seconds (see Figure 1-8). Similarly a fluctuation in size of a nanobubble that is in the equilibrium condition would see the nanobubble rapidly shrink or grow and leave solution due to buoyancy. Thus, the stability of nanobubbles is never likely to be maintained for any significant time.

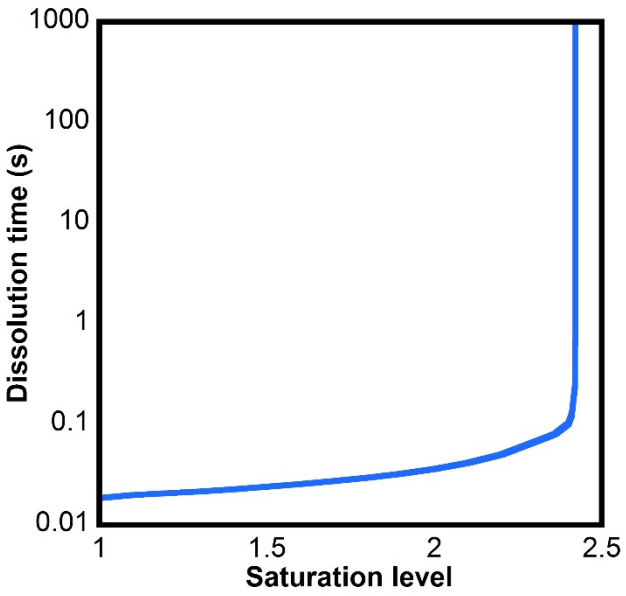

Figure 1-8. Calculated nanobubble lifetime using the Epstein and Plesset theory[1] for a nitrogen filled nanobubble of initial radius 1000 nm as a function of saturation level of N_2 gas in solution. For this calculation, equation 1.11 was implemented iteratively to take account of the increasing Laplace pressure with decreasing size. The lifetime for nanobubbles is expected to be infinite when the level of superaturation is in equilibrium with the nanobubble. However, a small fluctuation in the saturation level below that

required for equilbrium leads to rapid dissolution of the bubble. The parameters used in this calculation are T = 300 K, γ = 0.072 J m^{-2}, D = 2.0 × 10^{-9} m^2 s^{-1}, C_{sat} = 0.6379 moles m^{-3}, and $\rho_{1\ atm}$ = 40.6921 moles m^{-3}.

The effect of extremely high concentrations of nanobubbles has also been considered. Under these circumstances, the diffusion of gas out of a nanobubble is slowed by the effective increase in dissolved gas concentration due to the surrounding bubbles[116]. This is likely only to be significant at extremely high volume fractions. In the work of Johnson and Cooke[108], the formation of a skin of contaminant molecules was clearly implicated in the stability of the bubbles they observed. However, in other nanobubble preparations, the level of contamination would be much lower, so this is unlikely to be a universal stabilizing mechanism. Bunkin[78] proposed that ions at the air-water interface repel each other, effectively reducing the surface tension. However, this implies that the air-water interface cannot charge regulate and that the concentration of ions at the interface would not be determined by the chemical potential set by the concentration in the bulk. Thus this proposed mechanism violates basic thermodynamics. Despite the obvious problems with this mechanism a recent work by Nirmalkar *et al.* [106] invoked the same mechanism.

Yasui *et al.* [117] adapted the equilibrium model proposed by Brenner and Lohse[69] to explain the stability of surface nanobubbles. In this case, solid particles adsorbed to the nanobubble surface are thought to provide a reservoir of gas, as the substrate does in the dynamic equilibrium model. This model has already been abandoned for surface nanobubbles, in part because it requires a constant input of energy, lest it violate the second law of thermodynamics. The adaptation here requires that a reasonable fraction of the nanobubble surfaces are covered in hydrophobic particles, which is not supported by the experimental evidence. Nor does this modification overcome the fundamental violation of thermodynamics in the dynamic equilibrium model.

1.4.1.6 Use and Potential Applications of Bulk Nanobubbles

Despite the lack of direct evidence for the existence of bulk nanobubbles, the level of industry activity and interest in the field is rapidly increasing. This is reflected in the growing membership of the Fine Bubble Industries Association (FBIA) and the rising number of patents in the area. Below is a brief summary of the currently reported and potential applications of bulk nanobubbles. Many of these applications depend on the nanobubbles being present in solution for extended periods of time.

The motion of nanobubbles in solution is influenced by the terminal rise velocity and Brownian velocity. The terminal rise velocity of a spherical bubble of a radius *r* due to buoyancy U_T, is dependent on the boundary condition, and for a no-slip boundary condition, is given by:

$$U_T = \frac{2r^2 \Delta\rho g}{9\eta} \tag{1.13}$$

where $\Delta\rho$ is the difference in density between the bubble and the solution, *g* is the acceleration due to gravity, and η is the viscosity of the liquid. If a slip boundary condition is employed, then the terminal velocity is 1.5 U_T, though studies show that a no-slip boundary condition is appropriate in nearly all cases, due to minute amounts of contamination[118,119]. The calculated no-slip terminal rise velocity for a nanobubble of radius 50 nm is 6.12 nm s^{-1} and for a nanobubble of radius 500 nm is 612 nm s^{-1}. This indicated that the nanobubbles will take a long time to rise to the surface and burst.

The second factor influencing the behaviour of nanobubbles is Brownian motion. The velocity of a Brownian particle *v* over a long time-scale *t* is given by:[120]

$$v = \sqrt{\frac{k_B T}{3\pi\eta r t}} \tag{1.14}$$

where k_B is the Boltzmann constant, T is the temperature, η is the viscosity, and r is the particle radius.

For a nanobubble of a radius 50 nm and 500 nm, the Brownian velocities are 3131 nm s^{-1} and 990 nm s^{-1}, respectively. Comparison of these two values to the rise velocity shows that the Brownian motion dominates the behaviour of the nanobubbles and will act to mix them in solution and oppose the effect of buoyancy.

A number of applications make use of this, particularly those that require the oxygenation of water, as smaller bubbles have longer residence times, and therefore have more time to deliver gas into solution and a larger surface area for a given volume. Moreover, smaller bubbles have higher Laplace pressures and consequently increase the solution saturation concentration of the gas surrounding a bubble. This could potentially have a significant effect if large numbers of nanobubbles were produced. The various applications for bulk nanobubbles are discussed in detail below.

1.4.1.6.1 Biological and Medical Applications

Bulk nanobubbles are increasingly finding biological and medical applications. Bubbles are effective ultrasound contrast agents, since their acoustic response is very different from that of tissues and fluids[121]. Nanobubbles used for ultrasound imaging have been used in several studies[3–8,115], due to their ability to easily pass through the vasculature. For instance, Fan *et al.*[122] compared the echogenic properties, both *in vitro* and *in vivo*, of lipid-coated nanobubbles with an average size of 435.2 ± 60.5 nm with a commercial standard (SonoVue® microbubble contrast agent), and found that a higher contrast was achieved using nanobubbles. A similar study performed by Yin *et al.* [8] showed that lipid coated (armoured) nanobubbles with a mean diameter of 436.8 ± 5.7 nm provided a greater contrast enhancement than microbubbles. The ultrasound images from this study are shown in Figure 1-9. Further, they showed that the enhancement obtained using nanobubbles lasted longer. Zhang *et al.*[123] recently designed

‘multicoloured’ nanobubbles for disease diagnostic applications by encapsulating three types of fluorophores into the lipid-coating of nanobubbles for a combination of fluorescence resonance energy transfer (FRET) and ultrasound imaging. Variations in the ratios of three dyes caused the nanobubbles to register multicolour images under single wavelength excitation, allowing the differentiation of the two tumours.. Further, they showed that two tumour regions exhibited comparable fluorescence signals when triple-dye-doped nanobubbles and dual-dye-doped nanobubbles were injected. This was demonstrated in a tumour on the left hand side of a mouse following the injection of dual-dye-doped nanobubbles, which exhibited a stronger signal compared to a tumour on the right hand side following the injection of triple-dye-doped nanobubbles when the fluorescence signal was 670 nm. The weak and strong florescence signals coming from these two tumours were flipped when they performed the FRET fluorescence imaging using the same nanobubbles but with a fluorescence signal of 790 nm. They hypothesized that this technique could be further developed to distinguish different tissues in a complex clinical diagnosis. Another great area of interest for nanobubbles is their potential use in therapeutic drug delivery[6,9–11]. They can be fabricated for drug delivery purposes by incorporating lipids with head-groups that specifically bind the drug[124,125], which can be released when the nanobubbles are irradiated with high levels of ultrasound energy. Candidate nanobubbles or related entities have also been implicated in an oxygenated medical saline for treating asthma and other autoimmune diseases with remarkable efficacy[126–133].

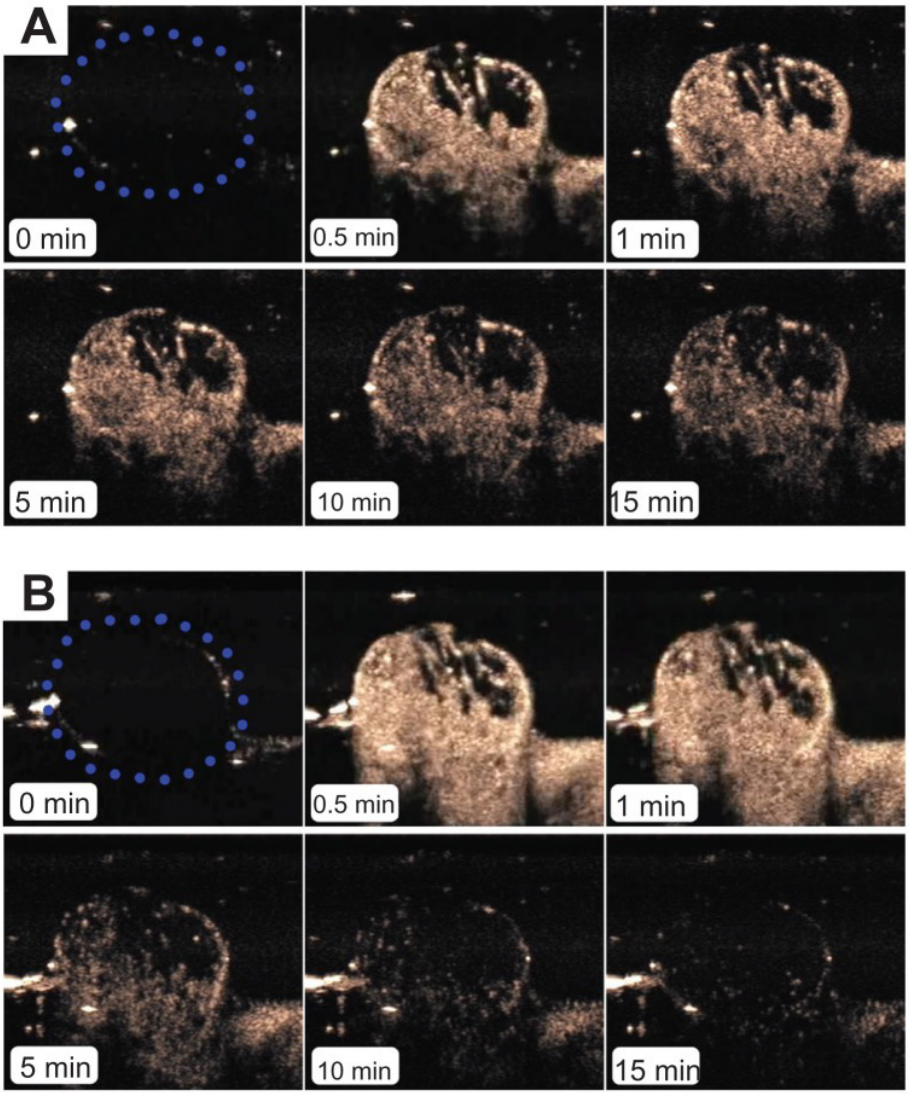

Figure 1-9. Representative set of comparison tumour images before and after injecting nanobubbles (A), and microbubbles (B) into tumour-carrying mice at different times: 0.0, 0.5, 1,5, 10.0 and 15.0 minutes. Images are republished from [T. Yin, P. Wang, R. Zheng, B. Zheng, D. Cheng, X. Zhang, X. Shuai, Nanobubbles for enhanced ultrasound imaging of tumors., Int. J. Nanomedicine. 7 (2012) 895–904. doi:10.2147/ijn.s28830] Copyright (2019) with the permission of Dove Medical Press Ltd.

1.4.1.6.2 Plant Growth and Seed Germination

Candidate nanobubbles are reported to have considerable impact on plant growth and seed germination[30–37]. Ebina *et al*. have claimed that water infused with oxygen nanobubbles, less than 200 nm in diameter, promotes the growth of plants, fish and mice[34]. Images comparing the

growth of plants exposed to oxygen nanobubbles with controls are shown in Figure 1-10. This effect was further investigated through the use of four types of gasses (i.e., air, nitrogen, oxygen and carbon dioxide) on seed germination and plant growth by Khaled *et al.*[30]. All types of nanobubbles except the air nanobubbles were reported to enhance plant growth, but only nitrogen nanobubbles showed a significant effect on the seed germination. It is odd that the air nanobubbles did not have an effect on the growth, whereas nitrogen and oxygen nanobubbles showed an effect. This casts doubt on this research. A recent two-year field experiment conducted by Zhou *et al.*[35] showed that candidate microbubble/nanobubble dispersions had a positive impact on maize roots, although they demonstrated that the effect was also associated with the concentration of dissolved oxygen, where the optimum level was at 20 mg/L. Nanobubbles have also been reported to disrupt water transport, due to hydraulic failure in the xylem of trees[32].

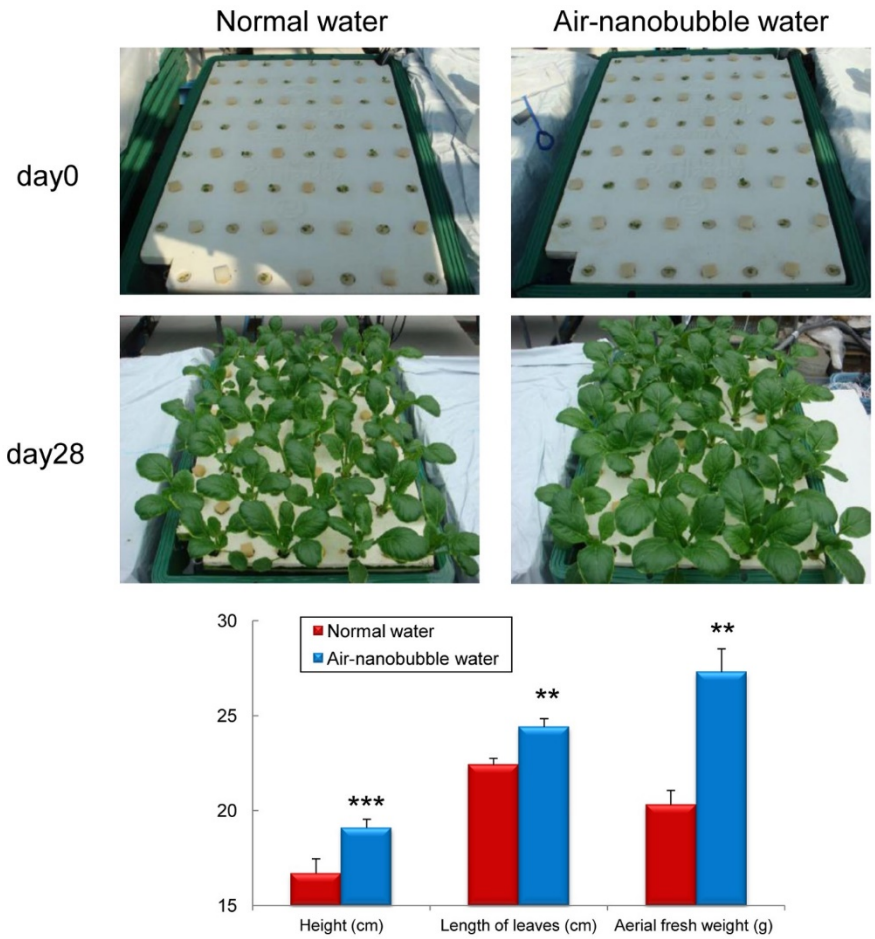

Figure 1-10: Comparison of the growth of plants cultured with normal water and candidate air-nanobubble dispersions. Images are republished from [K. Ebina, K. Shi, M. Hirao, J. Hashimoto, Y. Kawato, S. Kaneshiro, T. Morimoto, K. Koizumi, H. Yoshikawa, Oxygen and air nanobubble water solution promote the growth of plants, fishes, and mice., PLoS One. 8 (2013) e65339. doi:10.1371/journal.pone.0065339] Copyright (2019) with the permission of Plos One.

1.4.1.6.3 Water Treatment

The use of nanobubble dispersions for oxygenation is also being applied in the bioremediation of groundwater pollution[15] and in water treatment[12–17]. Ushida *et al.*[50] observed that nanobubbles collected impurities on their surfaces and hence they could be used to capture and remove these impurities. They argued that the effectiveness of this technique would depend on the concentration of nanobubbles. Xia *et al.*[14] suggested the use of ozone nanobubbles as an

efficient method for remediation of wastewater contaminated with organic matter. They argued that the effectiveness of nanobubble water treatment was pH sensitive, with the highest efficiency for ozone nanobubbles being at pH 5. A recent study by Kyzas *et al.* [17] investigated the effects of nanobubbles on the adsorption of lead ions to activated carbon. They found that the main effect was not on the adsorption capacity, but on the adsorption rate, claiming an acceleration of the adsorption process by 366%.

1.4.1.6.4 Froth Flotation

The use of nanobubbles to separate hydrophobic solid particles in mineral flotation has been extensively investigated[18–29] . It is worth noting here that flotation studies have been conducted using a combination of what has been reported as nanobubbles and larger bubbles; utilising nanobubbles by itself in flotation is inefficient because of their low buoyancy. The suggested mechanism is that nanobubbles adsorb onto the surface of hydrophobic particles, thus promoting their attachment to larger bubbles by acting as a bridge between the particles and the larger bubbles[27]. In a series of publications, Maoming *et al*. suggested that the presence of nanobubbles with larger bubbles can provide the optimum conditions for the flotation of hydrophobic particles[20,21,24–29]. In their studies, they used hydrodynamic cavitation to produce candidate nanobubble dispersions and conventional-sized bubbles, and examined their effect on the flotation of coarse phosphate and coal. They emphasised the potential use of nanobubble technology in froth flotation by demonstrating an increase of 10 % – 30 % and 8 % – 27 % in phosphate and coal recovery, respectively. A similar study by Calgaroto *et al*.[134] also claimed that nanobubbles improved the recovery of quartz particles by 20 % – 30 %.

Another possible application is in depletion flocculation[135] for dewatering of minerals tailings. Depletion flocculation usually employs large quantities of high-molecular-weight non-adsorbing polymers, which imparts an attraction between colloidal particles. If this could be carried out using nanobubbles, it would be both economically and environmentally

advantageous and would eliminate the need to remove the flocculant for downstream processing.

1.4.1.6.5 Cleaning

Bulk nanobubbles are being claimed for cleaning applications, as the dispersion of nanobubbles presents a significant surface area of high interfacial tension, which can attract contaminants due to favourable energetics and thereby prevent their deposition onto surfaces. Candidate nanobubbles have been reported to effectively clean membrane-fouled surfaces[136]. They have also been reported to be used in cleaning textiles[137]. Ushida *et al.* claimed that water containing what was assigned to be nanobubbles exhibited a higher washing rate for textiles soiled with hydrophobic organics by 5 % compared to control water not treated with nanobubbles[137]. The absence of added surfactants means that chemical residues are avoided and the cleaning process is more environmentally friendly.

1.4.1.6.6 Hydrogen Fuels

A high profile claim made by Oh *et al.*[39,40] suggested that hydrogen nanobubbles can be introduced as an energy source for improving engine performance[39,40]. Oh *et al.* argued that gasoline fuels containing what was assigned to be hydrogen nanobubbles were more efficient than conventional gasoline fuel[39]. In another study[40], they claim that the change in the chemical composition of gasoline in a "hydrogen nanobubbles gasoline sample" was measured using chromatography/mass spectrometry, could be the reason for the improvement in efficiency.

1.4.1.7 Summary

Reports that armoured nanobubbles are gas filled are supported by their response to ultrasound. In contrast, reports of uncoated bulk nanobubbles remain controversial, and there is still no definitive proof of their existence. Despite this, a significant number of reports claim to be applying bulk nanbubbles to a wide range of industrial and environmental problems. This has

led to a proliferation of claims many of which are unsupported. Therefore, it is important to systematically examine the existence of bulk nanobubbles. To this end, the development of an easily conducted test or tests that can consistently and reliably differentiate nanobubbles from nanoparticles is required. The widespread adoption of such tests would prevent false reports of bulk nanobubbles and progress our understanding of bulk nanobubbles.

1.5 Aims and Structure of the Thesis

This study aims to

1. Develop a protocol that can be applied to a dispersion of unknown nanoparticles to determine with confidence whether they are gas filled bubbles or otherwise.
2. Investigate methods that have been reported to produce long-lived bulk nanobubbles.

   This knowledge will be used to address fundamental issues in the field, such as understanding what conditions (if any exist) are required for nanobubbles to be long lived.

The following hypotheses will be tested in this study

- The pressure response of nanobubbles can be used to differentiate them from other nanoparticles, even when the nanobubbles are armoured with a shell of insoluble lipid.
- The density of nanoparticles can be determined using the resonant mass measurement method.
- Long-lived bulk nanobubbles can be generated by mechanical means.
- The mixing of ethanol and water produces stable long-lived bulk nanobubbles.
- Supersaturation obtained by a chemical reaction produces long-lived nanosized bubbles in bulk.

1.5.1 Outline

The remainder of this thesis is organised as follows

Chapter 2 describes the main characterization techniques used in this study, including dynamic light scattering, nanoparticle tracking analysis, and resonant mass measurement.

In Chapter 3, the methods developed to distinguish bulk nanobubbles from other nanoparticles are explained in detail. This includes size measurement under the application of external pressure and the determination of nanoparticle density. These methods were applied to armoured nanobubbles that are usually used in ultrasound imaging. The results of these experiments are discussed in detail. These techniques have been applied in chapters 4-6.

Chapter 4 investigates the existence of long-lived bulk nanobubbles produced using two different devices that are designed to produce bulk nanobubble solutions by mechanical means.

In Chapter 5, a simple method for generating nanoparticles by mixing ethanol and water is presented. The constitution of these particles whether they are gas filled or otherwise is determined and how the nanoparticles are formed is explained.

In Chapter 6 the hypothesis that nanobubbles can be generated using a gas evolving chemical reaction to supersaturate the solution is tested. In particular, the chemical reaction between ammonium chloride and sodium nitrite is studied. A promising method for controlling the generation of nanoparticles by controlling the reaction rate of the chemical reaction is proposed and discussed.

Chapter 7 summarizes the main findings of this research and discusses interesting areas for future research in this field.

Chapter 2 Experimental Procedures

A range of methods were employed in this study to provide fundamental information about the nanoparticles such as their average size, concentration, buoyancy, and stability. The techniques described here are shared across most of the research described in later chapters. Techniques that are applied exclusively to a specific portion of the research are reported later in the experimental methods section of the chapter describing that research.

The size distributions of nanoparticles in this study were measured using light scattering methods such as dynamic light scattering (DLS) and nanoparticle tracking analysis (NTA). Resonant mass measurement (RMM) was used to measure the size and buoyant mass of nanoparticles in solution. This chapter provide an overview of each technique including a brief discussion of their capabilities and limitations.

2.1 Dynamic light scattering

In this study, a Zetasizer Nano ZS (Malvern) employing a 633 nm He−Ne laser at a scattering angle of 173° was used to measure the size of particles in solution using dynamic light scattering (DLS).

Dynamic light scattering (DLS), which is also known as photon correlation spectroscopy (PCS), is used to measure the hydrodynamic size of dispersed particles. If a laser light is shone onto a group of stationary particles, they will interact with the electromagnetic radiation and scatter light in different directions. If a detector is placed at a specific angle from the sample, the scattering of the particles in the detector will look like a speckle pattern of dark and bright spots

due to the constructive and destructive interference of the scattered waves from the particles[138]. In reality, suspended particles in solutions are never stationary, rather they move randomly due to Brownian motion. This leads to fluctuating patterns over time. In DLS, the fluctuation in the net intensity of the scattered light is quantified using an autocorrelation function. Small particles that move quickly due to Brownian motion result in a fast decay in the autocorrelation function. In contrast, large particles cause a slow decay in the autocorrelation function. An example of raw correlation data is given in Figure 2-1A below.

For suspended monodisperse particles in solution undergoing Brownian motion, the exponential decay for the correlation function $G(\tau)$ with delay time τ is expressed as[138]

$$G(\tau) = Ae^{-Dq^2\tau} + B \tag{2.1}$$

Where A is the amplitude of the correlation function, which is the intercept the correlation decay, D is translational diffusion coefficient of dispersed particles, B is the baseline, and q is the magnitude of the scattering vector which is related to the angle θ by

$$q = \frac{4\pi n_D}{\lambda} \sin\frac{\theta}{2} \tag{2.2}$$

where n_D is the refractive index of the solvent

DLS uses the Stokes-Einstein law to extract the average size of nanoparticles from the diffusion coefficient D. This size is reported as the z-average diameter, which is simply the intensity weighted mean size and is the most reliable size measurement produced by the instrument. The form of the Stokes-Einstein law is dependent on the hydrodynamic boundary condition at the surface of the particle. For a spherical particle, the Stokes-Einstein law is:

$$r = \frac{k_B T}{c\pi\eta D} \tag{2.3}$$

where k_B is the Boltzmann constant, T is the temperature, η is the viscosity, r is the particle radius, and c is 4 for a slip boundary condition and 6 for a no-slip boundary condition. If the wrong boundary condition is used, the error in the measured size may be substantial; a particle with a slip boundary condition analysed using a no-slip boundary condition would have its size underestimated by one-third. Generally, a no-slip condition is assumed in equation 2.3. This assumption is accurate for solid particles and liquid droplets. For nanobubbles, it is possible that a slip boundary condition should be used as the gas-liquid interface is often treated with a slip boundary condition. However, analysis of the rise velocity of bubbles in purified water shows that only when water has undergone extreme purification measures is a slip boundary condition evident for a bubble that is more than a few seconds old [118,119]. Therefore, it is appropriate to use the no-slip boundary condition here, even for nanobubble samples (i.e., c = 6 in equation 2.3).

DLS provides three types of distributions: intensity, volume, and number distribution. The intensity distribution reflects the raw distribution obtained by the DLS technique. It is worth noting that the size measurements based on intensity distribution are more sensitive to large particles than to small particles. This is due to the proportional relationship between the intensity of scattered light and the sixth power of the diameter of the detected particle according to the Rayleigh approximation[139].

$$I \approx d^6 \qquad (2.4)$$

These limitations must be borne in mind when using the results from the Zetasizer. The other two distributions are useful but less accurate as they are derived from the intensity measurements using Mie theory[140,141]. The volume distribution shows the total volume of particles in different size bins, whereas the number distribution shows the number of particles in different size bins. The last two distributions are calculated from intensity measurements based on the assumption of the optical properties of the material, namely, refractive index and

absorption. Thus, the volume and number distribution can only be used if the optical properties of the material and solvent are known.

DLS is suitable for measuring monodispersed samples. It measures particles ranging from 0.3 nm to 10 µm. It does not require a large sample volume or long periods of time for sample preparation. However, an appropriate sample concentration is needed to meet the quality criteria for measurement, where the minimum and maximum concentrations are 0.1 mg/ml. and 40 % weight/volume, respectively.

A typical DLS size measurement for a standard nanoparticle is shown in Figure 2-1 . The measurements were made with automatic attenuation at a position of 4.65 mm from the cuvette wall and analysed using the Malvern Zetasizer software version 7.1.

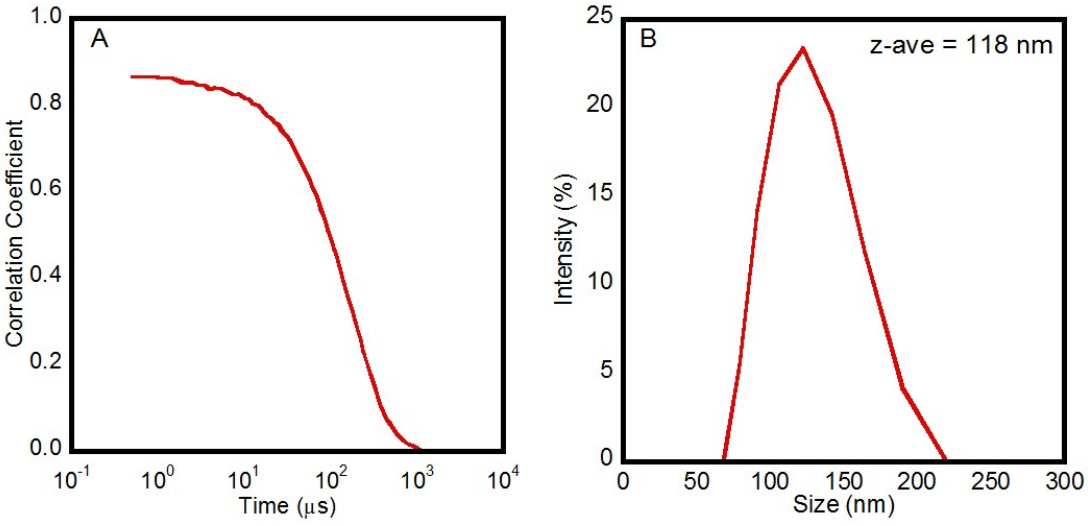

Figure 2-1. An example of raw data obtained using DLS for 100 nm standard silica particles (nanoComposix, USA). Panel A shows the correlation function over time, and Panel B shows the corresponding intensity weighted distribution and the measured z-average for this data is reported in the legend. (The supplier-reported physical characterization data for these standard particles are shown in Table 2-1)

2.2 Nanoparticle tracking analysis

A NanoSight (NS300, Malvern) was used to measure the size and determine the concentration of nanoparticles in solution.

The first description of the Nanoparticle tracking analysis (NTA) technology was published in 2006 by Malloy and Carr[142]. It has a unique capability in visualizing the scattered light from individual nanoparticles in a liquid using a conventional optical microscope. By tracking the particles,; it can be used to obtain the size distribution of the particles. Tixier *et al*., conducted one of the early experiments using NTA to obtain the size distribution of oil droplets in lyotropic cholesteric and thermotropic nematic emulsions[143]. In the same year, Borm *et al.*[144] highlighted the possible uses of NTA by characterising nanoparticles in order to monitor changes in particle size and concentration. The novelty of this technique has attracted growing interest for use in characterising nanoparticles and obtaining particle size distributions for different applications such as drug delivery[145–147], protein aggregations[145,148,149], virology and vaccine production[150,151], toxicology[152,153], and nanoparticle design and production[154–156].

In this technique, suspended particles in a solution are illuminated by a laser light source. The scattered light from these particles is detected and recorded into movie files (see Figure 2-3A) using a camera mounted on a 20 x magnification microscope. A schematic representation of the instrument is shown in Figure 2-2. The instrument employs the nanoparticle tracking analysis (NTA) system to track the scattering of the individual particles and calculate their size based on their diffusion under Brownian motion using the 2 dimensional modified version of Stokes-Einstein equation[157].

$$\frac{\overline{(x,y)^2}}{4t_s} = D = \frac{k_B T}{6\pi\eta r} \tag{2.5}$$

Where $\overline{(x,y)^2}$ is the mean squared displacement of a nanoparticle in two dimensions and t_s is the sampling time.

As NTA measures the size particle by particle, the NanoSight instrument generally provides more accurate size distribution data than DLS[145]. In addition, the instrument calculates the concentration of particles by counting the number of particles observed in an approximately 100 × 80 μm field of view illuminated by a beam with a depth of 10 μm. The concentration range for the instrument is within a range of 10^7 to 10^9 particles/ml for particles in the 20–2000 nm size range.

The NanoSight used here was equipped with a blue laser light source (70 mW, λ = 405 nm) and NanoSight software (version V3.1) was used to process all measurements. To achieve a more accurate measurement, the sample was inserted into the NanoSight cell using a syringe pump at constant speed (flow rate set to 30 in arbitrary units) for the duration of measurement.

The size distribution data obtained for a standard consisting of spherical polystyrene particles with a diameter of 100 ± 0. 2 nm (Thermo Fisher Scientific) is shown in Figure 2-3. The measurement was the average of numerous particles imaged in five recorded videos with a duration of 60 seconds each, captured at 25 frames/s. The parameters used were camera level = 14, threshold = 3, gain = 366, and the viscosity for water at 25 °C, 0.888 Cp. The camera level is responsible for the brightness and contrast of the image, which are used to identify the particles with minimum background noise. The viscosity parameter affects the size measurement, whereas the other parameters primarily influence the measurement of concentration (see section 2.3.2.4).

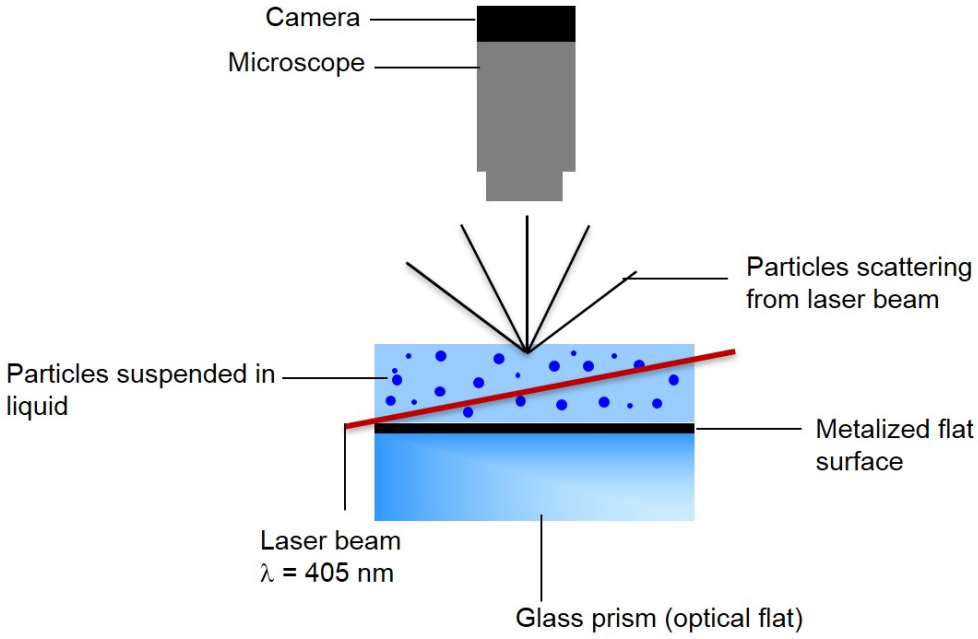

Figure 2-2. Schematic diagram of the NanoSight instrument, adapted from a diagram on the webpage of the instrument manufacturer from Malvern[1].

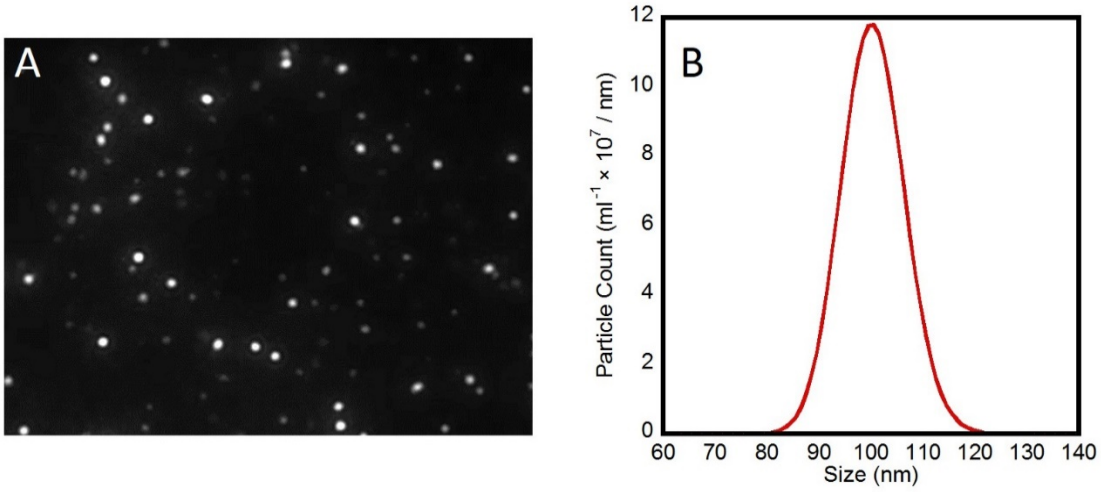

Figure 2-3. Panel A. A single frame showing the visualized polystyrene latex nanoparticles using NnaoSight NS300. NTA tracks the Brownian motion of these individual particles to determine the corresponding size distribution (Panel B).

[1]https://www.malvernpanalytical.com/en/learn/knowledge-center/whitepapers/WP140311NanoScaleMaterialCharacterizationNTAReview

Comparison between DLS and NTA

Filipe *et al*[145] performed a comparison study between DLS and NTA. They showed that NTA is superior for reporting accurate size distributions for both monodispersed and polydispersed samples compared to DLS. In addition, the accuracy of the NTA measurement was not affected by the presence of large particles in the suspension, unlike in the DLS measurement, where the accuracy of the size measurement was greatly affected. However, DLS has some advantages over NTA. For instance, the size range in DLS (0.3 nm – 10 μm) is broader than the size range in NTA (20 nm – 2 μm). Further, while NTA measurements are limited to a concentration range of $10^7 – 10^9$ particles/ml, DLS can measure concentrated samples without dilution (up to 40 % weight/volume). Finally, DLS measurements are known to be less time consuming than NTA measurements, which require a skilled operator to obtain accurate and reproducible results.

2.3 Resonant mass measurement

An Archimedes (Malvern Instruments, Malvern, UK) was used to determine the size and buoyant mass of nanoparticles in solution. The instrument uses the resonant mass measurement technique to measure the mass of a particle relative to the solvent for individual suspended particles [105].

Burg *et al.*[105] first demonstrated the RMM technique in 2007 by weighing suspended single nanoparticles and bacterial cells in water. In other work by the same authors[158], RMM was used to measure the mass, density and size of polystyrene particles, E. coli bacteria and human red blood cells. The technique has since been commercialised by Affinity Biosensors (Santa Barbara, CA) and used for a range of purposes such as determining the density of single cells[159], monitoring cell growth[160] and quantifying the coating on particle surfaces[161]. RMM has also

been used to characterise protein particles in order to quantify the protein and silicon oil contaminates that are present in commercial silicon oil-lubricated prefilled syringes[162,163].

In RMM, a fine cantilever with an internal channel is used as the sensing unit (panel A in Figure 2-4). The nanoparticle suspension is passed through the microchannel using a pressure gradient, whilst the resonance frequency is monitored. The nanoparticle solution is delivered to the microfluidic channel via two wider bypass channels that are connected to the inlet and outlet of the embedded microfluidic channel. The flow within the microchannel is controlled by tuning the pressure at the inlet and the outlet of the bypass channel. This has been previously described in detail by Burg *et al.* [105]. As particles pass through the sensor, the resonant frequency of the sensor shifts. If the particle density is greater than that of the surrounding solvent, the frequency decreases, and if the particles are less dense than the solvent, the frequency increases (see panel B in Figure 2-4). Thus, positively buoyant particles can easily be distinguished from negatively buoyant particles by the sign of the change in frequency. Each particle leads to a spike in the resonance frequency as the particle moves through the channel. Therefore, surface nanobubbles or nanoparticles adhered to the surface of the microchannel are not measured, as they will induce a change in the baseline signal, rather than a spike in the resonance frequency.

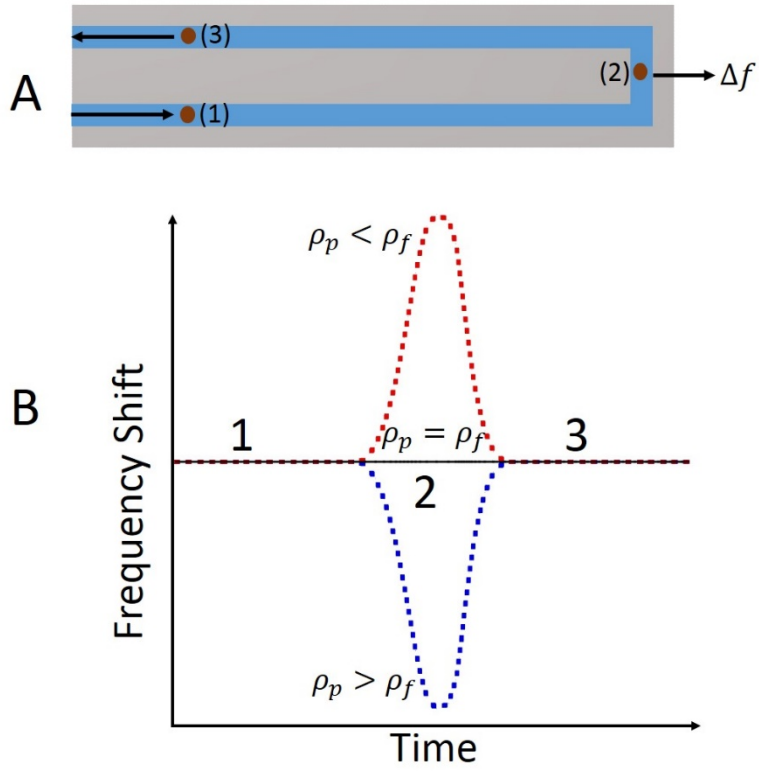

Figure 2-4. Principle of the RMM technique. The Archimedes uses a fine cantilever with an embedded fluidic channel to detect the particles in solution (panel A). Positions 1–3 correspond to the order of movement of the particles as they enter the channel (1), reach the sensing point (2) and finally leave the channel (3). The flow of the dispersed nanoparticles ($\rho_p \neq \rho_f$) through the microchannel causes a shift in the resonance frequency of the cantilever, which enables the instrument to distinguish positively buoyant particles ($\rho_p < \rho_f$) from negatively buoyant particles ($\rho_p > \rho_f$) (Panel B).

This technique determines the size based on the frequency shift (Δf), which is proportional to the buoyant mass (m_B) and the sensitivity of the resonator (S_r) (eq 2.6) The software converts the buoyant mass to a dry mass (m) (eq 2.7), and to a corresponding particle diameter (eq 2.8) based on the density of fluid (ρ_f) if the density of the suspended particles (ρ_p) is known.

$$m_B = \frac{\Delta f}{S_r} \tag{2.6}$$

$$m = \frac{m_B}{(1 - \frac{\rho_f}{\rho_p})} \tag{2.7}$$

$$d = \sqrt[3]{\frac{6m}{\pi\rho_p}} \tag{2.8}$$

Although particles less dense than the solvent can be immediately distinguished from particles denser than the solvent, due to the sign of the change in frequency, the technique does not directly yield the density of the particles, as both the particle size and density contribute to the buoyant mass of the particle. However, a method was adapted in this study to calculate the mean density of dispersed nanoparticles using the RMM method. (details are reported in §3.4.4).

RMM is designed to measure the buoyant mass and size of particles in the micron and nano size ranges using microsensor and nanosensor chips with internal channels having square cross sections of 8 × 8 μm^2 and 2 × 2 μm^2, respectively. Optical microscope images of the sensors are given in Figure 2-5. The particles upper size limit is set by the channel size and is therefore 8 μm for the microsensor chips and 2 μm for the nanosensor chips. The nanosensor chips have a higher sensitivity (lower detection limit of 350 ag) than the microsensor chips (lower detection limit of 1.5 fg).

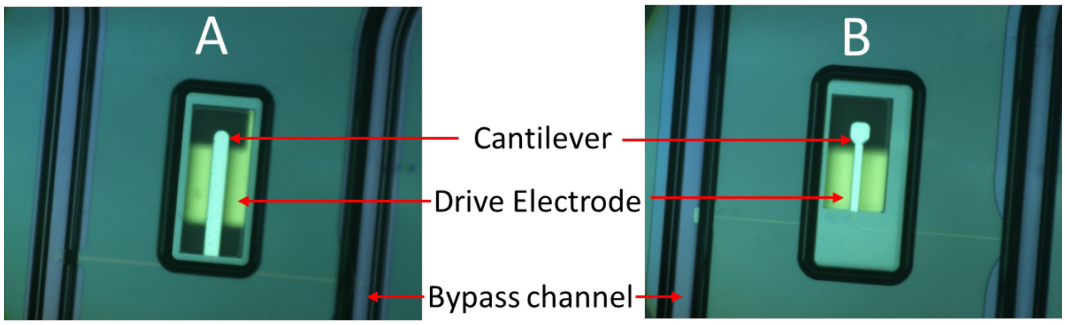

Figure 2-5. Optical microscope images of a microsensor (A) and nanosensor (B) (magnification, 5x) used in the RMM system. The sensors have cantilevers with embeded internal channels, as shown in Figure 2-4A. The cantilevers are connected to a bypass channel from the right and left sides. The dimensions of the bypass channels (~ 50 µm) are designed to be larger than the cross dimensions of the embedded microfluidic channel in the sensor to allow the sample to be delivered quickly.

A disadvantage of RMM is that the sensor can become blocked. Thus, great care should be taken when preparing samples for RMM. To avoid blocking the sensor, it is recommended that the samples be filtered through a smaller pore size than the width of the channel. If blockage occurs, it is not straightforward to resolve the issue, given the very small dimensions of the channel. Difficulty was experienced in restoring blocked sensors during this study. To resolve this, the blocked sensors were rinsed with different surface-active agents, such as a positively charged surfactant (CTAB), a negatively charged surfactant (SDS), and even a commercial stain remover (OxiClean™, Church & Dwight, USA, < 10% w/w). The stain remover was found to be more effective than the other agents. However, the success rate of restoring the blocked sensors was low, even with the stain remover. Thus, precautions should be taken to eliminate larger particles when preparing and measuring samples using RMM.

ParticleLab software (version 1.2) provided by Malvern, was used to process all measurements described in this study. Standard spherical particles of polystyrene with a diameter of 508 ± 8 nm purchased from Thermo Fisher Scientific were used to calibrate the RMM sensors prior to

measurements. The raw frequency and the buoyant mass, dry mass, and size histogram for this sample are shown in Figure 2-6.

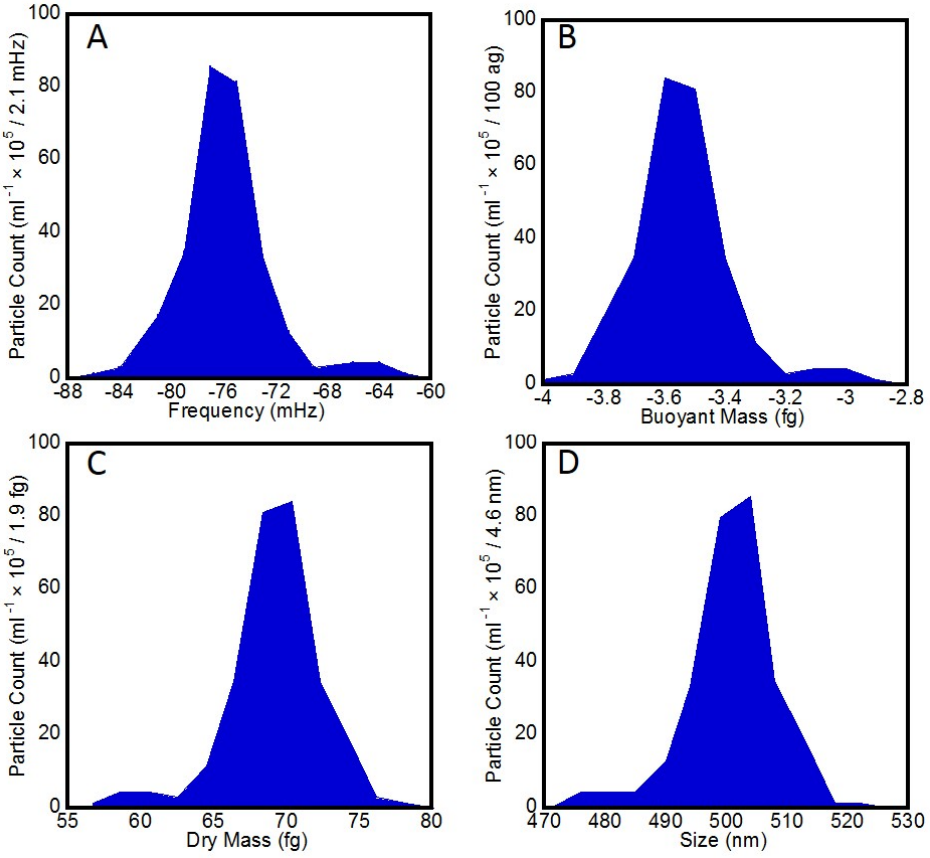

Figure 2-6. RMM on a 508 ± 8 nm polystyrene standard in water. The measured raw frequency histogram (A) was used to calculate the buoyant mass histogram (equation 2.6) (B), convert it to a dry mass histogram (equation 2.7) (C), and finally, to a size distribution (equation 2.8) (D). These data were determined based on a total of 300 particles detected at room temperature using a nanosensor chip. The detection threshold parameter was set at 0.009 Hz and the density for polystyrene nanoparticles[2] was set to 1.055 g/cm^3.

[2] https://www.thermofisher.com/au/en/home/life-science/cell-analysis/qdots-microspheres-nanospheres/idc-surfactant-free-latex-beads/latex-bead-technical-overview.html

2.3.1 Comparison between NTA and RMM

NTA and RMM are both unique methods for characterising nanoparticles in solution. As RMM can distinguish positively buoyant particles from negatively buoyant particles, it has a clear advantage over NTA in the characterisation of particle dispersions that may contain nanobubbles. However, RMM requires great care when performing measurements to eliminate larger particles and to avoid blockage of the sensor. Both techniques are time-consuming and require a skilled operator.

The two techniques use two different working principles to measure the size and concentration. The study below describes a preliminary evaluation of RMM compared to NTA using different size ranges of standard particles. This study was important for testing and comparing the techniques before applying them to nanobubble candidate samples, as we are unaware of any available study comparing these two techniques.

2.3.2 Evaluation of Size and concentration measurements: a comparison of NTA and RMM

2.3.2.1 Preparation of standard nanoparticles

Standard silica nanoparticles and gold nanoparticles with diameters ranging from 80 – 200 nm and 60 –100 nm, respectively, purchased from (nanoComposix, USA) were used for the comparison study. The supplier reported the average diameter (measured using transmission electron microscopy (TEM)), the hydrodynamic diameter (measured using Zetasizer Nano ZS) and the nanoparticle concentration. The physical characterization data, and the supplier lot number for each standard is shown Table 2-1. The nanoparticles were diluted from the supplied package in high-grade purified water (ELGA PURELAB Chorus 3 system with a resistivity of

18.2 MΩ) until the concentration was suitable for NTA and RMM measurements. The final diluted particle concentration used in NTA and RMM is provided in Table 2-1. The sample was sealed and shaken vigorously by hand for 60 seconds at the time of dilution, and also before characterization.

For the polydisperse samples, the standard nanoparticle solutions that had been diluted in Table 2-1 were used to prepare a mixture containing 80 nm, 100 nm and 200 nm silica nanoparticles and another mixture containing 60 nm, 80 nm and 200 nm gold nanoparticles at an equal volume ratio of 1:1:1. Note the concentration of each particle size in the mixtures is not the same.

2.3.2.2 Instruments parameters

For NTA measurements, the parameters used were camera level = 14, threshold = 3 and gain = 366; the viscosity for water at 25°C = 0.888 cP. RMM measurements were performed at room temperature using nanosensor chips. Data were acquired until 300 particles had been measured. The detection threshold was set to 0.009 Hz. The density of the gold nanoparticles was set to 19.32 g/cm^3. The density of silica nanoparticles varies and was not known for these samples. Therefore, the density was estimated by adjusting the density in the Archimedes software until the sum of mean sizes for 100 nm and 200 nm silica nanoparticles matched the sum of the mean size reported by the manufacturer for the samples. This yielded a mean density value of 2.2 g/cm^3, which was used in RMM to analyse the silica nanoparticle measurements.

Table 2-1. Details of the particles used in this study as reported by the supplier (nanoComposix, USA) and the dilluted particle concentration.

	80 nm SiO_2	100 nm SiO_2	200 nm SiO_2	60 nm Au	80 nm Au	100 nm Au
Supplier Lot Number	ECP1152	JEA0068	JEA0113	MEL0003	BAM0007	JSD0020
Diameter (TEM)	82.6 ± 4.7 nm	99.2 ± 5.8 nm	199 ± 15.2 nm	63 ± 6 nm	76 ± 7 nm	103 ± 10 nm
Hydrodynamic Diameter*	98.6 nm	118.8 nm	218.6 nm	71 nm	84 nm	105 nm
Initial Particle Concentration* (particles/ml)	1.5×10^{13}	9.5×10^{12}	1.1×10^{12}	2.1×10^{10}	1.2×10^{10}	4.7×10^{9}
Diluted Particle Concentration (particles/ml)	9.5×10^{8}	1.4×10^{9}	2.5×10^{8}	2.5×10^{8}	2.2×10^{8}	1.5×10^{8}

* The hydrodynamic diameter and concentration was reported by Nanocomposix without error bars.

2.3.2.3 Size measurements for monodispersed samples

Standard silica nanoparticles (80 nm, 100 nm, 200 nm) and gold nanoparticles (60 nm, 80 nm, 100 nm) were measured using NTA and RMM. The size distribution is shown in Figure 2-7, and the values are reported in Table 2-2. The size measurements for gold nanoparticles showed reasonable agreement between the two techniques and the supplier-reported size measurements (Table 2-2). The mean size measurements were 69.5 ± 0.4 nm, 79.8 ± 0.6 nm, and 96.8 ± 0.5 nm using NTA, and 61 ± 0.2 nm, 73 ± 0.3 nm, and 97 ± 0.4 nm using RMM, for 60 nm, 80 nm, and 100 nm gold nanoparticles, respectively. These values agree with the values reported by the supplier, in which the reported diameters were 63 ± 6 nm, 76 ± 7 nm, and 103 ± 10 nm for 60 nm, 80 nm, and 100 nm gold nanoparticles, respectively. Further, the size distributions for 80 nm and 100 nm gold particles obtained using NTA, agreed with the size distributions

obtained by RMM (Figure 2-7 Panels E-F). For 60 nm gold particles, the size distributions using the two techniques overlapped, but the distributions were offset. RMM registered smaller particles down to 40 nm, whereas NTA detected larger particles up to 80 nm in size (Figure 2-7D).

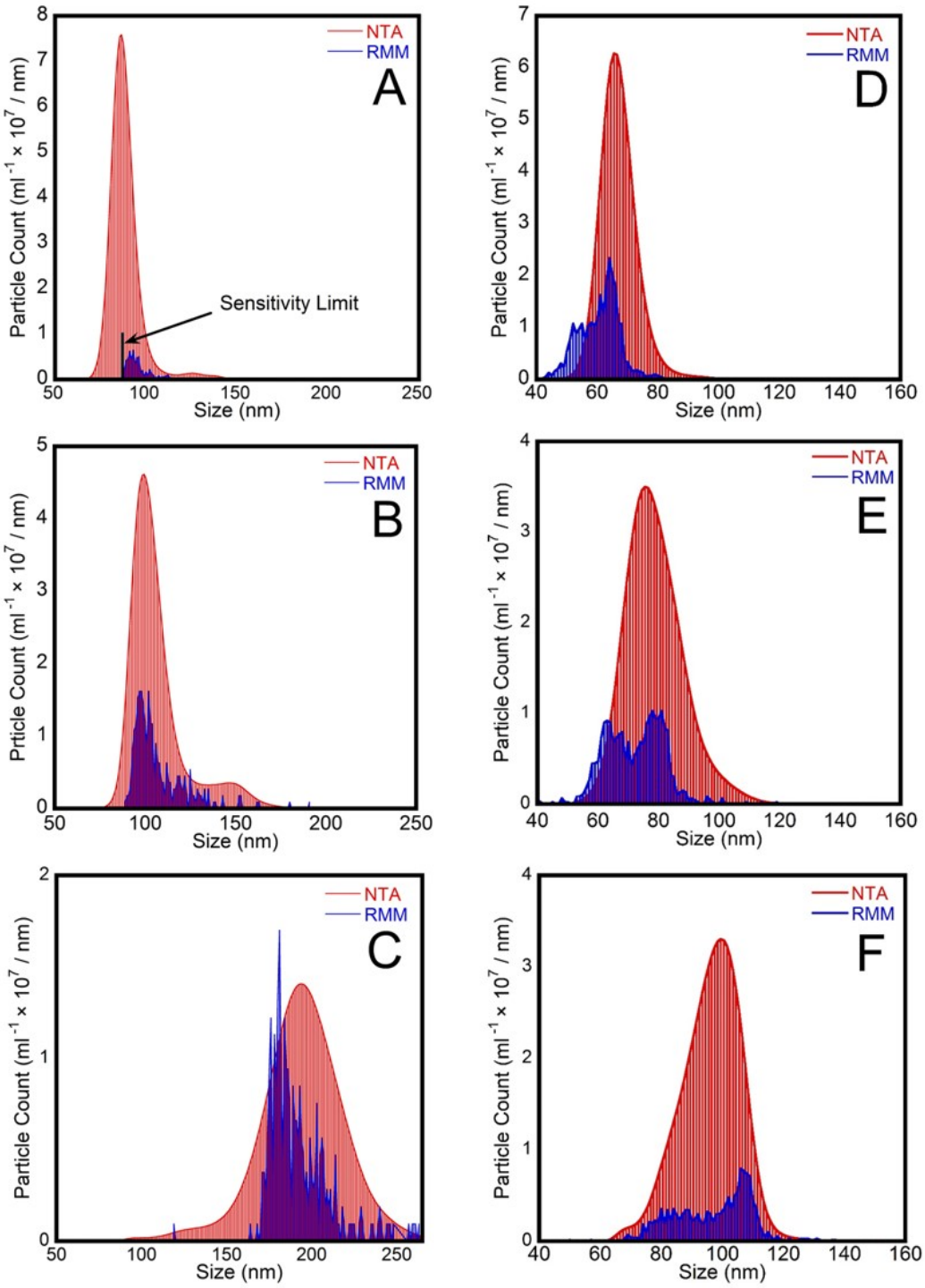

Figure 2-7. Size distribution for standard nanoparticles using NTA and RMM. The left column shows the size distribution for silica nanoparticles with a reported mean diameter of 82.6 ± 4.7 nm (A), 99.2 ± 5.8 nm (B), and 199 ± 15.2 nm (C), and the right column shows the size distribution for gold nanoparticles with an average diameter of 63 ± 4.7 nm (D), 76 ± 7 nm (E), and 103 ± 10 nm (F). Note the concentration scale on these figures is not the same.

NTA provided accurate size measurements for 100 nm and 200 nm silica, with obtained mean sizes of 105.2 ± 1 nm, and 187 ± 1.9 nm, which were in agreement with the reported values of 99.2 ± 5.8 nm, and 199 ± 15.2 nm for, 100 nm, and 200 nm silica respectively. However, the measured mean size of 80 nm silica was above the reported value, where the measured size and the reported value were 89.3 ± 0.6 nm and 82.6 ± 4.7 nm respectively. The sizes measured using RMM differed slightly from that measured using NTA for 100 nm silica and 200 nm silica, with mean sizes of 108 ± 0.8 nm and 192 ± 1 nm, respectively. The slight variation in RMM could be due to variation in the density of silica, which does not have a well-defined density (a typical density range for silica is 1.9–2.7 g/cm^3)[164].

For 80 nm silica nanoparticles, RMM was unable to register all the particles, resulting in an inaccurate size measurement (see Figure 2-7A). This was attributed to the particles having a buoyancy below the detection limit of RMM, as the instrument was unable to register silica nanoparticles with sizes of less than 87 nm, as shown by the cutoff in the figure. More details of the effects of nanoparticle and solvent density on the minimum detection limit of RMM are given in §3.4.4 .

Table 2-2. Tabulated size and concentration measurements for standard silica and gold nanoparticles using NTA and RMM. The error bars in the size measurements represent the standard error.

		80 nm SIO_2	100 nm SIO_2	200 nm SIO_2	60 nm Au	80 nm Au	100 nm Au
Reported Size (nm)		82.6 ± 4.7 nm	99.2 ± 5.8 nm	199 ± 15.2 nm	63 ± 6 nm	76 ± 7 nm	103 ± 10 nm
NTA	Mean Size (nm)	89.3 ± 0.6	105.2 ± 1	187± 1.9	69.5± 0.4	79.8± 0.6	96.8± 0.5
	Concentration (particles/ml)	1.2×10^9	1.3×10^9	8.6×10^8	8.7×10^8	7.8×10^8	7.8×10^8
	Measured conc./expected conc.	1.20	0.92	3.4	3.50	3.50	5.20
RMM	Mean Size (nm)	97 ± 7	108 ± 0.8	192 ± 1	61 ± 0.2	73 ± 0.3	97 ± 0.4
	Concentration (particles/ml)	6×10^7	2.7×10^8	2.8×10^8	2.7×10^8	2.2×10^8	1.4×10^8
	Measured conc./expected conc.	0.06*	0.20*	1.12	1.10	1.00	0.93

*Particles with bin size less than the cut-off (i.e. 87 nm) were undetected leading to only a fraction of the population being detected.

2.3.2.4 Concentration measurements

Another conclusion that can be drawn from this comparison regards the variation in the measured concentration. The original and measured concentrations are shown in Table 2-2. For NTA, the measured concentrations for 100 nm and 200 nm silica were close to the original values, whereas the concentrations for the other nanoparticles were overestimated by factors of 3 to 5 (see Table 2-2). In contrast, the concentration measured using RMM was in agreement with the value reported by the supplier, when the entire population was within the detection limit. This is shown in the concentration measured for all size ranges of gold nanoparticles and 200 nm silica nanoparticles (values are reported in Table 2-2). For 100 nm silica particles and 80 nm silica particles, the concentrations were underestimated by factors of 5 and 15, respectively. However, the concentration comparison here is not valid because a portion of the particles were below the detection limit.

In NTA, the concentration measurement is greatly affected by the camera level, where an increase in the camera level leads to saturate the scattering intensity of the particles and an increased number of detected particles[165,166]. A high camera level is needed to detect smaller particles, whereas larger particles are usually detected at low camera levels. Measuring small particles (< 100 nm) at low camera levels thus causes small particles to go undetected, whilst measuring large particles (~ 1000 nm) at high camera levels leads to oversaturation of the scattering intensity, which causes background noise and false results[31]. This poses challenges when measuring a very polydisperse sample that contains a mixture of very small particles (< 50 nm) and very large particles (~ 1000 nm), with an optimal setting for the camera level being hard to achieve in such cases. Another key factor in determining the concentration in NTA is the detection limit (i.e. detection threshold), which is the minimum intensity required for a particle to be registered[31]. In contrast to the camera level, a low detection limit is needed to detect small particles and increasing the detection limit results in underestimation of the actual

number of particles. However, if the detection limit is too low noise interferes with the particle tracking. Further, the capture time needs to be sufficient to track the fast movement of very small particles and needs to be longer for larger particles in order to produce reliable statistics and results. Finally, the concentration of nanoparticles measured by NTA has been reported to be affected by the flow mode in which particles are measured whilst fluid passes through the cell[167]. Mass *et al.*[167] indicated that using the flow mode leads to the concentration of nanoparticles being underestimated, compared with the static mode. This underestimation in the flow mode is mainly because of the drift velocity, which causes more particles to move out of the field of view before being counted. However, the flow mode is preferred in NTA measurements because it allows a larger volume of the sample to be detected and counted in the same measurement. This allows a greater number of particles to be measured offering a closer reflection of the actual sample size distribution than the static mode. It is worth noting here that the concentration measurement using NTA was overestimated for most of the particles. It is still not known the reason behind overestimating the concentration of the nanoparticles.

As discussed above, concentration measurements using NTA are strongly affected by the parameters selected, and any variation in the parameters would change the reported concentrations. Therefore, it is recommended that a set of suitable parameters for a particular measurement be chosen and that these parameters are not changed between samples that are being compared. The parameters also depend on the sample and are not necessarily a single set that is suitable for all samples; therefore, the concentration measurement using this technique should not be seen as an accurate, absolute measure unless it has been calibrated against an appropriate (i.e. similar) standard under the same imaging conditions.

Concentration measurements using RMM could also be influenced by the choice of parameters. For instance, a crucial parameter used in RMM is the limit of detection (LOD), which is the

minimum shift in the sensor frequency to register the presence of a particle. Choosing a higher value for the LOD than the optimal value increases the baseline during measurement, which then leads to discounting signals that may correspond to small particles. The aim is to set the LOD as low as possible in order to detect as many particles as possible without registering noise as particles. This selection can be informed by observing the noise in the solvent in the absence of particles. Further, as the particles are delivered to the microfluidic channel via a bypass channel, not all particles are necessarily delivered successfully, with some particles not entering the microfluidic channel, leading to less particles being registered in the sensor than the actual number of particles in the sample. Finally, concentration measurements using RMM are influenced by the concentration range of the nanoparticles. The concentration range for an accurate RMM measurement is $10^7 – 10^9$ particles/ml, such that the instrument detects one particle in the microfluidic channel at any given time. If two or more particles enter the detector at the same time, the software rejects this data, thus affecting the reported concentration[168]. This leads to an upper limit for the concentration that can be studied. The lower limit is due to the time taken to count a sufficient number of particles.

2.3.2.5 Size measurements for polydisperse samples

To test the accuracy of NTA and RMM measurements for polydisperse samples, a mixture of silica and gold nanoparticles were prepared by mixing the monodispersed 80 – 100 – 200 nm silica and 60 – 80 – 200 nm gold nanoparticles reported above separately. The results of the NTA and RMM measurements for these samples are shown in Figure 2-8. Apart from the 80 nm silica in which most of the monodispersed population could not be detected by RMM (see Figure 2-7A), RMM showed well-defined peaks for all size ranges in both the silica and gold samples. NTA was also able to show the individual peaks for 100 nm and 200 nm silica; however, it was not able to show well-defined peaks within smaller size ranges. The 80 nm

silica was not distinguishable using NTA in the mixture, as the sample merged with the 100 nm peak (Figure 2-8A). Similarly, the peaks for 60 nm, 80 nm and 100 nm gold were not well defined when compared to RMM (Figure 2-8B).

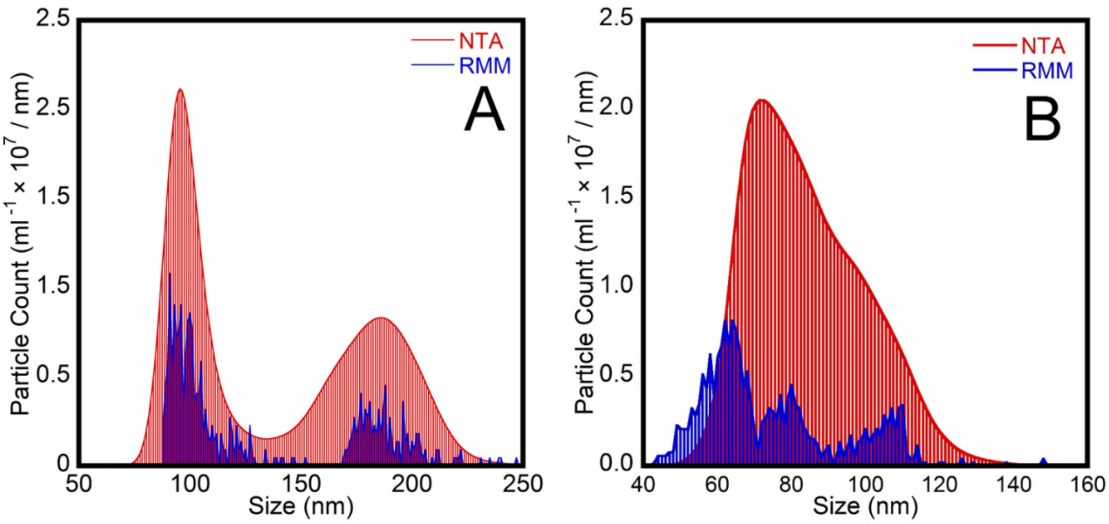

Figure 2-8. Size distribution obtained using NTA and RMM for a mixture of different size ranges of monodispersed nanoparticles (A) silica (80 – 100 – 200 nm), and (B) gold (60 – 80 – 100 nm) (B). The size distribution and concentration for each size range before mixing is shown in Figure 2-7 and Table 2-2.

2.3.3 Summary

The main experimental characterization methods used in this thesis have been described in this chapter. These techniques include light scattering techniques including dynamic light scattering (DLS) and nanoparticle tracking analysis (NTA) and resonant mass measurement (RMM). A detailed overview of the principles and capabilities of each technique has been provided.

In the second part of this chapter, a preliminary comparison between NTA and RMM techniques was conducted on monodispersed and polydispersed nanoparticles. NTA provided accurate size measurements and distributions for monodispersed silica and gold nanoparticles. RMM also yielded accurate size measurements with the exception of the 80 nm silica

nanoparticles, as a portion of these particles was below the detection limit for RMM. For polydisperse samples, well-defined peaks were shown in the size distributions obtained by RMM, whereas NTA was not able to resolve the peaks of the two smaller particle sizes. Finally, the accuracy of the concentration measurements using NTA varied from one range of particles to the next, whereas RMM provided more accurate concentrations as long as the entire population of particles was within the limits of detection. Clearly the lessons here are that caution is required when comparing concentrations and size measurements between the techniques and therefore wherever possible these comparisons on real samples should be made using the same technique. More research is needed to expand this comparison for different particle types and different particle size distributions. Further, is it important to do the comparison by manipulating the experimental parameters used in both NTA and RMM techniques to better understand how such parameters influence the measurement.

Chapter 3 Differentiating Between Nanoparticles and Nanobubbles by Evaluation of the Compressibility and Density of Nanoparticles

Most of the material in this chapter is reproduced with minor changes from the following references:

M. Alheshibri, V.S.J. Craig, Armoured nanobubbles; ultrasound contrast agents under pressure, J. Colloid Interface Sci. 537 (2019) 123–131. doi:10.1016/j.jcis.2018.10.108.

M. Alheshibri, V.S.J. Craig, Differentiating Between Nanoparticles and Nanobubbles by Evaluation of the Compressibility and Density of Nanoparticles, J. Phys. Chem. C. 122 (2018) 21998–22007. doi:10.1021/acs.jpcc.8b07174.

3.1 Introduction

A lack of techniques and methods designed to distinguish bulk nanobubbles from other nanoparticles has meant that most reports of measurements on long-lived bulk nanobubbles have not been definitively shown to involve nanobubbles. Therefore, the field of bulk nanobubble research is in dire need of reliable methods to demonstrate that a particular dispersion of nanoparticles contains nanobubbles, particularly as their long term stability challenges our fundamental understanding of the interplay between solubility, Laplace pressure, Henry's equation and diffusion.

This chapter reports a novel protocol that can be applied to candidate nanobubble dispersions. The samples selected for this study are well known gas filled bubbles that have been used in ultrasound imaging (i.e. ultrasound contrast agent). An overview of ultrasound contrast agents including key studies in the literature concerning their usage, size, and formation is given in section §3.2. The chapter then describes the materials and the protocol developed to test whether candidate nanoparticles are gas-filled nanobubbles. The protocol is based on evaluating the compressibility and density of nanoparticles. Details of these methods and the findings when they were applied on the ultrasound contrast agent sample is discussed in sections §3.3 and 3.4 respectively.

3.2 Background of Ultrasound Contrast Agents

Contrast in ultrasound imaging arises from the dissimilar acoustic properties of different tissues. The acoustic properties of bubbles is very different to that of tissues and fluids, therefore imaging contrast can be enhanced by using bubbles as ultrasound contrast agents. Microbubble preparations such as Definity (Lantheus Medical Imaging) and Optison (GE Healthcare) are used clinically as image contrast agents and are currently approved by the Food and Drug Administration (FDA) for use in the United States [121]. As microbubbles are removed by the vasculature, nanobubbles are being investigated as a means to improve the lifetime *in-vivo* of ultrasound contrast agents [5,6,8]. The high acoustic impedance mismatch between the gas and surrounding tissues or fluids causes strong ultrasound scattering. Further, the response of bubbles to an ultrasound field is more complex than other tissues [121]. Microbubbles resonate symmetrically when exposed to low acoustic power. However, at intermediate acoustic power, the expansion and contraction phases became unequal which results in nonlinear behaviour. On the contrary, tissues have a linear behaviour due to their comparative incompressibility.

Microbubble ultrasound contrast agents utilize bubbles that are less than 10 μm in diameter [169]. They consist usually of a perfluorocarbon gas of low solubility (e.g C_3F_8, 5.7 mg/l at 15 ˚C) [170] and a polymer, protein, or lipid shell[169]. Due to their low solubility in blood, perfluorocarbon gasses are typically used over other common gasses such as nitrogen or oxygen in ultrasound contrast agents. The role of the shell of the bubble is to provide impermeable layer leading to a substantial drop in the surface tension, which results in near-zero Laplace pressure. This will satisfy the equilibrium between the chemical potential of the gas inside and outside the bubble and extend their lifetime (for details, see §1.3.1). Coated lipid microbubbles can also be fabricated for drug delivery by incorporating lipids with head-groups that specifically bind the drug [124,125]. The presence of the shell differentiates the ultrafine bubbles used as ultrasound contrast agents from most other reports of bulk nanobubbles.

There has been considerable interest in the formation of sub-micron bubbles for ultrasound imaging or drug delivery applications. They are of particular interest because smaller bubbles more easily pass through the vasculature due to their small size [3–8]. It is a challenge to produce very small bubbles of controlled size, however some groups have reported the production of bubbles in the nanometer size range. Yin *et al*. fabricated lipid nanobubbles with an average size of 436 nm and studied their echogenic properties both *in vitro* and *in vivo* [8]. They demonstrated that nanobubbles provided a greater contrast enhancement than microbubbles. Further, the smaller bubbles exhibited an extended lifetime *in vivo*. The enhancement obtained using microbubbles lasted for 15 minutes, whereas that obtained using nanobubbles lasted for an hour. Krupka *et al*. developed a method to decrease the size of nanobubbles from 881 ± 127.6 nm to 208 ± 74.7 nm and showed that the addition of a pluronic copolymer enhanced echogenicity and stability [171]. Recently Gnyawali *et al*.[172] have developed a microfluidic technique to decrease the size of suspended encapsulated microbubbles by using a vacuum to

extract air from liquid as it flows through microchannels. Tuning the vacuum pressure enabled them to reduce the bubble size from 100 μm to 1 μm. Applying similar techniques to nanobubbles could potentially produce contrast agents of controlled size in the nanobubble size range.

3.3 Materials and Methods

High grade purified water (ELGA purelab Chorus 3 system with resistivity 18.2 MΩ) was used for all investigations. D_2O was purchased from Sigma-Aldrich (Aldrich no: 151882, 99.9 atom % D). D_2O and water were filtered through filters (0.02 μm Whatman Anotop 10 inorganic with an Al_2O_3 membrane) before use. The filters themselves can be a source of nanoparticles, therefore 10 mls of pure water was passed through the filters to rinse them before use. All glassware was cleaned with 10% NaOH (AR Grade, Aldrich) for 10 min and rinsed copiously with purified water, before being used.

3.3.1 Ultrasound Contrast agent

A commercial ultrasound contrast agent (Definity ®, Lantheus Medical Imaging) was used in this study. Once activated the ultrasound contrast agent contains nanobubbles of octafluoropropane (C_3F_8) in the gaseous state with an outer lipid shell consisting of (R) – hexadecanoic acid, 1-[(phosphonoxy)methyl]-1,2-ethanediyl ester, monosodium salt (DPPA, Mwt 670 Da); (R) -4-hydroxy-N,N,N-trimethyl-10-oxo-7-[(1-oxohexadecyl)oxy]-3,4,9-trioxa-4-phosphapentacosan-1-aminium, 4-oxide (DPPC, MWt 734 Da), and (R)-∝-[6-hydroxy-6-oxido-9-[(1-oxohexadecyl)oxy]-5,7,11-trioxa-2-aza-6-phosphahexacos-1-yl]-ω-methoxypoly(ox-1,2-ethanediyl), monosodium salt (MPEG5000 DPPE, Mwt ~5750 Da). The contrast agent is supplied

in 2 ml clear glass vials that were stored at 4 ˚C before activation. According to the manufacturer, each vial initially contains 6.52 mg/ml of octafluoropropane in the headspace and 0.75 mg/ml of the lipid mixture in water. One ml of the clear liquid contains 0.75 mg lipid mixtures consisting of 0.045 mg DPPA, 0.401 mg DPPC, and 0.304 mg MPEG5000 DPPE; 103.5 mg propylene glycol; 126.2 mg glycerin; 2.34 mg sodium phosphate monobasic monohydrate; 2.16 mg sodium phosphate dibasic heptahydrate; and 4.87 mg sodium chloride in water.

The ultrasound contrast agent is a colourless clear liquid prior to activation by mechanical agitation (see panel A in Figure 3-1). Each vial was equilibrated at room temperature before being mechanically agitated for 45 seconds using a mechanical shaking device, (Vialmix®, Lantheus Medical Imaging) according to the manufacturer's instructions, to produce a milky white suspension as shown in the right image in panel A. A 1 ml glass syringe equipped with a 24 gauge needle was used to withdraw the suspension. According to the manufacturer, 1 ml of activated Definity® suspension contains 1.2×10^{10} lipid coated octafluoropropane bubbles and approximately 1.1 mg/ml of C_3F_8. Panel B and C shows a schematic representation of the ultrasound contrast agent and the molecular structures of the three lipids present.

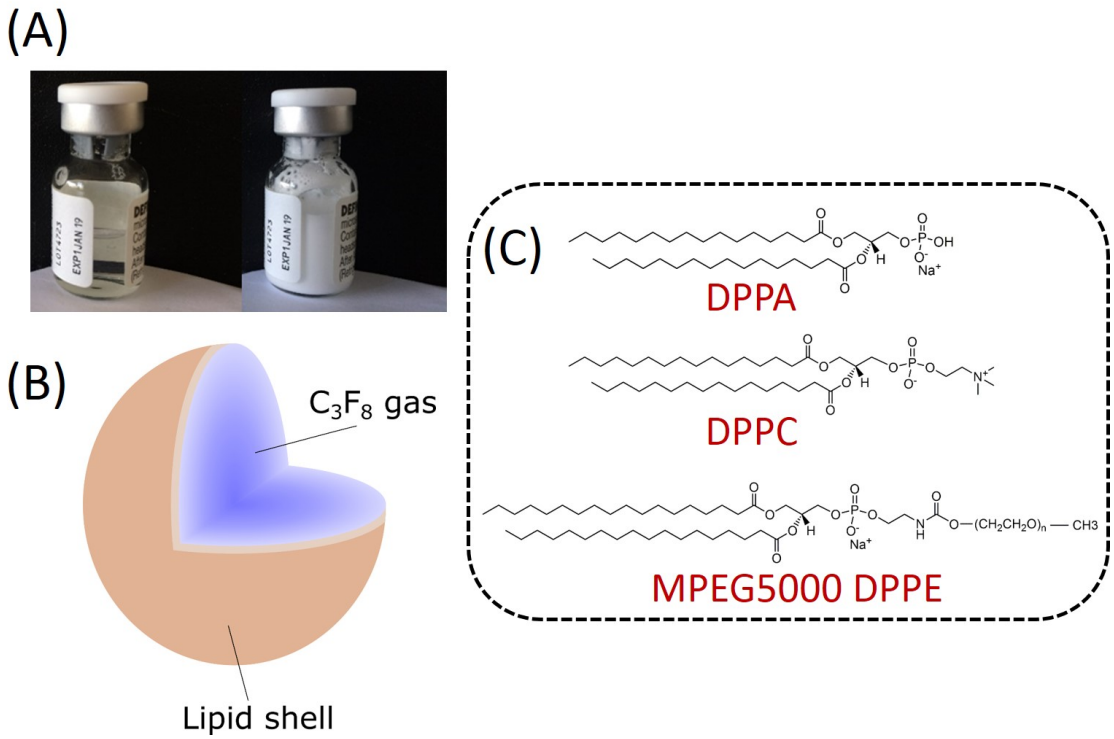

Figure 3-1. Schematic representation of Definity® ultrasound contrast agent. Panel A shows the ultrasound contrast agent before agitation (left) and after mechanical agitation (right). The vial was activated by mechanical agitation for 45 seconds using a mechanical shaking device (Vialmix®, Lantheus Medical Imaging). The activated contrast agent contains bubbles of octafluoropropane gas and a shell consisting of a mixture of three lipids (panel B). The lipids are DPPA, DPPC, MPEG5000 DPPE (panel C) with the following empirical formulas $C_{35}H_{68}O_8PNa$, $C_{40}H_{80}NO_8P$, and $C_{265}H_{527}NO_{123}PNa$ and molecular weights of 670, 734, and ~ 5750 Da. The large hydrocarbon groups contained within these lipids ensures that their solubility in water is low.

3.3.2 Resonant Mass Measurement

An Archimedes (Malvern Instruments, UK) was used to measure the size and buoyant mass of bubbles in the ultrasound contrast agent at room temperature. ParticleLab software (version 1.2) provided by Malvern was used to process all measurements in this study. RMM sensors were calibrated prior to measurement with a polystyrene standard containing spheres 508 ± 8 nm in

diameter (Thermo Fisher Scientific). Nano sensor chips with internal channels having a square cross section of $2 \times 2\ \mu m^2$ were used in all measurements. The threshold frequency change for identifying a particle was set to 0.025 Hz for bubble measurements, based on the observed baseline noise value at 0.15 Hz.

3.3.3 Dynamic light scattering on samples under Pressure

A Zetasizer Nano ZS (Malvern) was used with a purpose built apparatus for applying external pressure to a cuvette containing the sample during measurement. A schematic of the apparatus is shown in Figure 3-2. The pressure within a cuvette placed in the Zetasizer Nano ZS (Malvern) was modified by action of the plunger, which compresses the gas in the syringe (10 ml gas tight syringe equipped with purpose-built holder) and measured using a commercial pressure sensor (PE3004, IFM Efector). Polyetheretherketone (Peek) tubing (Chromalytic Technology PTY Ltd), was used to connect the syringe to the cuvette. Tubing with a narrow internal diameter (0.5 mm) was chosen to minimize the dead volume. The absolute pressure was controlled from 1 atm up to 10 atm to enable size measurements under a larger pressure range during the pressurisation and depressurisations process. A cuvette with a 5-mm path length and 0.875-mL volume (23-5.45-Q-5, Starna cells, US) was placed in the Zetasizer during the measurement. This cell was glued inside a metal adaptor (FCA5, Starna cells, US) enabling it to withstand up to 10 atm of gauge pressure. A similar cell without the metal adaptor, withstood up to 6 atmospheres of pressure before failing. Note, due care should be taken when dealing with vessels under pressure. The size of nanoparticle dispersions within the cuvette were determined at 25°C at both 1 atmosphere and elevated pressures. Henry's law states that the solubility of gas is proportional to pressure, therefore one would expect that this leads to dissolution of gas from the head space above the cuvette. As this dissolution process is slow compared to the timescale of the measurements in this study, we believe it had no effect on our measurements.

Further, the pressure readings once adjusted were very stable, indicating that an insubstantial fraction of the gas in the headspace dissolved within the timescale of the measurement.

For all dynamic light scattering measurements 13 runs of 10 s were performed to obtain a single particle size distribution on a sample in a cuvette with a 5 mm path length and 0.875 ml volume. Size measurements of nanoparticles in ultrasound contrast agent were commenced 15 min after activation. The measurements were made with automatic attenuation at a position of 4.65 mm from the cuvette wall and analysed using the Malvern Zetasizer software version 7.1.

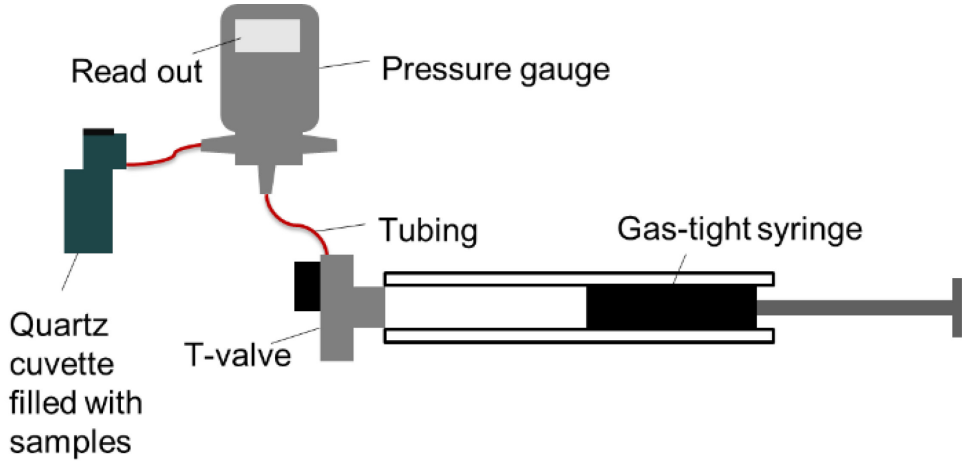

Figure 3-2. A schematic of the apparatus used for performing light scattering on samples under an applied external pressure. The cuvette was inserted inside the light scattering instrument during measurement and the pressure measured using a commercial pressure gauge. Pressure was applied to the cuvette by activating the plunger of the gas-tight syringe. A T-valve was used to select between the application and release of pressure.

3.4 Results and Discussion

The lifetime and bubble size of the activated ultrasound contrast agents were measured. It was reported by the manufacturer that this ultrasound contrast agent suspension can be used for up to 12 hours after activation, indicating that the dispersions are stable for at least this long. The size of the nanoparticles was measured by light scattering over a period of 200 minutes as shown

Figure 3-3, with the diameter initially rising to nearly 1000 nm and then falling to ~ 800 nm. The cuvette containing the solution of interest was placed inside the instrument and left undisturbed during these measurements. The milky white appearance of the dispersions suggests that the multiple scattering could affect the reliability of the measurement. However, the automatically set measurement position was 4.65 mm from the cuvette wall. For highly concentrated samples the measurement position will be shifted closer to the wall (<<1 mm) to minimize multiple light scattering. This indicates that the concentration of nanoparticles (reported to be <1.2 x10^{10} particles ml^{-1}) is not so high as to render the light scattering measurements unreliable.

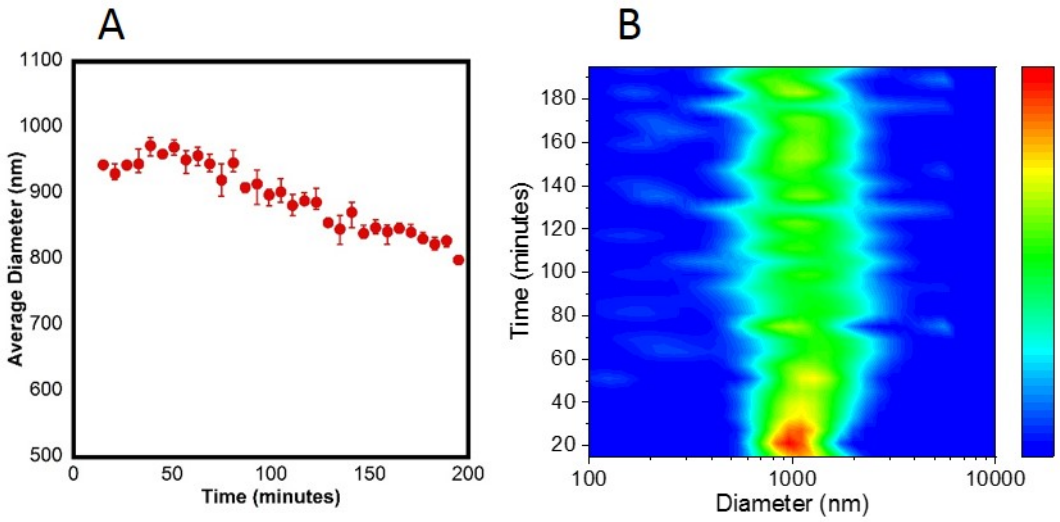

Figure 3-3. Panel A: Average diameter of nanoparticles in the ultrasound contrast agent as a function of time. The diameter initially increased, then decreased gradually with time. Each data point here is the average of three measurements. The error bars represent the maximum and minimum values. Panel B: Contour plot of the corresponding Intensity weighted distributions over the same time (the colour scale is shown next to the figure, where the top corresponds to the highest intensity (i.e. peaks) and the bottom corresponds to the lowest intensity). For Data DOI:10.25911/5b9b54301e67f

3.4.1 Effect of external pressure

As gas is highly compressible, bubbles respond to the application of an external pressure, whereas solid particles and liquid droplets, which are almost incompressible are unchanged at moderate pressures. In the case of a nanobubble without a shell, the change in radius, *r*, due to application of an external pressure, P_{ext}, can be calculated using the Laplace pressure and assuming the gas behaves ideally, using equations 3.1 & 3.2. In this calculation, the number of moles of gas within a bubble, *n*, is calculated under an external pressure of 1 atmosphere and assumed to be unchanged with external pressure. The effect of external pressure on bubble radius requires an iterative calculation as the bubble radius impacts the Laplace pressure. The calculated effect of external pressure on the diameter of a bubble as a function of pressure is shown in Figure 3-4.

$$P_{total} = P_{ext} + \frac{2\gamma}{r} \quad (3.1)$$

$$r^3 = \frac{3nRT}{4\pi P_{total}} \quad 3.2)$$

Where, P_{total}, is the total pressure inside a spherical nanobubble and γ is the interfacial tension, *R* is the ideal gas constant (8.314 Pa m^3 mol^{-1} K^{-1}) and *T* is the temperature in Kelvin.

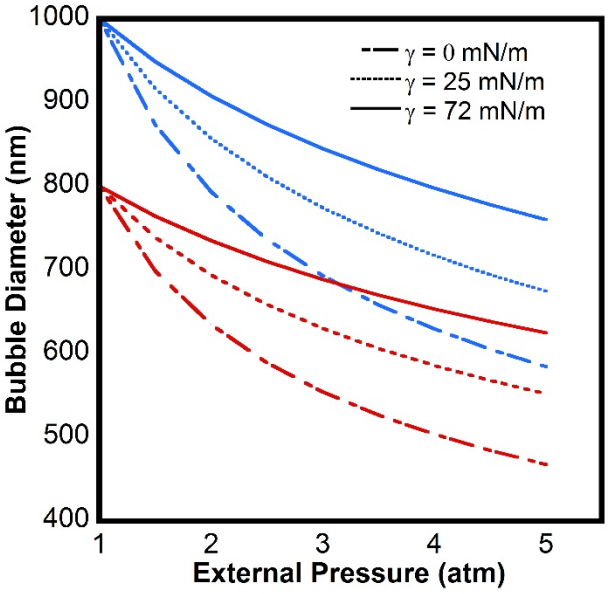

Figure 3-4. The calculated effect of external pressure (equations 3.1 & 3.2) on the diameter of a bubble without a shell, with an initial diameter of 1000 nm (blue) and 800 nm (red) as a function of external pressure, for nanobubble-solution interfacial tensions of $\gamma = 0$ mN m^{-1}, $\gamma = 25$ mN m^{-1}, (approximation of the air-water interface with liquid phase phospholipids [173]) , and $\gamma = 72$ mN m^{-1} which is equivalent to the surface tension of pure water at 25°C. For Data DOI: 10.25911/5b9b578b8040c

In the case of an armoured nanobubble, the calculation in Figure 3-4 is invalid here because the shell is expected to provide an additional mechanical resistance to the reduction in size when external pressure is applied. Here we applied an external pressure to the dispersion of armoured nanobubbles and measured the change in size using light scattering. The dispersion was placed in a cuvette, which was connected to the pressure apparatus described above. The reduction in size for lipid coated nanobubbles was found to be more significant the higher the pressure (see Figure 3-5).

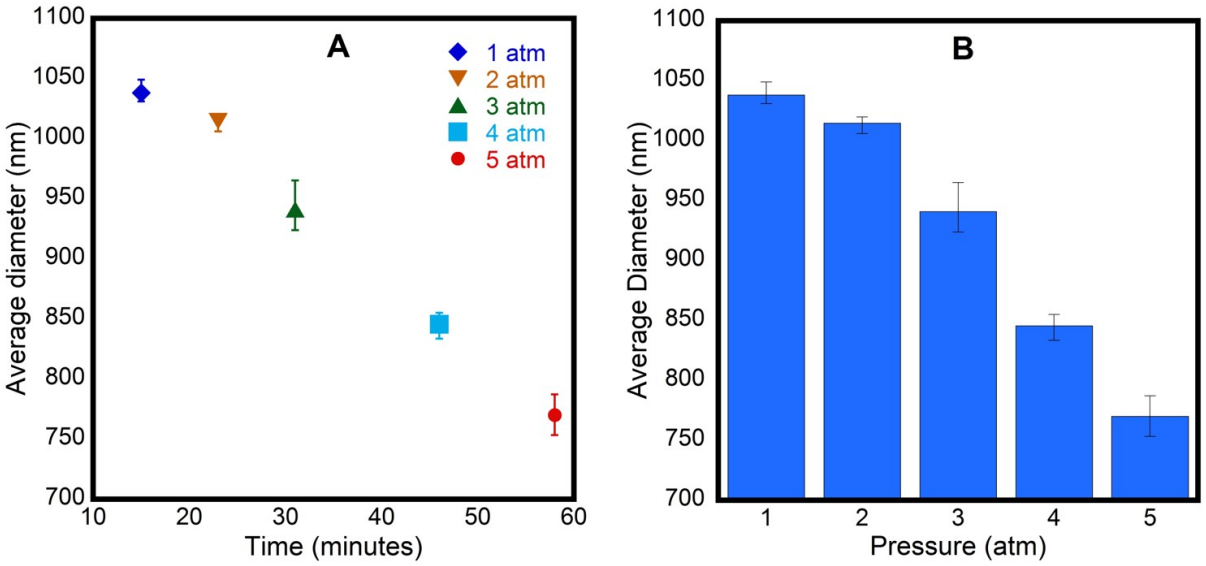

Figure 3-5. Experimentally measured effect of external pressure of 2.0 ± 0.1 atm, 3.0 ± 0.1 atm, 4.0 ± 0.1 atm, and 5.0 ± 0.1 atm on the diameter of a nanoparticle dispersion containing lipid coated nanobubbles using dynamic light scattering. The average diameter is shown as a function of the actual passage of time (panel A), and as a a function of the external pressure (panel B) on the horizontal axis. The average particle diameter decreased as the external pressure increased, in line with expectations for a dispersion containing nanobubbles. Each data point here is the average of three measurements. The error bars represent the maximum and minimum. Note the change in average diameter is not attributed to the passage of time; cf with Figure 3-3.

It is important to note that octafluoropropane condenses to a liquid at 298 K when an external pressure of $\geq$ 8.7 atm is applied [174]. Therefore the applied external pressure was limited to 5 atm for the data presented in Figure 3-5 and in the cycling of the external pressure between 1 atm and 5 atm, as shown in Figure 3-6. If a Laplace pressure is acting, it will be no more than 1.5 atm, which means the total pressure within the bubbles is < 6.5 atm which ensures that the pressure is insufficient to condense the octafluoropropane in these experiments.

Following the time sequence from left to right in Figure 3-6, the initial size (Marked A) was 836 nm under normal atmospheric pressure. Upon increasing the external pressure to 5.0 ± 0.1 atm (B) the mean size decreased to 787 nm. If these bubbles were uncoated, the size would be

expected to decrease to 574.5 nm for a surface tension of 25 mN m^{-1}. The measured reduction in size is considerably smaller than what is expected for a naked nanobubble and substantially greater than expected for a solid or liquid particle. The smaller than expected reduction in size is attributed firstly to the presence of a significant number of particles (~ 40%, see Figure 3-9) in the dispersion that are not nanobubbles and therefore unaffected by pressure and secondly to the mechanical resistance of the lipid shell. As the lipids are highly insoluble in water, they are effectively trapped at the air-water interface and can therefore form a robust shell. Upon decompression to 1.0 atm, the z-average diameter increased to 921 nm, indicating an expansion of nanobubbles in response to the reduction of pressure (C). What is surprising is that the average size measured upon decompression initially exceeds the size before compression, before it decreases to 825 nm. Upon increasing the pressure to 5.0 ± 0.1 atm again, (D) the size decreases substantially to ~ 600 nm, which is substantially smaller than the size measured upon the initial application of 5.0 atm of pressure. Upon another decompression to 1 atm (E), the z-average diameter again increases substantially before a reduction in size back to the levels before decompression. A further application of 5.0 ± 0.1 atm of pressure (F) sees a further reduction in size to ~ 400 nm which is unchanged with further cycles of pressure change (G, H, I). In interpreting this data, it is important to remember that these measurements are the average diameter of a population of nanobubbles and non-buoyant nanoparticles as shown in Figure 3-9 (see below). The non-buoyant particles are not gas filled and therefore it is expected that they do not respond in a measurable way to the changes in pressure, so their presence in the sample has the effect of reducing the average measured change in size with changes in pressure.

In the initial pressure cycles a subpopulation of nanobubbles are responding to the pressure changes whilst the heavy particles are unaffected. Decompression is likely to damage the shells of some nanobubbles causing these nanobubbles to grow to a larger size before being quickly eliminated from the measured population – possibly by growing further and being removed by

buoyancy or by dissolution. Each cycle produces a reduction in the average size, suggesting that the shells of the larger nanobubbles are selectively more likely to suffer damage on decompression. This indicates that the shells of smaller bubbles are more robust. After several cycles of pressure changes no further changes in size were observed (see Figure 3-6; F, G, H, I), indicating that the shells of the remaining population of nanobubbles are sufficiently robust to resist any effect of external pressure or that no nanobubbles remain and the particles being measured are nanoparticles not nanobubbles, as indicated in the resonant mass measurement (see Figure 3-10). These effects were reproducible in different samples of the same vials and from different vials (see Appendix, §A.2).

It is notable that when the pressure is released the size of the particles is initially greater than the initial size as indicated by the first data points at (C) and (E) in Figure 3-6 which are greater than the data at (A). A possible explanation is that when the pressure is released the expansion of the bubble results in damage to the lipid shell. These bubbles are then free to grow if the solution is supersaturated to a size where they are sufficiently buoyant to be removed from solution. This process happened relatively fast (< 2 minutes) as it was only observed in the first measurement after decompression (see C and E).

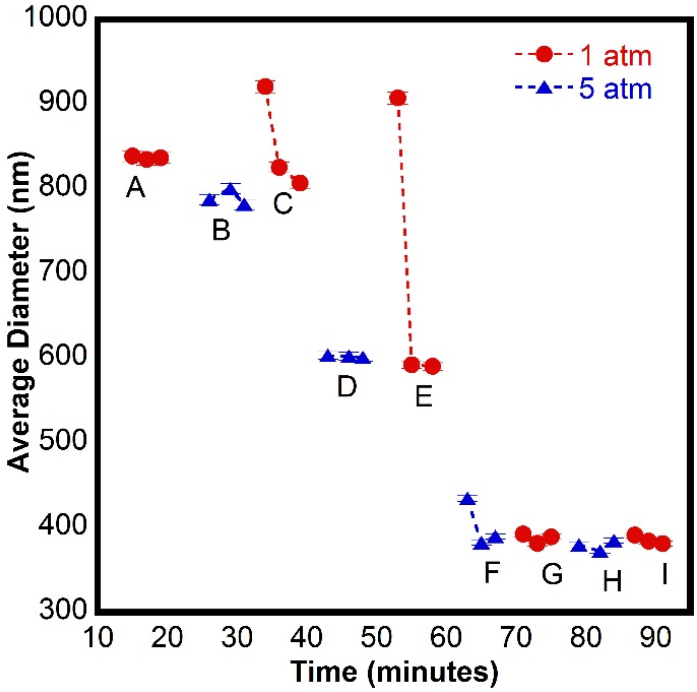

Figure 3-6. Experimentally measured effect of pressure cycling between an external pressure of 1.0 atm and 5.0 ± 0.1 atm on the diameter of a nanoparticle dispersion containing lipid coated nanobubbles using dynamic light scattering. The red points and the blue points represent the z-average diameter at 1.0 atmosphere and 5.0 atmospheres of pressure respectively. Each data presented in this figure is a single measurement. Each point represents a single measurement as the change in size was relatively fast when depressurizing the sample. The error bars shown are for 1 standard deviation calculated from the average of the relative standard deviation of all the data shown in Figure 3-3A. For Data DOI: 10.25911/5b9b5ba064e36

3.4.2 Pressure induced Condensation

Perfluoropropane will condense when a total pressure of 7 atmospheres is applied at T= 290.5 Kelvin. Therefore, when sufficient external pressure is applied, it is expected that the contents of the nanobubbles will condense into a liquid, resulting in a step change in size. To examine this, we applied an external pressure of 7.0 ± 0.1 atmospheres to a sample at 298 K and monitored the number average size as the temperature was decreased. The data is shown in Figure 3-7A. There was an initial significant reduction in size from 856 nm to 640 nm upon application of 7.0 ± 0.1 atm of pressure at 298 K (not shown in the plot). Then, the size was initially stable with decreasing temperature down to 290 K. Then the average size decreased between 288 K and 284 K, which was attributed to condensation of Perfluoropropane.

To understand the behaviour of these encapsulated gas bubbles the phase diagram of Perfluoropropane (C_3F_8) as reported by Brown [174] is shown in Figure 3-7B. Based on Figure 3-7B, the gas should have condensed at 290.5 K when the total pressure is 7.0 atm. (vertical black line). However, the size data indicates that condensation did not occur until the temperature dropped below 288 K. This is attributed to the shell of the ultrasound contrast agent effectively reducing the pressure on the gas within the bubble. The observed transition in size occurred between 290 K and 286 K, which corresponds to condensation in the phase diagram at pressures of 6.9 - 6.2 atm indicating that the lipid shells were able to withstand between 0.1 and 0.8 atm of pressure. This can be seen as an effective negative Laplace pressure.

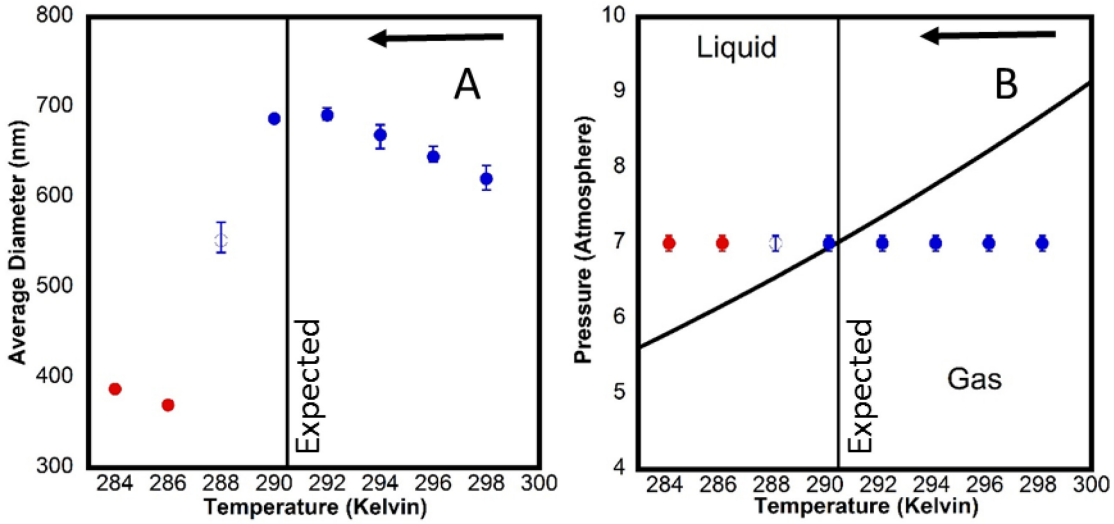

Figure 3-7. Panel A: Average diameter of the particles in the ultrasound contrast agent measured as the temperature was reduced from 298K to 284K under an applied pressure of 7.0 ± 0.1 atmospheres. Each data point here is the average of three measurement. The error bars represent the maximum and minimum values. Panel B: The phase diagram for Perfluoropropane gas C_3F_8, with the same data as panel A shown. The vertical line represents the expected condensation temperature at the applied pressure, based on the phase diagram for bulk perfluoropropane [174], whereas the non-filled and red circles highlight those measurements that show a substantially smaller size. The data points are coloured to aid in comparison between Panel A and Panel B. For Data DOI: 10.25911/5b9b5c93b96e7

The properties of lipid coated microbubbles under pressure was studied by Mountford *et al*.[175] They investigated the pressure required to condense aqueous suspensions of lipid-coated gas-filled microbubbles containing perfluorobutane gas and observed that the vapour to liquid transition in a bubble was shifted to higher pressures by up to 1.4 atm compared to the bulk phase. They concluded that the lipid shell provided mechanical resistance under compression. The extra pressure required in our experiments to induce a phase change is consistent with these findings.

It is well known that the surface energy of the air-water interface can be reduced by the addition of lipids to the interface and that for insoluble lipids the surface energy can be further reduced by compression of the interface as occurs on a Langmuir trough. As the lipids are insoluble they remain at the air-water interface and the area occupied by each lipid molecule is reduced when the area of the surface is reduced. The effect on the interfacial tension can be measured using a Langmuir trough and is usually presented as a surface pressure (Π)-Area isotherm. This can be converted to the lipid-vapour interfacial tension-Area isotherm by the expression

$$\gamma_{lv} = \gamma^0_{lv} - \Pi \qquad (3.3)$$

where Π is the surface pressure and γ_{lv} is the interfacial energy of the lipid coated water-vapour interface and γ^0_{lv} is the interfacial energy of the pure water-vapour interface. For DPPC we have taken the data from [176], and calculated the lipid water interfacial tension as a function of area per molecule (see Figure 3-8). Note the interfacial energy at very high compression is not available as this technique is incapable of measuring negative surface energies. The evidence above suggests that the reduction in area of the interface of a shrinking bubble can compress the lipids on the surface sufficiently to generate a negative surface tension, this would occur when the area per molecule drops below 40 Å^2. In order to produce a negative Laplace pressure

of up to 0.8 atm the negative surface tension may be as large as 0.015 N m^{-2}. This could also occur in oil-in-water emulsion systems for oil droplets coated with water insoluble surfactants, thereby reducing the rate of Ostwald ripening. It is worth noting that at high values of Π, monomolecular lipid layers can buckle or fail. If this failure is defect induced, it may be dramatically reduced on the surface of a nanobubble due to the very small surface area (~ 1.0 x 10^{-12} m^2), allowing substantially higher surface pressures to be obtained on a nanobubble interface than are accessible on a Langmuir trough.

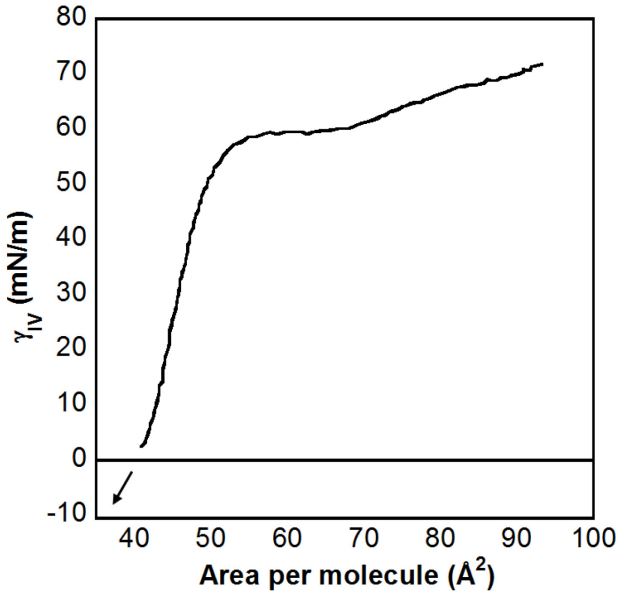

Figure 3-8. Liquid-Vapour interfacial energy, γ_{lv}, versus area per molecule for DPPC calculated using equation 3.3 and surface pressure values from[176]. The arrow here indicates the influence that further compression of the molecules by either application of an external pressure or loss of gas from the nanobubble would have on the area per molecule of the lipid at the interface in the absence of buckling of the interfacial film. It can be seen that the interfacial tension effectively becomes negative when the area per molecule is reduced below ~40 Å^2. For Data DOI: 10.25911/5b9b5d3cbe522

3.4.3 Resonant Mass measurements

The size of the bubbles in the ultrasound contrast agent were measured and characterized using resonant mass measurement. Due to the high concentration of bubbles it was necessary to dilute the sample by a factor of 50 to allow single particles to be registered as they passed through the microfluidic channel. This prevents miscounting two individual particles as a single particle. Dilution was made with water. The population of positively buoyant nanoparticles was measured at a concentration of 8.79×10^7 particles/ml (see Figure 3-9) in the diluted sample, this corresponds to an undiluted bubble concentration of 4.4×10^9 particles/ml. The average buoyant mass for these bubbles was 23.7 ± 1.6 fg. These bubbles have a broad distribution as shown in the inset figure. A significant population of negatively buoyant particles (which are denser than water and therefore not bubbles) were detected in the same sample (see Figure 3-9). The mean buoyant mass for these particles was -1.9 ± 0.1 fg. The concentration of non-buoyant particles was 5.28×10^7 particles/ml. These negatively buoyant particles have been attributed to lipid structures [115,177]. It is worth noting that dilution has a significant impact on bubble stability, this may in part be due to a reduction in ionic strength and a corresponding increase in lipid solubility leading to a reduction in the stability of the lipid shell. It was observed that the concentration of diluted bubbles decreases significantly over time. The concentration of diluted bubbles after 120 minutes was measured to be less than 4 % of the original population at the beginning (see Figure 3-10). On the contrary, heavy particles were found to be stable and at least 60 % of their population lasted for 120 minutes. The resonant mass measurement technique can distinguish between buoyant and non-buoyant populations of particles enabling them to be investigated separately, whereas the light scattering measurements made with the zetasizer reported above include all of the particles present.

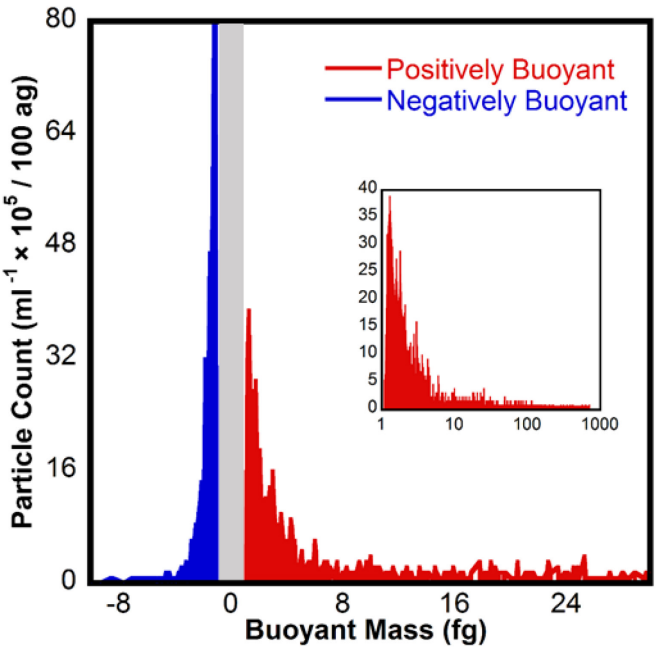

Figure 3-9. Representative size distributions using the resonant mass measurement method for positively buoyant particles (red, RHS) and negatively buoyant particles (blue, LHS) in the ultrasound contrast agent diluted 50 times with filtered water. The whole distribution for the positively buoyant bubbles is shown in the inset using the same units but the abscissa axis is presented using a log scale. A total of 1158 buoyant particles and 696 negatively buoyant particles were measured over 20 minutes. The grey shaded region indicates a region in which particles cannot be measured due to the limit of sensitivity of the instrument. For data DOI: 10.25911/5b9b5de680dd5

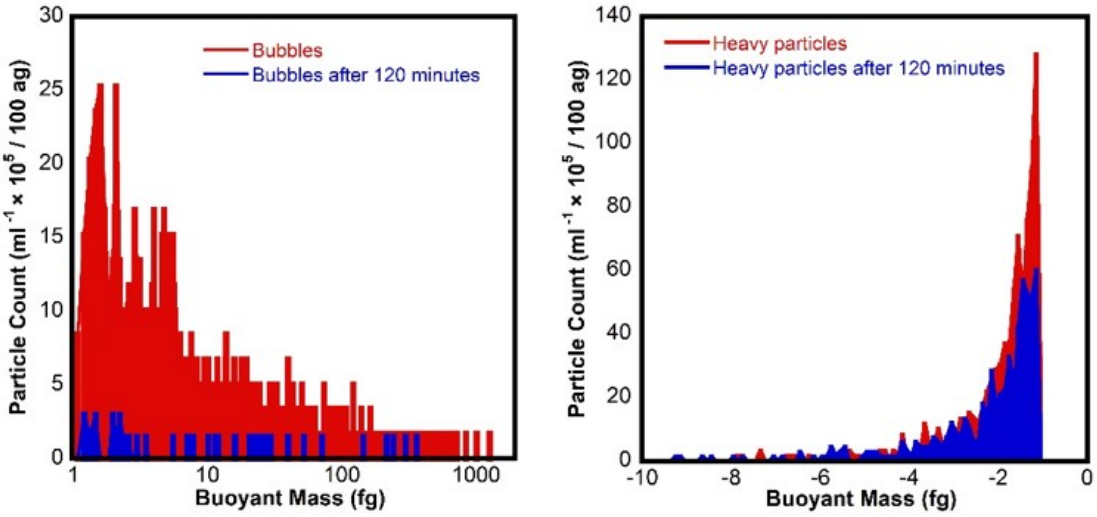

Figure 3-10. A histogram showing the particle concentration measured using the Archimedes for positively buoyant bubbles (left) and negatively buoyant particles (right) initially and after 120 minutes have elapsed. The concentration of bubbles dropped significantly from 1.67 x 10^8 particles/ml to 0.06 x 10^8 particles/ml. The negatively buoyant particles decreased far less from 0.87 x 10^8 particles/ml to 0.62 x 10^8 particles/ml. A total of 1000 buoyant particles and 516 negatively buoyant particles were measured over 10 minutes for the initial measurement, and a total of 40 buoyant particles and 414 negatively particles were detected after 120 minutes had elapsed. For data DOI: 10.25911/5b9b5e70bad30

3.4.4 Measuring the density of nanoparticles

Several groups have reported density determinations using RMM on cells, proteins, standard particles, and silicon oil droplets [158,162,178]. In this approach the mean buoyant mass is measured in solvents of different density. Interpolation or extrapolation of the data to zero buoyant mass yields the particle density, as shown in Figure 3-11. At zero buoyant mass the density of the particle is equivalent to the density of the solvent.

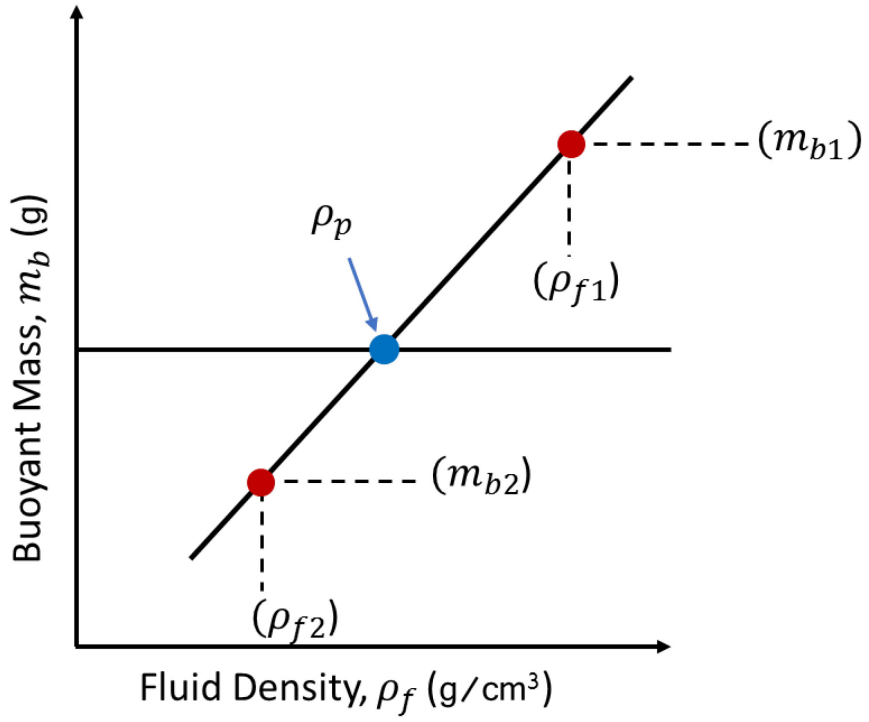

Figure 3-11. The density of suspended particles can be determined from the mean buoyant mass m_b for dispersed particles that are measured in at least 2 fluids of different densities (ρ_{f1}, ρ_{f2}). Extrapolating or interpolating a line that passes through the experimental measurements {(ρ_{f1}, m_{b1}) and (ρ_{f2}, m_{b2})}, to zero buoyant mass enables the mean density of the particles to be determined.

The density of 508 ± 8 nm polystyrene latex particles of known density was measured in order to check the accuracy of this method. The buoyant mass of latex nanoparticles was measured in aqueous solutions in which the ratio of H_2O to D_2O was varied in order to vary the density of the solvent whilst minimizing changes to the chemical nature of the solvent. Extrapolating the mean buoyant mass for these particles to zero buoyancy as shown in Figure 3-12 yielded a density of 1.052 ± 0.006 g/cm^3, which is equivalent to the expected value[3] of 1.055 g/cm^3.

[3] https://www.thermofisher.com/au/en/home/life-science/cell-analysis/qdots-microspheres-nanospheres/idc-surfactant-free-latex-beads/latex-bead-technical-overview.html

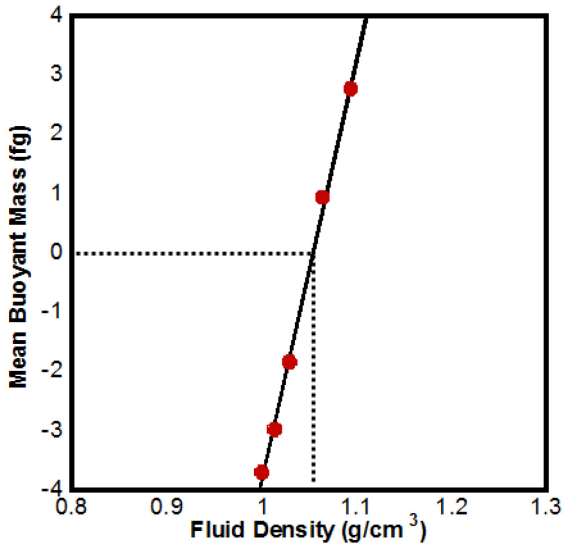

Figure 3-12. The density of 508 ± 8 nm polystyrene latex particles was determined from the x-intercept using regression analysis. Here the density of the particle is equivalent to the density of the solvent when the buoyant mass of a particle is zero. The density of the polystyrene particles was determined to be 1.052 ± 0.006 g/cm^3, which is in agreement with the expected value. The stated error represents the 95% confidence interval. The method for determining the error is provided in Appendix, §A.3

This approach is suitable only when the entire particle size range is within the detection limits of the instrument. Polydisperse samples with particles around the sensitivity limit of the instrument require a different approach, as the sensitivity limit of the instrument is dependent upon both the solvent and particle density. The effect of solvent density on the sensitivity limit can be obtained using equation 2.7 with the minimum detectable buoyant mass. The corresponding particle diameter can then be obtained using equation 2.8. Combining these equations yields an expression for the size of the smallest detectable particle, d_{min},

$$d_{min} = \sqrt[3]{\frac{6L_{mass}}{\pi|\rho_p - \rho_f|}} \tag{3.4}$$

The lower limit of mass detection, L_{mass}, for the nanosensors we are using is typically 350 attograms. The effect of solvent density on the minimum particle size that can be detected in shown in Figure 3-13 for particles with densities corresponding to nanobubbles, polystyrene latex and silica.

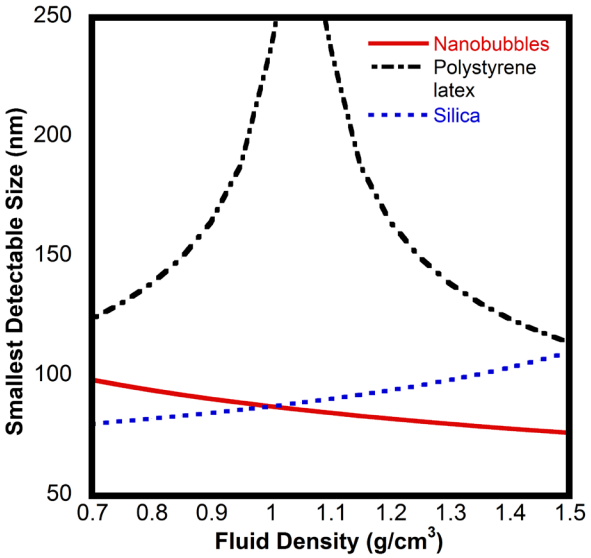

Figure 3-13. The effect of fluid density on the size of the smallest detectable particle that can be measured with an Archimedes using a typical Nano sensor for; nanobubbles (red line, ρ_p = 0.001 g/cm3), polystyrene latex (dashed black line, ρ_p = 1.05 g/cm3), and silica nanoparticles (dashed blue line, ρ_p = 2.0 g/cm^3).

It is necessary to adopt an approach that limits the particle distribution used in the calculation of the buoyant mass to a distribution that is within the detection limits of the instrument. As the sensitivity is dependent on the relative density of the particle and the solvent, the sensitivity limit and therefore the range of particle sizes that are measured changes with the density of the solvent. For buoyant particles, a solvent with a higher density will push the sensitivity limit to a lower range when compared to a solvent of lower density. This could potentially lead to a different population of particles being measured in different solvents. Patel *et al.*[162] recognized this and employed a restricted range of particles for determination of the particle density. This restricted range was chosen based on an iterative calculation in which an estimate of the density

was used to determine which particles were within the appropriate size range and the corresponding mean buoyant mass of these particles was used to revise the particle density until the density converged [162]. This technique required an iterative calculation to select the buoyant mass range and particle density. This is relevant to the determination of the density of nanoparticles in ultrasound contrast agent sample as the particle distribution extends below the sensitivity limit of the instrument. This is shown in Figure 3-9, where it can be seen that the sensitivity limit for the nanoparticles truncates the distribution.

Using this approach to determine the range of particles included in the analysis, the mean buoyant mass of nanoparticles was measured in five different solutions with different ratios of H_2O and D_2O, to produce solvents of different density. A straight line was fit to the data plotted as the buoyant mass versus the fluid density and the density of the particles was obtained from the x-intercept, as shown in Figure 3-11. The analysis technique was tested using polystyrene latex nanoparticles and the determined density was found to agree with the expected value and the value obtained in Figure 3-12 (see Figure 3-14). This method was then applied to determine the density of nanoparticles in the ultrasound contrast agents. However, there were large errors in these measurements and the data was unreliable. This was evident, as data points measured in different ratios of H_2O and D_2O when plotted as mean buoyant mass versus solvent density did not sit on a straight line (see Figure 3-15), despite several attempts using different approaches to address perceived issues. We can speculate as to why these measurements were not reliable. For these measurements to be reliable it is essential that the measurements are made on an equivalent population of particles in each solvent. The data suggests that this was not the case. This could be because: i) Some of the particles that were excluded because they were negatively buoyant in water became positively buoyant in the denser solutions and were therefore counted, ii) The presence of large particles and bubbles in the sample could influence the access of smaller particles to the sensor, particularly if these particles lodge in the entrance

to the microfluidic channel [179] and iii) the short stability of bubbles in the diluted suspensions led to significant changes in the population of nanobubbles on the timescale of the measurement.

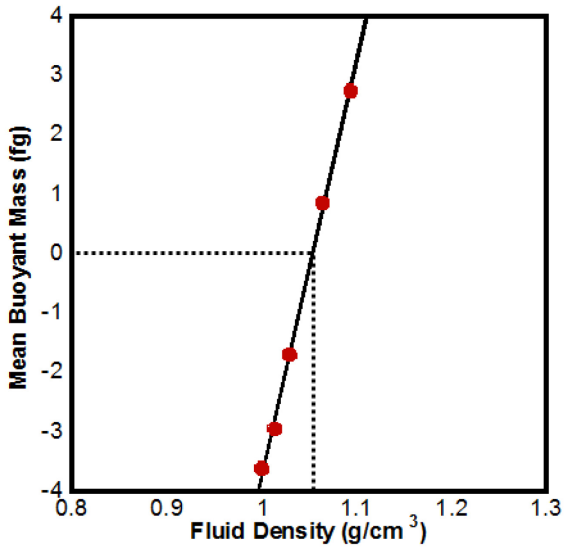

Figure 3-14. Density determination of 508 ± 8 nm polystyrene latex particles using regression analysis based on mean buoyant masses using an iterative calculation. Extrapolating the mean buoyant mass for these particles to zero buoyancy yielded a density of 1.052 ± 0.003 g/cm3, which is in agreement with the result from the simple method given in Figure 3-12 and the expected density of the polystyrene particles.

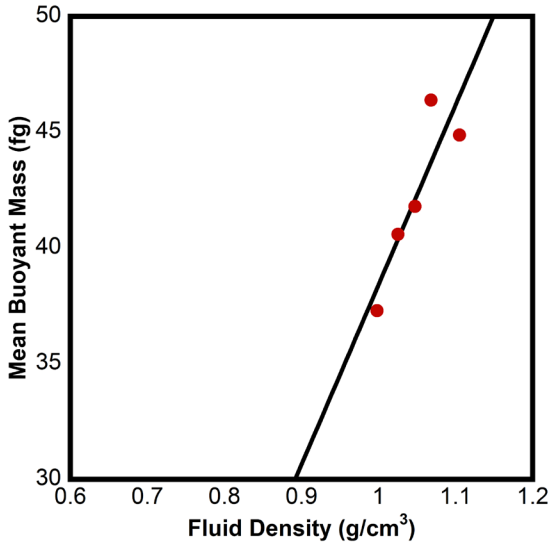

Figure 3-15. Density determination of nanoparticles in an ultrasound contrast agent sample. Here the uncertainty in the determined density was found to be large (i.e. 55% of the determined value), where the density and its corresponding error are 0.89 ± 0.5 g/cm^3.

3.5 Summary

The work presented here shows that pressure studies used to evaluate candidate nanobubbles can be extended to include nanobubbles that are armoured with a shell of surface active material. The pressure results presented here are in agreement with previous work showing that armoured gas bubbles in the size range of 200 to 1500 nm expanded when put under negative pressure and contracted when the pressure was raised to 1 atmospheric pressure[112]. The evidence from the pressure studies performed here and in other work[175] demonstrates that ultrasound contrast agents that utilize armoured bubbles are indeed bubbles and these bubbles are stable for long periods, even when the bubbles are in the nanosize (< 1 μm) range. The pressure studies demonstrate that the lipid shell contributes to the stability of the nanobubbles by negating the Laplace pressure and providing a mechanical resistance to shrinkage. This mechanical resistance is evidenced by the higher pressure required to condense the gas within

a bubble compared to a bulk phase. Moreover the lipid shell likely inhibits the transport of gas across the interface[175]. This has implications for all studies of nanobubbles in bulk as it suggests that the state of the interface plays a major role in the stability. This explanation is consistent with the idea proposed by Ducker [68] to explain the stability of surface nanobubbles. In his model, contaminants that have accumulated at the air-water interface become sufficiently concentrated that upon compression the interfacial energy drops rapidly, leading to the situation where a reduction in interfacial area can lead to an increase in free energy – an effective negative surface tension. The implication is that the purity of water used for the generation of nanobubbles and the introduction of impurities from the generation process can potentially play a significant role in the stability of any nanobubbles produced, not just those prepared using lipid solutions. The long-term stability of armoured nanobubbles has implications beyond those in the immediate field. Yount *et al*.[112,180] have pointed out that such nanobubbles may be formed in low numbers even in highly purified water and are likely responsible for the cavitation of water well below that expected for homogenous nucleation based on the tensile strength of water [181]. Furthermore, armoured nanobubbles are likely the nuclei for growth of bubbles in supersaturated solutions. Thus armoured nanobubbles may be implicated in the cavitation of water columns in the xylem of plants [32] and in the formation of bubbles that cause decompression sickness[182,183].

3.6 Synopsis

New approaches were developed to test whether candidate nanoparticles are gas-filled nanobubbles. Here, resonant mass measurements were employed to assess the density of candidate nanoparticles and dynamic light scattering was used to size candidate nanoparticles under the influence of external pressure.

The resonant mass measurement showed that the population of the commercial ultrasound contrast agent contains ~ 60 % bubbles and ~ 40 % denser particles. Further, the RMM was implemented here to determine the mean density of nanoparticles, and was found to be accurate for standard polystyrene nanoparticles. However, the short stability of the diluted nanobubbles and the presence of larger particles in the sample affected their determined density, and a reliable measurement could not be determined.

The size of nanobubbles was shown to decrease under elevated pressure. This is clear evidence that the nanobubbles are gas filled. The pressure response is complex due to the mechanical properties of the shell and the damage the shell sustains upon decompression. The shell was found to reduce the transmission of external pressure to the gas within the nanobubbles by up to 0.8 atm., as evidenced by condensation studies. Furthermore, a mechanism was proposed by which bulk nanobubbles can be made stable. Compression of insoluble material at the interface leads to an effective negative surface tension and elimination of the Laplace pressure, thereby removing the driving force for dissolution of gas within a nanobubble. This work has implications for all studies of bulk nanobubbles, as it demonstrates that the change in average size of a nanoparticle dispersion under pressure can be used to test whether the nanoparticles are nanobubbles even for armoured nanobubbles and that contamination either from the solvent or from apparatus can play a significant role in stabilizing bulk nanobubbles.

Chapter 4 Investigating the Existence of Long Lived Bulk Nanobubbles in Commercial Nanobubble Generators

This chapter is reproduced with minor changes from:

M. Alheshibri, V.S.J. Craig, Differentiating Between Nanoparticles and Nanobubbles by Evaluation of the Compressibility and Density of Nanoparticles, J. Phys. Chem. C. 122 (2018) 21998–22007. doi:10.1021/acs.jpcc.8b07174.

4.1 Introduction

There are a growing number of reports in the literature of techniques to produce swarms of long-lived nanosized bubbles. A number of these works have reported the existence of long-lived nanobubbles that have been generated by mechanical means. Exceptional amongst these reports is that of Ohgaki *et al*. who described bulk nanobubbles produced at high concentrations consisting of nitrogen, methane, and argon gas with an average radius of 50 nm, that were stable for two weeks [48]. In other work, Ushikubo *et al*.[49] reported that air nanobubbles and oxygen nanobubbles could be made stable for 1 hour and 15 days respectively. Oh *et al.* [92] described a method to produce bulk nanobubbles by mixing CO_2 gas and water. In this study, they adapted a technique that was used previously on surface nanobubles[66] to investigate the identity of the generated objects. The infrared spectra shows the fine rotational structure characteristic of CO_2 molecules indicating the observed objects are gaseous. However, it was not clear if the spectra

originated from nanobubbles as opposed to larger bubbles or surface nanobubbles. The production of bulk nanobubbles by pressure cycling has also been reported [50,102]. The resonant mass method showed that the particles produced by this method were less dense than water, supporting the assertion that they are gas filled nanobubbles [51].

The experiments presented in this chapter are designed to test whether nanoparticles generated by mechanical means are gas filled nanobubbles. Two different devices designed to generate bulk nanobubble solutions by mechanical means are used. Details of thesis devices and all the related experimental methods are reported in §4.2. The candidate nanobubble dispersions were characterized using NTA, DLS, and RMM. Further, the protocols developed in chapter 3 were applied to nanoparticle samples to test whether these nanoparticles are gas-filled nanobubbles. The rest of the chapter describes the main results and discusses the implications of this work.

4.2 Materials and Methods

High grade purified water (ELGA purelab Chorus 3 system with resistivity 18.2 MΩ) was used for all investigations. D_2O was purchased from Sigma-Aldrich (Aldrich, 99.9 atom % D). D_2O was filtered through a 20 nm filter (0.02 μm Whatman Anotop 10 inorganic with an Al_2O_3 membrane) before use. Prior to use, 10 ml of pure water was passed through the filters to remove any particles from the filter. All glassware was cleaned by soaking in 10 % NaOH for 10 minutes and rinsed copiously with purified water, before being used.

4.2.1 Dissolved oxygen measurement

Dissolved oxygen was measured using an oxygen micro meter (AMT Analysenmesstechnik GmbH, Rostock, Germany) that uses a galvanic dissolved oxygen sensor. The sensor is

composed of three electrodes that are submerged in an electrolyte solution. The sensor electrolyte is separated from the sample by a membrane that is permeable to gasses, whereas liquids, solids and ions are not accessible to the sensor electrolyte. Further, the electrodes are designed in such a manner that they are not polarized by an external voltage as it is used for polarographic sensors[184], but on the contrary they are self-polarized when they are immersed in the solution, leading to more stability and less drift. During dissolved oxygen measurement, the oxygen diffuses to the electrode where it is reduced causing a current to flow that is dependent on the oxygen concentration in the sample. The measured current is converted into a voltage in the range of 0-1500 mV by electronics integrated into the device, and then displayed on the panel meter as a concentration with a response time in the millisecond range.

4.2.2 Surface Tension measurements

The surface tension measurements were carried out at room temperature using a contact angle goniometer (CAM200, KSV, Helsinki, Finland). A 1 ml syringe (Hamilton glass syringe, Hamilton Co, USA) equipped with a 24-gauge needle was used to create a suspended droplet in the air. The surface tension at the liquid-air interface was determined using a pendant drop method by fitting the droplet shape with the Young-Laplace equation.

4.2.3 Bubble Generators

Commercial equipment for the generation of bulk nanobubbles often employs a geometry designed to entrain gas and cause flow driven pressure changes. The flowing solution is subject to oscillations in pressure, to firstly increase the solubility of the gas (high pressure) and subsequently nucleate bubbles (low pressure). In this study two different generators that employ this principal were used. The small-scale generator (SSG) (MA5S, HACK UFB, Japan)

typically produces 200 mls of solution per batch whilst the large-scale generator (LSG) (Ultrafine GALF, IDEC, Japan) produces 20 litres of solution per batch.

After passing through the generator the solution was filtered using syringe filters of 450 nm pore size (0.45 μm KX glass syringe filters, Kinesis) to eliminate any larger bubbles or particles. This is necessary as this removes larger particles or bubbles that may interfere with subsequent measurements. The filtered solution was transferred to a sealed flask prior to characterization. Measurements were commenced within 15 minutes of generation.

4.2.4 Nanoparticle Tracking Analysis

A NanoSight (NS300, Malvern) was used to measure the size and determine the concentration of nanoparticles in solution. Nanosight software (version V3.1) was used to process all measurements. All measurements were conducted at 25°C using a blue laser light source (70 mW, $\lambda = 405$ nm). The sample was inserted into the NanoSight using a syringe pump (flow rate set to 30 in arbitrary units). Each measurement reported here is the average of five measurements, each captured over 60 seconds at 25 frames/s. The parameters used were camera level = 14, threshold = 3, gain = 366, and the viscosity for water at 25°C, 0.888 cP.

4.2.5 Resonant Mass Measurement

An Archimedes (Malvern Instruments) was used to measure the size and buoyant mass of nanoparticles in solution. ParticleLab software (version 1.2) provided by Malvern was used to process all measurements. Standard spherical particles of polystyrene with a diameter of 508 ± 8 nm purchased from Thermo Fisher Scientific were used to calibrate the RMM sensors prior to measurement. For all the work described here, Nano sensor chips with internal channels having a square cross section of 2×2 μm^2 were used. All measurements were performed at

room temperature. Data was acquired for 1 hour or until 300 particles had been measured, as recommended by the manufacturer. The detection threshold was set to be 0.009 Hz.

4.2.6 Dynamic light Scattering

A Zetasizer Nano ZS (Malvern) employing a 633-nm He-Ne laser at a scattering angle of 173°, was used to measure the size of particles in solution by dynamic light scattering. The measurements were made with automatic attenuation at a position of 4.65 mm from the cuvette wall and analyzed using the Malvern Zetasizer software version 7.1. For all measurements, 13 runs of 10 s were performed with at least 5 repetitions to obtain the particle size distribution.

4.3 Results and Discussion

4.3.1 The production and stability of nanoparticles

During operation the nanobubble generators create a large number of micron-sized bubbles, which leave the solution over a few minutes due to buoyancy, leaving a solution containing nanoparticles, generally thought to be nanobubbles. Thus, immediately after the production step, the solution appears milky, due to the high concentration of visible bubbles, but becomes clear after several minutes as the larger visible bubbles rise out of solution (see Figure 4-1).

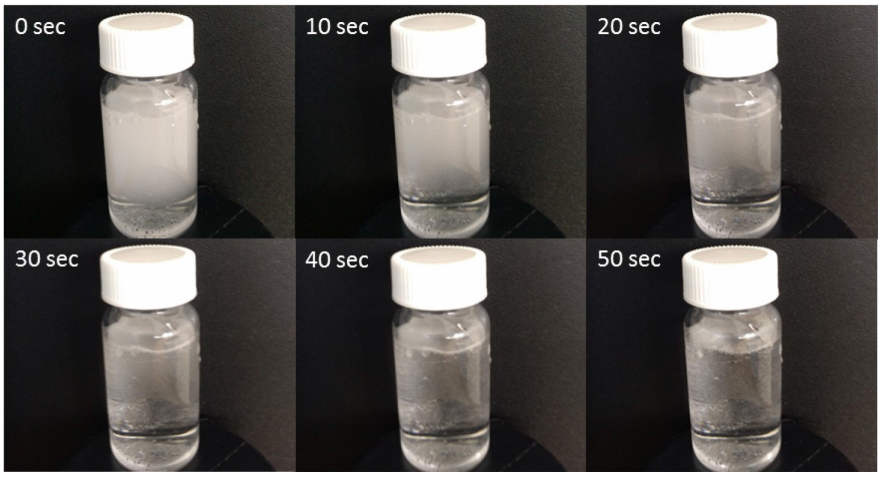

Figure 4-1. Time-sequence images of water treated with the small-scale generator (SSG). Immediately after production, numerous bubbles are present in solution, causing the solution to look cloudy. Because of buoyancy, the larger bubbles rise to the surface and burst, hence the appearance of the solution changes from cloudy to transparent within minutes. Note, some visible bubbles remain attached to the glass wall of the flask.

When the nanobubble generators are operating, the fluid is re-circulated within the generator and therefore subject to many cycles of treatment. The dissolved oxygen concentration was measured before treatment at 25 ˚C, as $[O_2]$=8.50 mg/l. For water treated with the SSG generator for 30 minutes, a similar oxygen saturation was measured ($[O_2]$ = 8.25 mg/l), noting that the solution becomes warm during operation of the SSG (e.g. T= 28-30 ˚C). The dissolved oxygen concentration for water treated with the LSG generator for 30 minutes was measured as $[O_2]$ = 10.50 mg/l, which indicates an increase in the saturation level. The saturation levels of dissolved nitrogen are expected to mimic those of dissolved oxygen.

Treatment with the generators caused a small reduction in the surface tension of solution. After treatment for 30 minutes, the surface tension was measured to be 65.7 ± 2.0 mN m^{-1} and 68.6 ± 1.5 mN m^{-1} for the SSG and the large-scale generator (LSG) treated samples respectively, using water with an initial surface tension of 69.4 ± 0.8 mN m^{-1} (all measured at 20 ˚C). This indicates that a small level of surface-active contamination is introduced during the treatment process.

The effect of treatment time on the concentration and size of generated nanoparticles was measured by nanoparticle tracking analysis (NTA). Panels A and B in Figure 4-2 show the size distribution and concentration of particles as a function of generating time for SSG nanoparticles. The concentration of SSG nanoparticles increased from 410.0 ± 11.5 × 10^6 particles/ml after 5 minutes of generating time to 698.0 ± 12.3 × 10^6 particles/ml after 45 minutes of generating time. The modal size was initially at 86.7 ± 3.4 nm and increased to 117.0 ± 5.6 nm after 45 minutes of generating time. Panels C and D show the size distribution and concentration of particles as a function of generating time for LSG nanoparticles. The concentration for LSG particles increased from 509.0 ± 11.5 × 10^6 particles/ml after 5 minutes of generation time to 774.0 ± 20.9 × 10^6 after 45 minutes of generation time. Unlike SSG nanoparticles, the modal size for LSG generated nanoparticles was unaffected by the generation time. In all subsequent measurements, the generation time for SSG and LSG nanoparticles was between 20 to 30 minutes. The concentration of particles in untreated solution was measured to be less than 1 % of the particle concentration following treatment with the generators (see Figure 4-3).

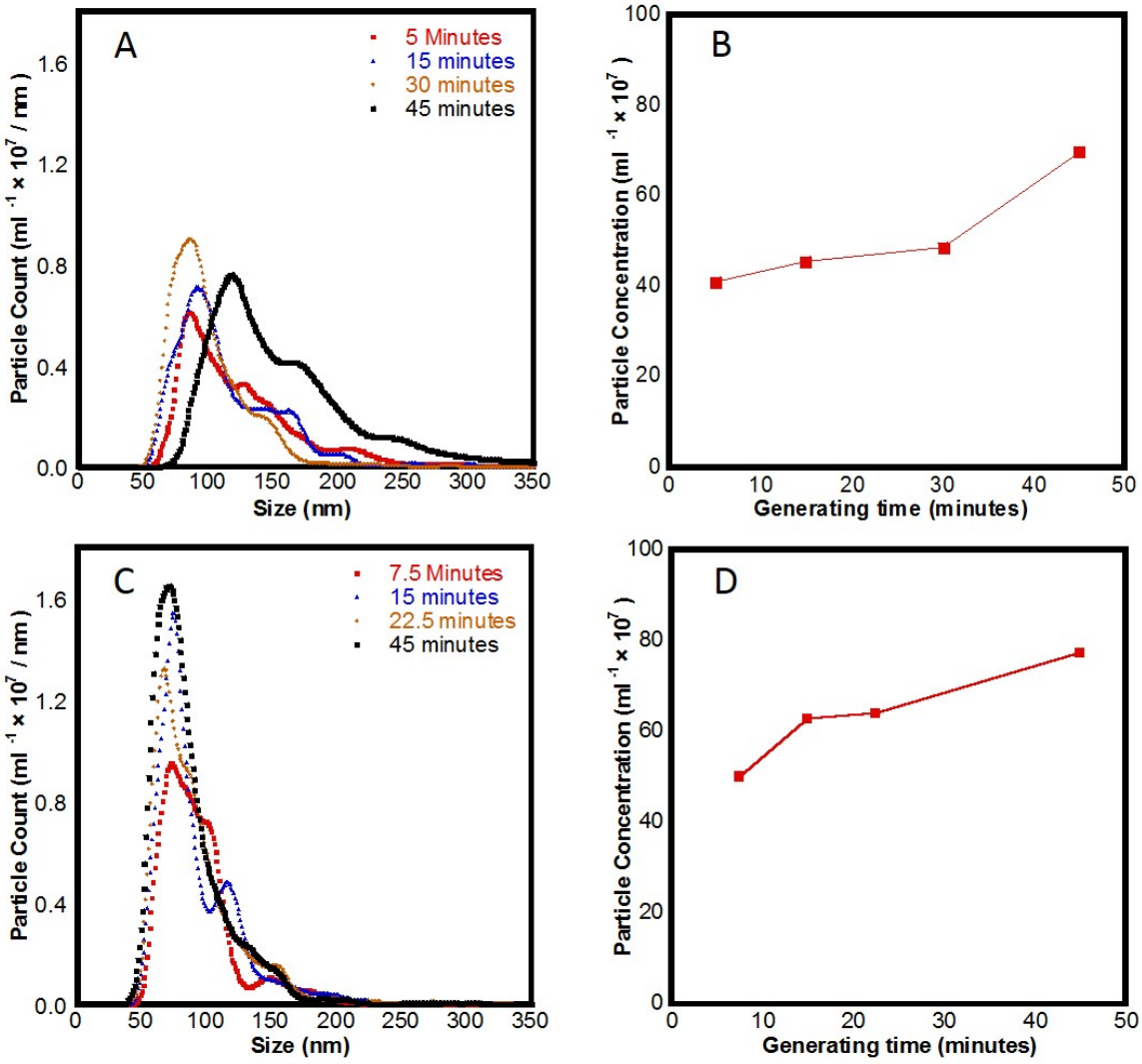

Figure 4-2. Influence of generating time on size and concentration of nanoparticles generated using the SSG (Panels A and B) and LSG (Panels C and D), measured using nanoparticle tracking analysis (NTA, Nanosight 300). The concentration of particles increased with increasing generation time in both samples. For Data DOI: 10.25911/5cd4cff51a5a5

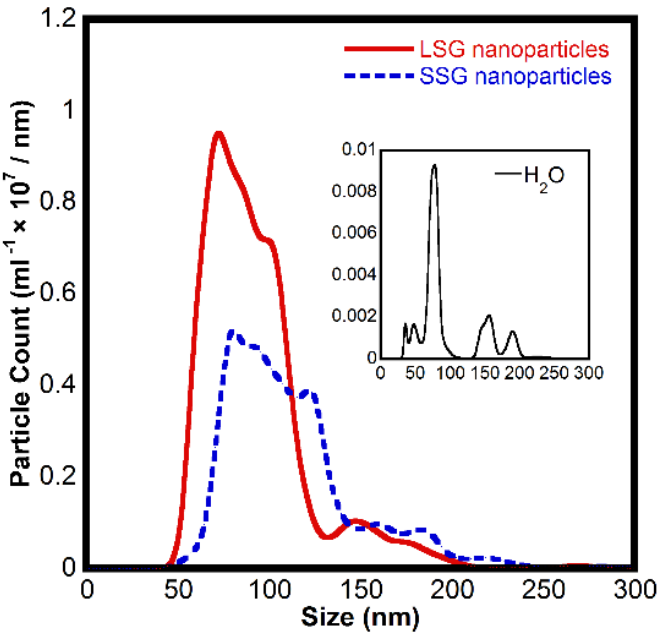

Figure 4-3. Histogram showing the particle size distribution using a bin width of 1 nm obtained using NTA (Nanosight NS300) for nanoparticles produced by the LSG generator (red line) and the SSG generator (dashed blue line) after filtering them through a 450 nm filter. The concentration of SSG nanoparticles was 348.0 ± 8.7 × 10^6 particles/ml. The concentration of LSG nanoparticles was 509.0 ± 10.2 × 10^6 particles/ml. The modal size was 98.7 ± 5.0 nm (SSG), and 73.5 ± 3.5 nm (LSG). This demonstrates that most of these particles were generated only after passing the water through the generators as the concentration of water (inset figure) was near the lower limit of the range of the apparatus. Note the axes titles for the inset figure are the same as the larger figure but the vertical scale is expanded 100 times. For Data DOI: 10.25911/5cd4d51053425

Given the expected instability of nanobubbles, it was important to determine the lifetime of any nanoparticles produced by the nanobubble generators. Note that the stability of nanoparticles or nanobubbles on the order of 15 minutes or less could not be investigated, because several minutes are required for the larger bubbles to leave the solution and the measurements themselves take several minutes or more to make. The long-term stability of the nanoparticles produced by the nanobubble generators was examined using light scattering. The size of the nanoparticles was tracked as a function of time and found to be stable for at least 7 hours as shown in panels A and B in Figure 4-4. The cuvette containing the solution of interest was placed inside the instrument and left undisturbed during these measurements. The formation of bubbles on the surface of the cuvette prevented measurements made in this manner proceeding over a longer period of time.

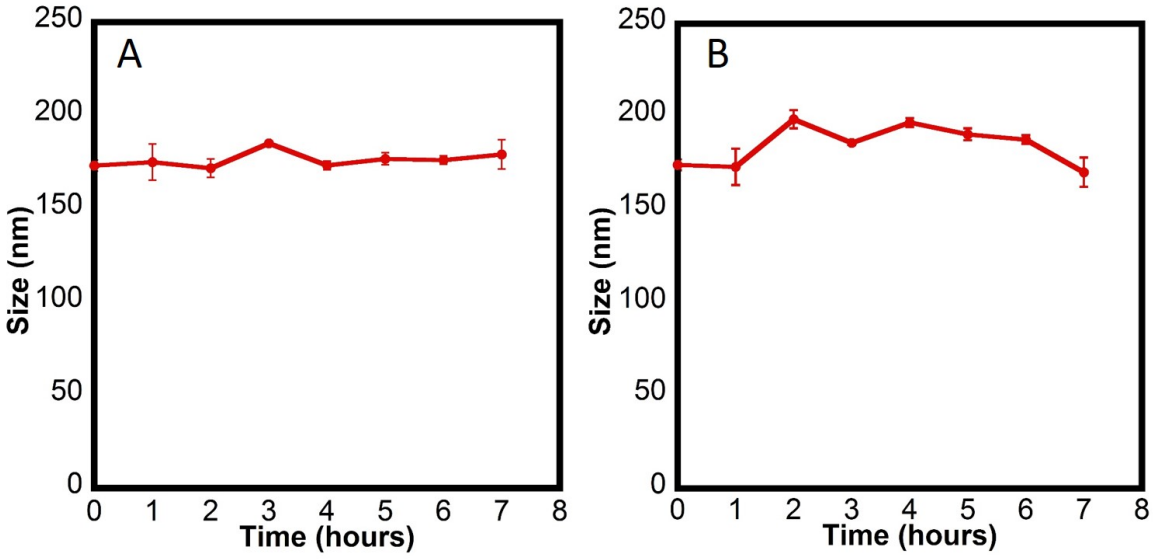

Figure 4-4. Average diameter of nanoparticles generated using SSG generator (panel A) and LSG generator (panel B) measured using light scattering over 7 hours. The error bars here represent the standard deviation for 10 measurements. For Data DOI: 10.25911/5cd4d75d0cbe1

To evaluate the stability of nanoparticles for longer periods NTA was used. A sample was generated at time zero and stored in a gas tight syringe. Aliquots of this sample were measured over a period of up to 9 days. As shown in panels A and B in Figure 4-5, the concentration of generated nanoparticles decreased slowly over time and the modal size increased slightly. The particles produced by the SSG generator were stable for approximately four days (see Figure 4-5A), while LSG nanoparticles were still present after 9 days (see Figure 4-5B).

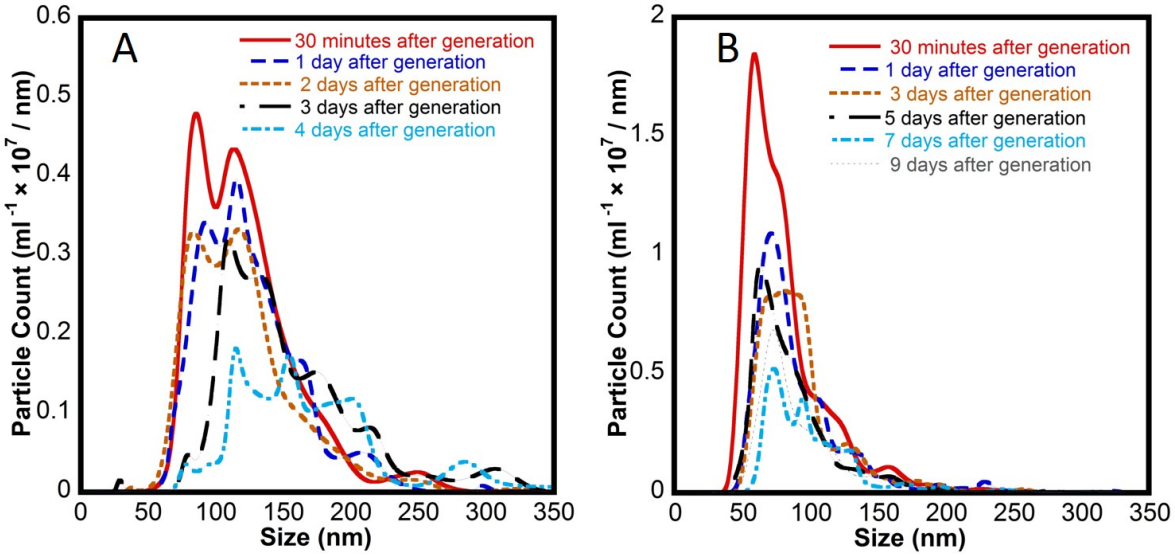

Figure 4-5. Histogram showing the particle concentration with a bin width of 1 nm measured using the Nanosight over 4 days for SSG nanoparticles and 9 days for LSG nanoparticles. For the LSG sample the concentration decreased significantly within 1 day, and then moderately until the ninth day (panel B). Note the concentration scale on these two figures is not the same. For Data DOI: 10.25911/5cd4d9ed2cb74

4.3.2 Measuring the density of nanoparticles

As nanoparticle tracking has the limitation of being unable to distinguish between nanoparticles that consist of solid, liquid or gas, a technique for differentiating nanobubbles from other nanoparticles was sought. The resonant mass measurement (RMM) technique employed by the Archimedes instrument can distinguish positively buoyant particles from negatively buoyant

particles, from the sign of the change in frequency that occurs when a nanoparticle passes through the sensor. The Archimedes was not able to detect a sufficient number of nanoparticles in the LSG sample due to their small size – that is most of the particles were too small to be detected. However, a significant number of nanoparticles that were less dense than water was observed in SSG samples. Therefore, RMM measurements in this study were only applied to SSG nanoparticles. The Archimedes revealed a population of buoyant nanoparticles with a concentration of 4.0×10^6 particles/ml (see Figure 4-6) and negatively buoyant nanoparticles with a concentration of 4.6×10^5 particles/ml. The mean buoyant mass for the detected buoyant particles was ~1.9 fg. These results show that the observed particles are indeed less dense than water as would be expected for a gas, but light oils also have a density less than water and therefore this is not definitive evidence that the nanoparticles being measured are nanobubbles. An accurate measure of the density would enable nanodroplets of light oils and indeed solid nanoparticles to be differentiated from nanobubbles.

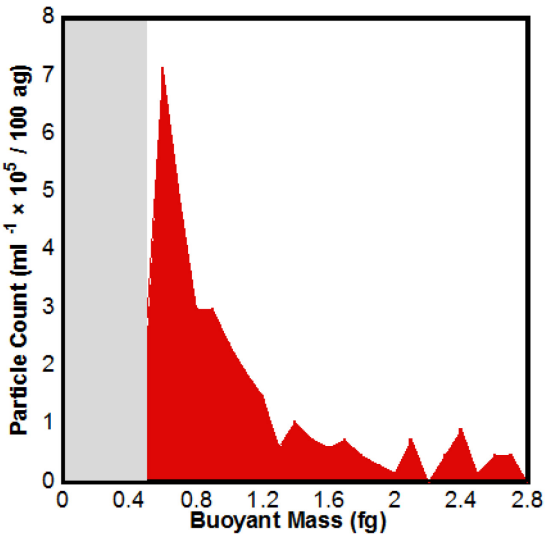

Figure 4-6. Representative buoyant mass histogram measured using the resonant mass measurement method for positively buoyant particles in the SSG sample with water as the solvent. Buoyant particles with a buoyant mass less than 0.45 fg were not able to be detected due to the limit of sensitivity of the instrument. This is indicated by the shaded grey region. For Data DOI: 10.25911/5cd5122333956

In the previous chapter, the RMM was used to determine the density of nanoparticles[158,162,178] (see §3.4.4). Here, the buoyant mass distribution is around the sensitivity limit (Figure 4-6). Therefore, the particle density was determined using the adapted iterative approach[162] (discussed in §3.4.4) in which a subset of the histogram was selected based on the estimate of the particle density and the known fluid density. This subset was used to determine the mean buoyant mass in each solvent, which was used to calculate an improved estimate of the particle density, until the estimate and resulting particle density agreed.

Application of the RMM technique as described in §3.4.4 yields the mean density of a nanoparticle dispersion. If the dispersion consists of nanoparticles of different materials with overlapping sizes the technique will give the population weighted mean density. Therefore measurement on a mixture of buoyant and non-buoyant particles requires that the positively buoyant particles are treated separately. This is straightforward using the Archimedes software.

The mean buoyant mass of SSG nanoparticles was measured in five different solutions with different ratios of H_2O and D_2O to produce solvents of different density. For each measurement, the particle concentration range was between 5×10^6 and 1×10^7 particles/ml. A straight line was fit to the data plotted as the buoyant mass versus the fluid density and the density of the particles was obtained from the x-intercept. The mean particle density was determined to be 0.95 ± 0.07 g/cm^3, (see Figure 4-7). The reported error corresponds to the 95 % confidence level (The method for determining the error is provided in Appendix, §A.3). The measured density is too high for the nanoparticles to consist of gas, indicating that the nanoparticles generated using the SSG technique are not nanobubbles.

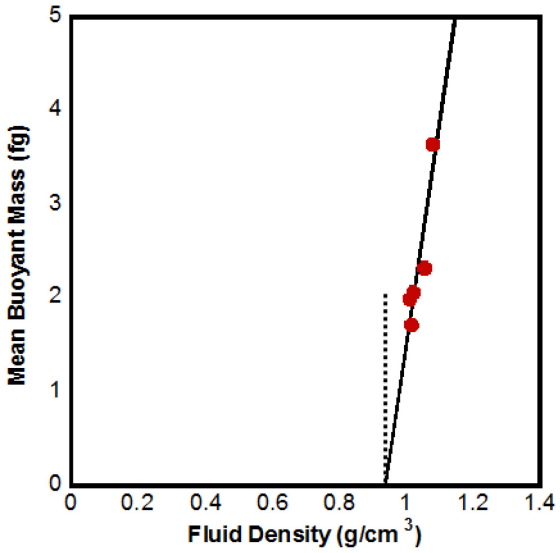

Figure 4-7. The mean density of SSG nanoparticles was determined from the x-intercept using regression analysis. Here the density of the particle is equivalent to the density of the solvent when the buoyant mass of a particle is zero. The density of SSG nanoparticles was determined to be 0.95 ± 0.07 g/cm^3. The stated error was calculated using the 95% confidence interval. The method for determining the error is provided in Appendix, §A.3. For Data DOI: 10.25911/5cd514fd9092d

The measurement of mean particle diameter by the resonant mass method can be determined from equations 2.6 – 2.8 in §2.3. In addition, fitting a line that passes through the experimental measurements of buoyant masses in solutions of at least two different densities enables the mean diameter to be determined from the slope of the linear regression[159], as shown in Figure 3-11. Here, the size measurements of the SSG nanoparticles, determined using these two methods, were compared and found to be in agreement. The measured mean diameter of the SSG nanoparticles using the determined density of 0.95 ± 0.07 g/cm^3 was 347 ± 93 nm, which was in agreement with the diameter that was obtained from the slope of the linear regression in Figure 4-7 (355 ± 119 nm).

For the SSG particles the size of the particles obtained from the Archimedes, (347 ± 93 nm), is very much larger than the size obtained from light scattering (i.e., 173 nm, see Figure 4-4) and NTA (i.e., 98.7 nm, see Figure 4-3). This is due to the sensitivity limit of the Archimedes, which

results in only the largest particles in the distribution being measured. This is supported by a comparison of the measured concentration of the SSG dispersion which was 348 × 10^6 particles/ml using NTA and 4 × 10^6 particles/ml using the Archimedes. The lower concentration measured in the Archimedes is due to only the largest fraction of particles being detected.

4.3.3 The influence of external pressure on nanoparticle size

The smaller LSG nanoparticles cannot be evaluated using this approach, as their size is below the sensitivity limit of the RMM. Another approach to differentiate nanobubbles from liquid or solid nanoparticles makes use of the large difference in compressibility between a gas and a condensed phase. As the compressibility of a gas is very different to the compressibility of liquids and solids, the response of a dispersion of nanoparticles to applied pressure may potentially be used to differentiate between nanobubbles and nanoparticles consisting of solids or liquids (details of this method were reported in §3.4.1). If light scattering is used to size the particles, the technique can be applied to particles substantially smaller than those measurable using the RMM.

The effect of varying the external pressure on the radius of a nanobubble can be obtained by solving equations 3.1 and 3.2 in §3.4.1. These equations were used to calculate the effect of external pressure on the radius of a nanobubble as a function of pressure. As stated in Chapter 3, the number of moles of gas within a bubble, *n*, is calculated under an external pressure of 1 atmosphere and assumed to be unchanged with external pressure. The effect of external pressure on bubble radius requires an iterative calculation as the bubble radius impacts the Laplace pressure. The results are shown in Figure 4-8, for bubbles of different sizes and for two values of the surface tension. Noting here the surface tension refers to the nanobubble-solution interface. The surface tension matters as it influences the Laplace pressure and therefore the magnitude of the effect of any external pressure on the change in bubble size. Generally, the

larger the bubble and the lower the surface tension the lower the Laplace pressure and the greater the effect of external pressure on bubble size.

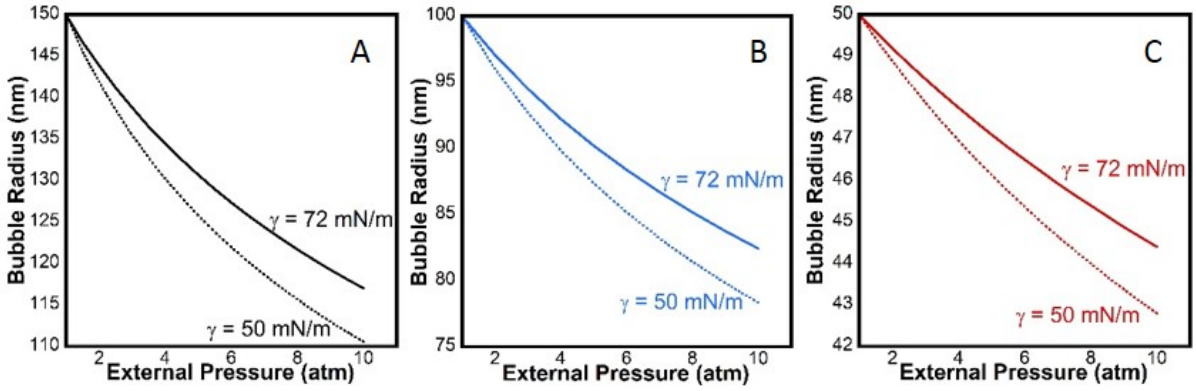

Figure 4-8. The calculated effect of external pressure (using equations 3.1 & 3.2) on the radius of a nanobubble with initial size 150 nm (Panel A), 100 nm (Panel B), and 50 nm (Panel C) as a function of external pressure, for nanobubble-solution interfacial tensions of γ = 72.0 mN m-1, (which is equivalent to the surface tension of pure water at 25˚C) and 50 mN m-1, (which corresponds to a moderately contaminated interface). Note that a reduction in surface tension that might accompany the adsorption of contaminants to the surface of a nanobubble leads to a greater reduction in nanobubble size at any given external pressure. For Data DOI: 10.25911/5cd515a919cb2

The effect of applying an external pressure to commercial nanobubble samples has been investigated by Tuziuti *et al.*[185]. A commercial nanobubble generator was used to generate nanoparticles with mean size around 55 nm and total concentration of 7.8×10^9 particles/ml. They reported a reduction in concentration and an increase in size after the sample had been exposed to an external pressure. However, this study differs from this study, as the size measurements of Tuziuti *et al.* were performed before and after application of an external pressure and not while the pressure was applied. That is, all measurements of Tuziuti *et al.* were taken at normal atmospheric pressure. Therefore, they did not measure the direct effect of external pressure on bubble size, as is the case here. The work presented here is akin to the earlier work by Johnson and Cooke[108] that showed that microbubbles produced by shear in

seawater contracted when the pressure was raised by about 0.8 atm above atmospheric pressure and expanded when put under negative pressure.

The effect of pressure using shock waves and ultrasound on surface nanobubbles has been studied by different groups [186,187]. Borkent *et al.* [186] applied shock waves to surface nanobubbles imaged by Atomic Force Microscopy in water. They observed that surface nanobubbles remained present after the passage of a shock wave with a large tensile stress down to approximately -6 MPa. However, the observed objects in this study are suspected to be nanodroplets because a plastic syringe with disposable needle was used in this work which was reported later as a source of PDMS contamination[188]. Zhang *et al.*[189] subjected surface nanobubbles to reduced pressures and later imaged the surface to reveal regions clear of surface nanobubbles. It was not possible in these studies to measure the surface nanobubbles during the application of pressure.

In order to study the response of nanoparticles to external pressure, SSG and LSG nanoparticles were measured at normal atmospheric pressure, and then the samples were pressurized to 10 atm and measured again, before the sample was depressurized to atmospheric pressure and measured a third time. The data obtained is summarized in Table 4-1 and compared to the calculated size change expected for a nanobubble with an interfacial tension of 72.0 x 10^{-3} $N\,m^{-1}$. It is worth noting that 72.0 x 10^{-3} $N\,m^{-1}$ is the surface tension of a pristine air-water interface and therefore is the maximum surface tension that any nanobubble-water interface would be expected to have. Contaminants adsorbing to the interface would lower the surface tension. As a lower interfacial tension leads to a greater expected change in size for a nanobubble, the calculated values are the *minimum* change in size that is expected for nanobubbles exposed to an external pressure. For both the LSG and SSG samples, the effect of pressure was negligible and far less than the size change expected for nanobubbles. This finding demonstrates that these particles are not gaseous, but rather consist of a solid or liquid that is relatively incompressible.

Table 4-1. Comparison of the experimentally measured and calculated effect of pressure on the diameter, *d*, of nanoparticles generated using the SSG and LSG generators. The error bars here represent the standard deviation for 10 measurements obtained by DLS.

Generator	$d_{(1\ atm,\ initial)}$	$d_{(10\ atm)}$	$\Delta d_{(10\ atm-1\ atm)}$	$\Delta d^{\ Expected}_{(10\ atm-1\ atm)}$[a]	$d_{(1\ atm,\ final)}$
SSG	188 ± 9 nm	197 ± 9 nm	9 ± 9 nm	- 32 nm	192 ± 8.6 nm
LSG	182 ± 6 nm	195 ± 7 nm	13 ± 7 nm	- 30 nm	189.6 ± 3.3 nm

[a] Minimum change in diameter calculated using a nanobubble interfacial tension of 72.0 x 10^{-3} $N\ m^{-1}$.

4.3.4 Implications

Both nanoparticle density measurements and the influence of external pressure on the measured size of the nanoparticles generated by the SSG and LSG indicate that the nanoparticles measured are not nanobubbles, but rather are other nanoparticles that form during the generation process. It is interesting that the generation process leads to the production of nanoparticles. Samples merely passed through the devices when inactive do not appear to produce nanoparticles, so the nanoparticle formation is likely to be associated with the formation of bubbles. One possible explanation is that bubbles formed during generation attract contaminants to their interface. Complete dissolution of such bubbles could lead to the formation of nanoparticles consisting of the accumulated material from the interface. This material may be slow to re-dissolve. The low concentration of nanoparticles produced means this is possible even in purified water, though here the surface tension data indicates the generators do contribute some level of contamination, so the surface-active material may be introduced during the generation process. It is expected that it will vary depending on the water source and the generator used. Due to their low concentration, an attempt to identify the

chemical makeup of these nanoparticles was not conducted. Enquiries indicated that Mass Spectrometry with an appropriate pre-concentrating step may be useful for determining the nature of the contaminants.

4.4 Summary

Two devices designed for generating nanobubbles on a small scale, SSG, and a large scale, LSG, were found to produce long-lived nanoparticles. The resonant mass measurement technique showed that the nanoparticles produced by SSG are positively buoyant and therefore less dense than water. However, extrapolating the mean buoyant mass as function of solvent density yielded a density for the nanoparticles of 0.95 ± 0.07 g/cm^3 at the 95% confidence level, which is inconsistent with the nanoparticles being gas-filled. Nanoparticles generated using SSG and LSG, showed no significant change in size when the external pressure was increased to 10 atm, which is also inconsistent with the nanoparticles being nanobubbles. Thus it is concluded that whilst these generators produce long-lived nanoparticles, these nanoparticles are not nanobubbles. Several other methods are reported to produce stable long-lived nanobubbles in bulk, without providing direct evidence that the nanoparticles being measured are indeed nanobubbles, in the following chapters, other reported methods for producing nanobubbles are tested to determine if nanobubbles were actually produced.

Chapter 5 Investigating the Existence of Long Lived Bulk Nanobubbles in Ethanol-Water Mixtures

This chapter is reproduced with minor changes from:

M. Alheshibri, V.S.J. Craig, Generation of nanoparticles upon mixing ethanol and water; Nanobubbles or Not?, J. Colloid Interface Sci. 542 (2019) 136–143. doi:10.1016/J.JCIS.2019.01.134.

5.1 Introduction

The mixing of ethanol and water has been widely reported as a convenient method for producing nanobubbles in bulk [44,98–100] and on surfaces [94], though in this study, the focus is only on bulk nanobubbles. During the mixing of ethanol and water, oversaturation is created as gas is more soluble in the components than in the mixture. That is, at equilibrium the combined amount of dissolved gas in any particular volumes of ethanol and water is greater than the equilibrium amount of dissolved gas when those same volumes of ethanol and water are combined. Thus mixing of solvents equilibrated with atmospheric gases (primarily N_2 and O_2) leads to supersaturation of dissolved gases in the mixture, leading to possible nucleation of bulk nanobubbles [95,98].

The debate as to whether bulk nanoparticles that are formed upon mixing ethanol and water are nanobubbles or other nanoparticles has persisted for more than a decade. In 2007 Jin *et al*.[44] used dynamic laser light scattering to examine solutions formed from mixing ethanol and water. They observed a slow mode of relaxation corresponding to submicron objects ~ 100 nm in diameter. The slow mode was shown to be removed only after repeated filtration and was regenerated by injecting filtered air. They argued the slow mode was due to bulk nanobubbles that were stabilized by organic molecules adsorbed at the gas-water interface. However, in a later study, it was reported that the intensity of light scattering was similar when gassed or degassed solvents were mixed, and it was concluded that these objects were not nanobubbles but contaminants [41]. In contrast, it has recently been reported that submicron particles generated upon mixing ethanol and water were nanobubbles [98] or nanobubble like clusters [99,100]. Qiu *et al*. [98] applied nanoparticle tracking analysis to nanoparticles generated by mixing ethanol and water. They studied the influence of the ethanol to water ratio on the concentration and the size of the nanoparticles. They found that the concentration of particles formed was a maximum at 8.3 % v/v ethanol. Contrary to the works by Habich *et al.* [41], they ascribed the scattering signal to the presence of bulk nanobubbles, because the concentration was five times less when degassed-solvents were mixed. Thus the issue remains unresolved. A concern in applying degassing to differentiate nanobubbles from other nanoparticles is that if the nanoparticles consist of a volatile solvent they may also be removed by degassing, giving a false positive. Moreover, in the circumstance that bulk nanobubbles are accompanied by other non-volatile nanoparticles the removal of nanobubbles by degassing may be masked by the presence of the other nanoparticles, giving a false negative. Thus degassing is an indirect and inconclusive method for determining if a candidate nanoparticle dispersion contains nanobubbles and this is likely the reason for the discrepancies reported in the literature. More direct techniques are needed to definitively address the issue.

This chapter tests the hypothesis that that long lived bulk nanobubbles are produced upon mixing ethanol and water, using the techniques developed in chapter 3 that probe the density and the pressure response of the nanoparticles. Nanoparticles were generated spontaneously upon mixing high-purity ethanol and high- purity water. Details of the generation process and all the related characterization methods are described in §5.2. The remainder of this chapter focuses on the outcomes of this study and discusses the origins of the nanoparticle formation.

5.2 Materials and Methods

High purity water (Elga Purelab Chorus 2) was used in this study. D_2O (Aldrich, 99.9 atom % D) was filtered to remove particles and used without further purification. All solvents were filtered through syringe filters with 20 nm pores (0.02 μm Whatman Anotop 10; Al_2O_3 membrane). The filters themselves may initially act as a source of nanoparticles, therefore prior to use 10 mls of pure water was passed through each filter to remove any particles that may have initially been in the filter. All glassware was cleaned by soaking in 10% NaOH (AR Grade, Aldrich), followed by generous rinsing with purified water before use.

5.2.1 Spinning Band Distillation Unit

Due to concerns that a dispersion of nanoparticles may be formed from contaminants in the ethanol that are made insoluble upon the addition of water via the ouzo effect[190], special care was taken to purify the ethanol in this study. A spinning band distillation column (36-100 mini fractional distillation system, BR instrument, USA) was used to further purify the analytical reagent grade ethanol. An image of the apparatus is shown in Figure 5-1. The distillation unit operates with a spinning band made of Teflon to achieve efficiency of up to 200 theoretical

plates at atmospheric pressure in a column 90 cm in length and 8 mm in diameter. A round bottomed flask filled with pure ethanol was placed on a heating mantle and connected to the column with a clamp. The reflux ratio was set to 30 and the heating mantle output to 5% to maintain slow distillation of the ethanol. Once the ethanol began to boil, the column was left to equilibrate the liquid and vapor flows for 30 – 60 minutes. This fraction was discarded before ethanol was collected at a rate of ~ 5 mls per minute. The collected distilled ethanol was then stored either in a glass flask or a stainless steel pressure vessel.

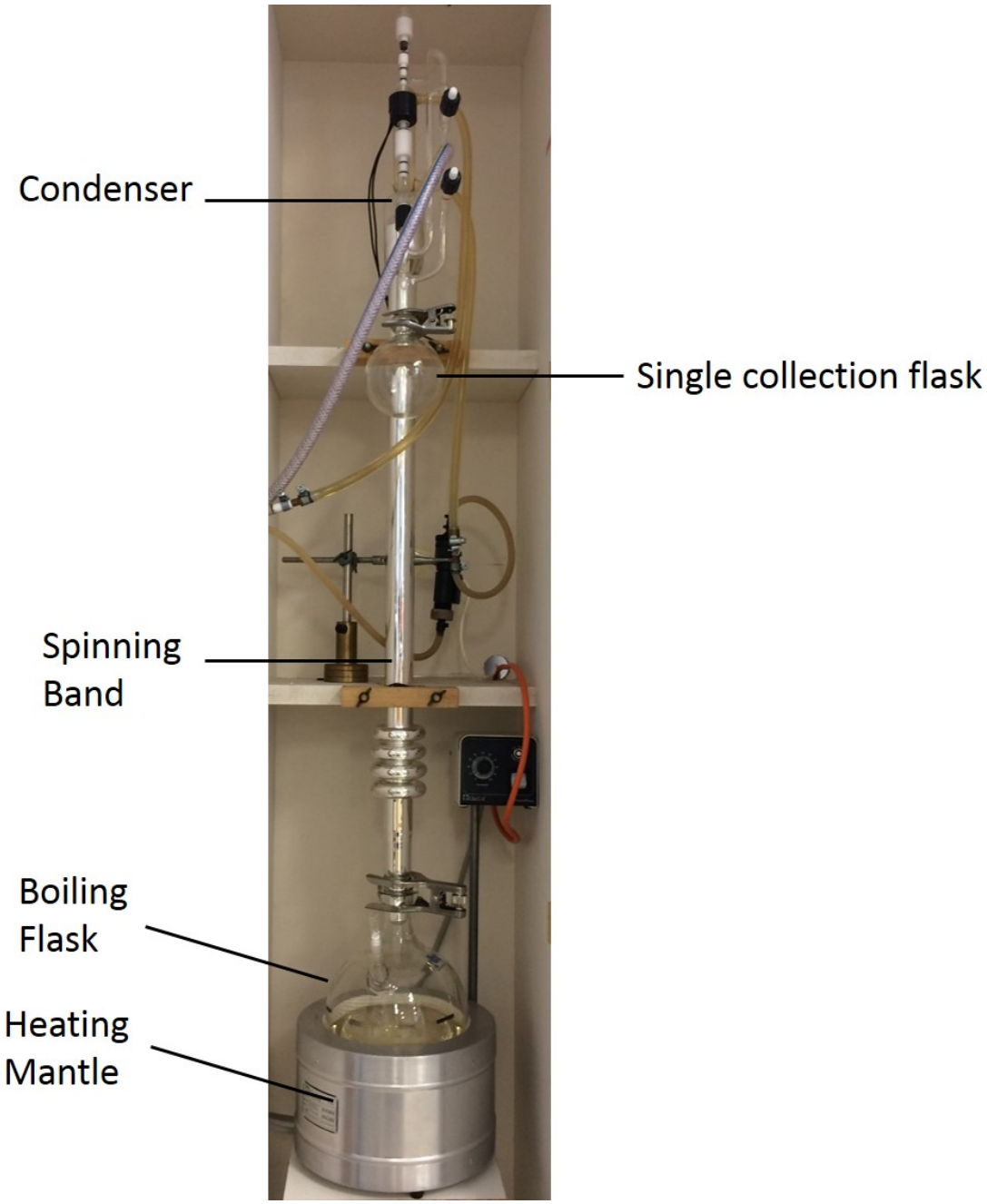

Figure 5-1. Photograph of the spinning band distillation unit installed in the cabinet with the doors open. The total unit is 153 cm in length.

5.2.2 Ethanol Water Mixing

Ethanol and high purity water were mixed to generate nanoparticles in this study. Ethanol and water were injected at the same time into a T shaped joint (nylon luer fitting, Cole–Parmer, Australia) using two separate syringes to produce a solution of ethanol and water. Each syringe

(1001 TLL, 1 ml Hamilton gastight glass syringe, Hamilton Co, USA) was connected to a syringe filter with a 20 nm pore size, such that the solvents passed through the filters immediately before mixing. Different ethanol concentrations were achieved by filling the syringes to an appropriate volume and operating the syringes at different speeds such that they emptied at the same time. This produced aqueous ethanol solutions, which invariably contained nanoparticles. This solution was immediately transferred to a sealed flask prior to characterization.

5.2.3 Dissolved oxygen measurement

Dissolved oxygen measurements were performed using a galvanic oxygen microsensor (AMT Analysenmes - Stechnik GmbH, Rostock, Germany) with a millisecond response time (for further details, see §4.2.1).

5.2.4 Degassing Experiments

Ethanol and Water were degassed in separate Schlenk flasks for a minimum of 4 hours using a vacuum pump (N840, 3FT. 18, KNF, US), and a liquid N_2 cold trap. The oxygen level in the water dropped from (8.4 mg/l at 25 °C), to (3.7 mg/l at 19 °C) after degassing. The level of dissolved nitrogen is expected to decrease by the same ratio suggesting an undersaturation of ~40%. The effects of degassing on the concentration of dissolved gases in ethanol was not measured because of material incompatibilities. It is assumed that a similar level of undersaturation was achieved.

5.2.5 Nanoparticle Tracking Analysis (NTA)

The size and the concentration of nanoparticles in aqueous ethanol solutions were determined using nanoparticle tracking analysis (NTA) with a NanoSight (NS300, Malvern, software version 3.1). Measurements were conducted at 25°C using a blue laser light source (70 mW, λ = 405 nm). A video of the scattered light from nanoparticles in a flow field was recorded for 60 s, enabling several hundred particles to be tracked and measured. The sample was introduced using a syringe pump (flow rate set to 30 in arbitrary units). The average of five measurements, each captured over 60 s at 25 frames/s is reported. The parameters used were camera level = 13, threshold = 3, and gain = 366. The size that is derived from the particle diffusion coefficient depends on the viscosity of the solvent, as per the Stokes−Einstein equation (see equation 2.3 in §2.1). The viscosity of the aqueous ethanol solutions was calculated using a polynomial fitting reported for the measurements by Khattab *et al*.[191].

5.2.6 Resonant Mass Measurement (RMM)

The size and buoyant mass of nanoparticles in aqueous ethanol solutions were measured at room temperature by the resonant mass method (RMM) using an Archimedes (Malvern Instruments, UK, ParticleLab software (version 1.2). A polystyrene standard containing spheres 500 nm in diameter (Thermo Fisher Scientific) was used to calibrate Nanosensor chips. Data was acquired for 1 h or until 250 particles had been measured using a detection threshold of 0.009 Hz.

5.2.7 Dynamic light Scattering

A Zetasizer Nano ZS (Malvern) employing a 633-nm He-Ne laser at a scattering angle of 173°, was used to measure the size of particles in solution by dynamic light scattering. The measurements were made with automatic attenuation at a position of 4.65 mm from the cuvette wall and analyzed using the Malvern Zetasizer software version 7.1. For all measurements, 13 runs of 10 s were performed with at least 5 repetitions to obtain the particle size distribution.

5.3 Results and Discussion

5.3.1 Formation and stability of nanoparticles

The concentration of particles in mixtures of ethanol and water were measured using nanoparticle tracking analysis (NTA, Nanosight NS300, Malvern). High grade purified laboratory water and AR grade ethanol, that was further purified by slow spinning band distillation, was used in these experiments. The mixing of ethanol and water was found to produce significant numbers of nanoparticles up to 200 nm in size. The effect of ethanol concentration on the size and number of nanoparticles produced is shown in Figure 5-2. The highest concentration of nanobubbles was observed in a 20% v/v ethanol aqueous solution. The concentration of the particles increased from 36.2×10^7 particles/ml at 10% v/v ethanol to 99.6×10^7 particles/ml at 20% v/v ethanol. Increasing the concentration of ethanol led to a reduced number of particles as shown for 30% and 40% v/v ethanol solutions.

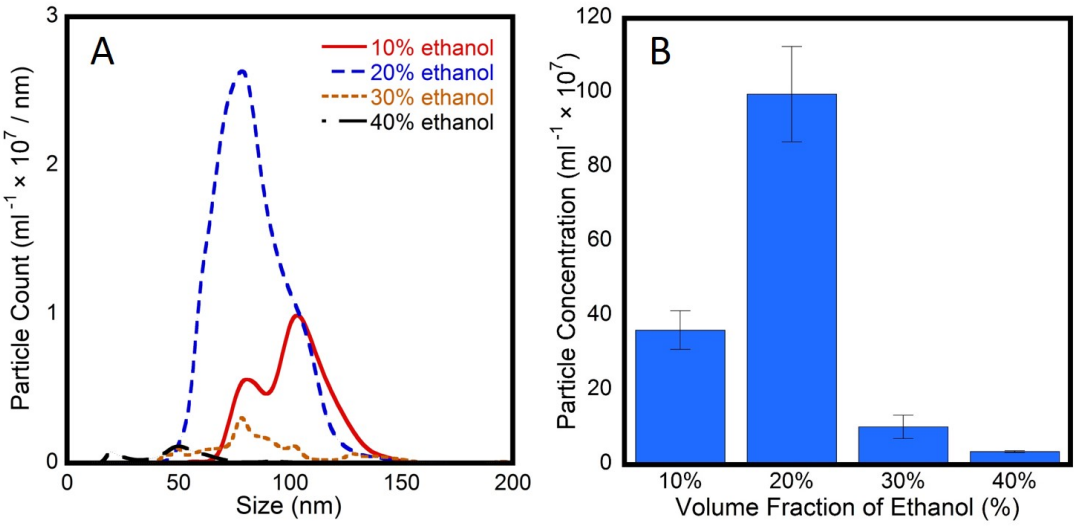

Figure 5-2. Size distribution (A) and total concentration (B) of nanoparticles produced upon mixing ethanol and water as a function of ethanol volume fraction measured using nanoparticle tracking. The error bars here represent the standard error for five measureme. For Data DOI: 10.25911/5c11b049a2c8c

In all subsequent measurements, the concentration was set to 20% v/v ethanol. The baseline levels of particles in each of the solvents after filtering (20 nm pore size syringe filters) and passing through the tubing and T section were also determined using the Nanosight. The concentration of particles in both ethanol and water were found to be near the lower limit of detection for the apparatus, being 0.69×10^7 and 0.65×10^7 particles/ml, respectively. This is more than two orders of magnitude lower than the concentration of nanoparticles found upon mixing ethanol and water to produce a solution of 20% v/v ethanol (see Figure 5-3), indicating that the nanoparticles measured are being produced during solvent mixing. The mean size of the nanoparticles shown in Figure 5-3 was 91.7 ± 0.5 nm, with a modal size of 85.2 ± 0.9 nm. The size of the nanoparticles produced from one batch to the next was found to vary (different size distributions are shown in Figure 5-4), likely due to slight variations in the mixing process which was not precisely controlled. However, the size was always in the range of 60–200 nm.

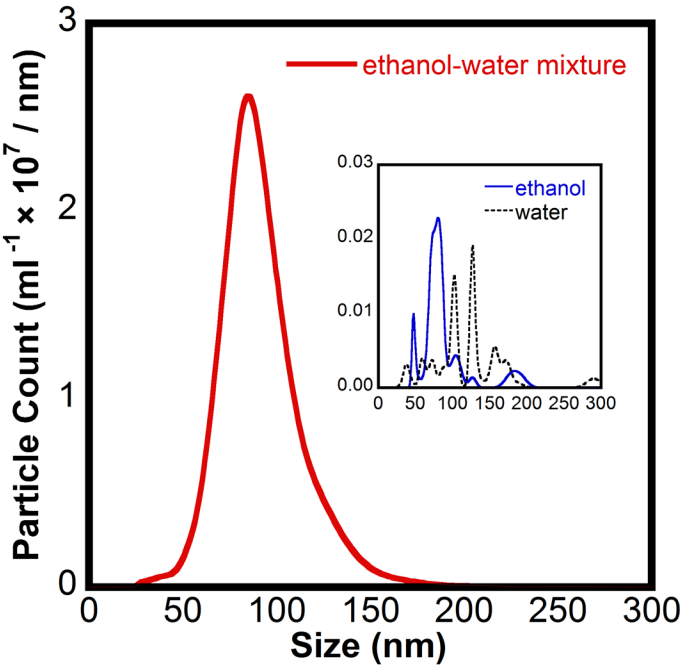

Figure 5-3. Particle size histogram with a bin width of 1 nm, obtained using NTA (Nanosight NS300) for nanoparticles produced by mixing ethanol and water to produce a 20% v/v ethanol solution (red line). The concentration of nanoparticles measured in the filtered pure solvents (measured separately) are shown in the inset. The concentration of nanoparticles in the pure solvent are near the lower limit of the range of the apparatus and are two orders of magnitude less than the concentration of nanoparticles measured after mixing. (Note: The axes labels for the inset figure are the same as those of the larger figure, but the vertical scale is expanded 100 times.) For Data DOI: 10.25911/5c11b0bb35a97

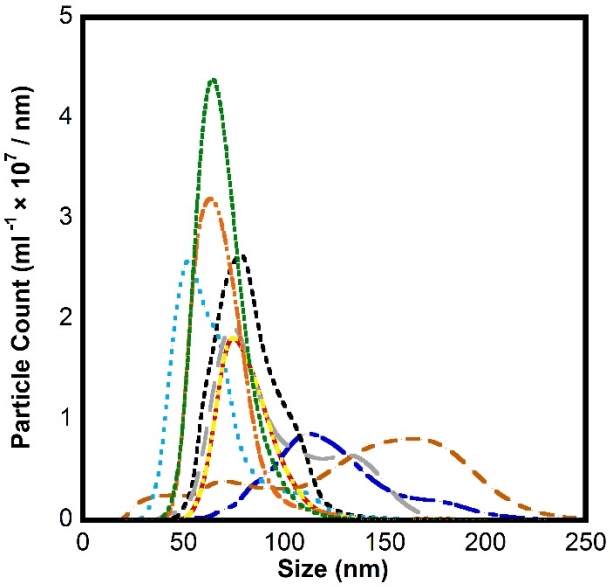

Figure 5-4. Histogram showing the variation in particle size distribution for nanoparticles produced by different trials of mixing ethanol and water to produce a 20% v/v ethanol solution. The ethanol-water mixture produced a narrow distribution of nanoparticles in most cases, and a broad distribution on a few occasions.

Given the anticipated very short lifetime of nanobubbles, the stability of the nanoparticles produced upon mixing ethanol and water was investigated. Nanoparticles were produced and stored in a gas-tight syringe. The syringe remained undisturbed during the lifetime of the study. Aliquots of this sample were measured at chosen times up to 96 hours after production. The modal size was maintained over the first 6 hours and then it increased gradually (see Figure 5-5). A longer study showed that the concentration decreased slowly with time and the size increased as shown in Figure 5-5. This indicates that the nanoparticles were stable for several hours after production but had grown and reduced in concentration substantially after 24 hours. These results confirm earlier reports that nanoparticles are produced upon mixing ethanol and water [41,44,98–100]. This is notable given the extra measures that were employed to purify the ethanol used in these experiments.

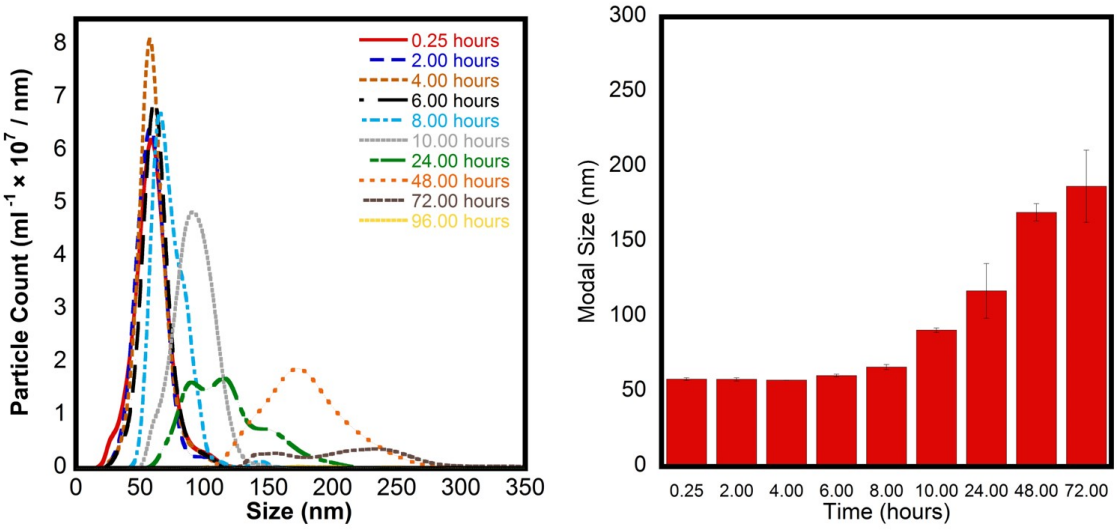

Figure 5-5. Size distribution (left panel), and modal size (right panel) versus time of nanoparticles produced upon mixing ethanol and water. The modal size for the nanoparticles after 96 hours is not shown because the concentration of the nanoparticles was very low (i.e. 5.9×10^7 particles/ml).

Due to the debate in the literature over the nature of the nanoparticles produced upon mixing ethanol and water, this study was designed to test whether the nanoparticles being produced are nanobubbles or non-gaseous nanoparticles. To do this, the density and compressibility of the nanoparticles were evaluated using the techniques that have been developed for this purpose (see chapter 3). The density can be determined by a series of resonant mass measurements in solvents of different density and the compressibility evaluated from the particle size as a function of pressure.

5.3.2 Nanoparticle Density

The particles generated by mixing ethanol and water were measured using the resonant mass measurement method (RMM). A population of positively buoyant nanoparticles at a concentration of 1.58×10^7 particles ml^{-1} (see Figure 5-6) was evident. Only positively buoyant particles were observed in the sample, with a mean buoyant mass of 0.76 ± 0.03 fg. This

indicates that the nanoparticles are less dense than the solvent and therefore unlikely to be solid nanoparticles. This however does not demonstrate that they are nanobubbles as they may be nanodroplets of a liquid that is less dense than water.

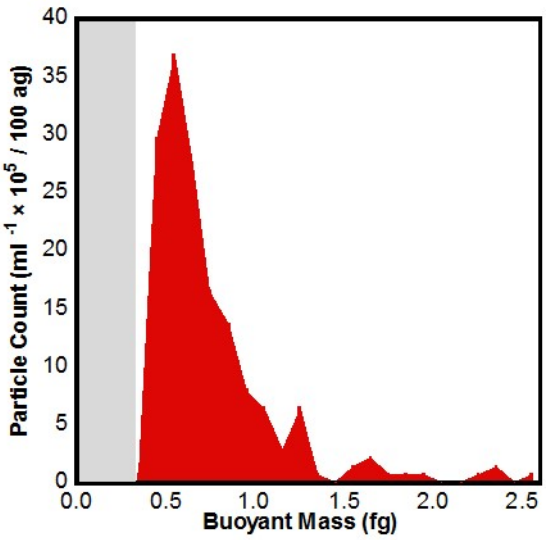

Figure 5-6: A representative buoyant mass histogram measured using RMM for nanoparticles generated upon mixing ethanol and water to produce an aqueous ethanol solution of 20% v/v ethanol. The concentration of particles was measured to be 1.58×10^7 particles/ml. Particles with a buoyant mass of < |0.4| fg are undetectable due to the instrument's limited sensitivity (shaded gray region). No negatively buoyant particles were detected. For Data DOI: 10.25911/5c11b178d13cc

The density of nanoparticles generated upon mixing ethanol and water to produce a 20% v/v aqueous ethanol solution were determined. Solutions of different densities were produced by varying the ratio of H_2O and D_2O used to dilute a single batch of nanoparticles (see Table 5-1). A single batch was used to ensure that the particle distribution was the same in each sample. The mean buoyant mass of the nanoparticles was measured in each medium. The particle density was determined by plotting the buoyant mass versus fluid density and extrapolating to the x-intercept to zero buoyant mass. A buoyant mass of zero occurs when the particle density is equivalent to the fluid density [158,159,162,192]. The mean particle density was found to be 0.91 ±

0.01 g/cm^3 (see Figure 5-7), with the error calculated based on a 95% confidence interval. The method for determining the error is provided in Appendix, §A.3. The measured density is inconsistent with the nanoparticles being nanobubbles, because the density is much higher than the expected density of gas bubbles.

Table 5-1. Densities of nanoparticle solutions produced by diluting a single batch of nanoparticles with different ratios of H_2O: D_2O.

Mass fraction used for dilution H_2O: D_2O	**Mass fraction of the diluted nanoparticle solution H_2O: D_2O: ethanol**	**Measured density of the nanoparticle solution [a] (g cm^{-3})**
1.00 : 0.00	0.93 : 0.00 : 0.07	0.977 ± 0.002
0.50 : 0.50	0.63 : 0.30 : 0.07	1.021 ± 0.002
0.33 : 0.67	0.53 : 0.40 : 0.07	1.036 ± 0.002
0.00 : 1.00	0.33 : 0.60 : 0.07	1.055 ± 0.002

[a] The density of the nanoparticle solution was measured using a digital densitometer (DMA 35, Anton Pear, Austria) at room temperature.

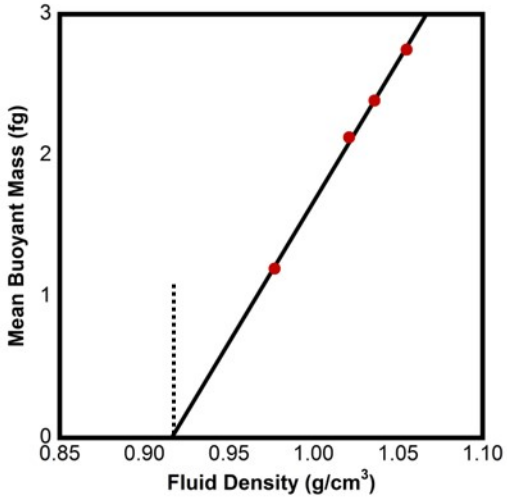

Figure 5-7: The mean density of nanoparticles produced by mixing ethanol and water to produce an aqueous solution of 20% v/v ethanol was obtained from the x-intercept. The density was determined to be 0.91 ± 0.01 g/cm^3 using regression analysis. The reported error represents the 95% confidence interval. The method for determining the error is provided in Appendix, §A.3. For Data DOI: 10.25911/5c11b1d50780b

5.3.3 Nanoparticle compressibility

A further test that can be applied to nanobubble candidates to assess the effect of pressure on the size of the nanoparticles. The Young–Laplace equation and the ideal gas law can be used to determine the effect of external pressure on nanobubbles (see equations 3.1 and 3.2 in §3.4.1).

The effect of external pressure on the size of a bubble is greater as the surface tension is reduced, due to the accompanying reduction in Laplace pressure. The calculated effect of external pressure on bubbles of different initial sizes at $\gamma = 42.0 \times 10^{-3}\ N\ m^{-1}$ is presented in Figure 5-8. This is the surface tension of 20% v/v aqueous ethanol[191]. As stated in Chapter 3, the number of moles of gas within a bubble, n, is calculated under an external pressure of 1 atmosphere and assumed to be unchanged with external pressure. The effect of external pressure on bubble radius requires an iterative calculation as the bubble radius impacts the Laplace pressure. Any

surface active contaminants will reduce the surface tension further, therefore the calculation reflects the minimum change in size that a nanobubble in 20% v/v aqueous ethanol should undergo with a change in pressure.

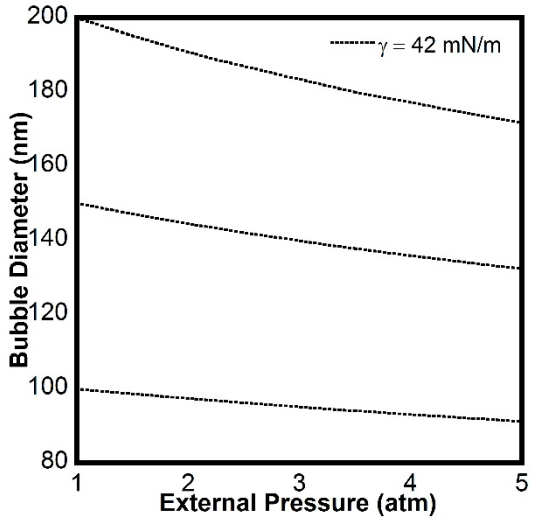

Figure 5-8. The diameter of bubbles with initial diameters of 200 nm, 150 nm, and 100 nm as a function of external pressure, for a nanobubble-solution interfacial tension[191] of γ = 42.0 x 10^{-3} $N\ m^{-1}$ (calculated using equations 3.1 and 3.2 in §3.4.1). For Data DOI: 10.25911/5c11b2280fe6a

The influence of external pressure on microbubbles [108,112], and nanobubbles has been investigated previously (see chapter 3). Due to the compressibility of gasses, bubbles expand when subjected to negative pressure and contract when the pressure is increased. It was shown in chapter 3 that the response of nanobubbles to pressure can be used to distinguish them from other nanoparticles, even when the nanobubbles are coated with insoluble material. In addition, the pressure response of nanobubbles was detected even in the presence of other solid nanoparticles in the same suspension. Thus, measurements of the change in size of candidate nanoparticles due to external pressure can be used to determine if they are nanobubbles.

In this study, the average diameter of nanoparticles in aqueous 20% v/v ethanol solutions were measured at 1 atmosphere of external pressure, then at 5 atm of external pressure and again at 1 atmosphere of external pressure. Table 5-2 shows the average diameter before, during, and after application of pressure. Using equations 3.1 and 3.2 in §3.4.1, where the surface tension for 20% v/v ethanol is[191] 42.0 x 10^{-3} $N\ m^{-1}$, the size at 5 atm should have decreased from 131 nm to 117.3 nm. The data is listed in Table 5-2 and compared to the expected size change for a nanobubbles with surface tension of 42.0 x 10^{-3} $N\ m^{-1}$. As shown, the change in size for nanoparticles generated by mixing water and ethanol was far less than the anticipated change for gas bubbles with the same initial size. These results show that the effect of pressure on the size of the particles is insignificant and indicates that these objects are not gas-filled bubbles. These findings are consistent with the density measurements, which confirm that these particles are impurities resulting from the mixing of water and ethanol rather than being nanobubbles.

Table 5-2. Comparison of the experimentally measured and expected effect of pressure on the average diameter, *d*, of nanoparticles generated upon mixing water and ethanol.

$d_{(1\ atm,\ initial)}$	$d_{(5\ atm)}$	$\Delta d_{(5\ atm-1\ atm)}$	$\Delta d^{Expected}_{(5\ atm-1\ atm)}$ [a]	$d_{(1\ atm,\ final)}$
131.0 ± 1.2 nm	132.0 ± 0.5 nm	1.0 ± 1.7 nm	-13.7 nm	130.0 ± 2.0 nm

[a] Minimum change in diameter calculated using a nanobubble interfacial tension of 42.0 x 10^{-3} $N\ m^{-1}$.

Having demonstrated that the mixing of ethanol and water results in the production of nanoparticles and that these nanoparticles are not nanobubbles, as their density and response to the application of pressure are inconsistent with the particles being nanobubbles, the question arises as to how the nanoparticles are formed and what they consist of. The origin of these particles might be considered an example of 'the ouzo effect'. The ouzo effect in the absence of surfactants or agitation, results in the formation of oil droplets of micron size and smaller in a ternary system comprising alcohol, water and oil [190]. Ethanol plays a significant role in the

ouzo effect as a co-solvent. This is due to the high solubility of oil in alcohol compared with water. Adding small amounts of oil to ethanol creates a homogeneous single phase, as the oil completely dissolves in ethanol. Adding water to this binary solution causes oil to supersaturate and then form into oil droplets because the solubility of the oil decreases rapidly with increasing water concentration. Vitale and Katz showed that droplets formed by the ouzo effect can be stable for up to several days, when the oil density was very near that of the continuous aqueous phase [190].

Are the nanoparticles formed in this study an example of the ouzo effect? Using the size distribution data in Figure 5-2 and assuming that all the material in the nanoparticles originated from the ethanol, the volume fraction of the nanoparticles was calculated to be $\approx 2.73 \times 10^{-5}$. That is if the nanoparticles represent an impurity sourced from the ethanol the limit of purity of the distilled ethanol used in this study was 99.997 % by volume. The small quantity of material in the nanoparticles exemplifies the challenge in identifying their composition. The very low volume fraction of material in the nanoparticles suggests that they are not within the appropriate region of the phase diagram to ascribe the production of nanobubbles here to the Ouzo effect. It is of course possible that the material within the nanoparticles represents only a small fraction of the oil within the ethanol, but this is not likely. Further nanoparticles were produced at all volume fractions of ethanol studied (10 %, 20 %, 30 % and 40 %), a range that would appear to be too large to be attributed to the ouzo effect.

If the formation of nanoparticles is not due to homogenous nucleation as in the ouzo effect, perhaps it can be attributed to heterogenous formation. The supersaturation of dissolved gases that accompanies mixing of ethanol and water could lead to the nucleation of bubbles during mixing, which subsequently shrink and dissolve. The bubble solution interface will attract contaminant material. During dissolution of the bubble, the contaminant material will be

concentrated, and this could lead to the formation of a nanoparticle when the bubble completely dissolves. To test this model, the experiments were repeated using ethanol and water with depleted concentrations of dissolved gas in order to reduce or prevent supersaturation upon mixing (see Figure 5-9). As shown, the total concentration of nanoparticles decreased significantly upon mixing degassed ethanol and degassed water. The result is consistent with the findings of previous studies[98,100]. The decrease in nanoparticles could be indicative of a decrease in the formation of bubbles due to a reduction in the dissolved gas concentration in solution. An alternative explanation is that degassing reduced the concentration of the material making up the nanoparticles directly. This is unlikely to happen given the density of the nanoparticles and the steps taken to purify the ethanol. To test this hypothesis, the solvents were re-gassed separately by shaking them vigorously for several minutes and waiting for 24 hours for the solvents to recover the air-equilibrated saturation level. The solvents were stored in a sealed vessel with a volume of air well in excess of the volume of liquid during equilibration. As shown in Figure 5-9, mixing the re-gassed solvents produce nanoparticles with a concentration slightly above the initial concentration obtained on mixing the gassed solvents. This suggests that the supersaturation of the dissolved gas is associated with the formation of the nanoparticles and is also strong evidence that the nanoparticles are not reduced upon degassing due to the removal of volatile oils.

With regards to the ouzo effect, removing the dissolved gasses prior to mixing was reported to enhance the formation of spontaneous emulsification[193]. Sowa *et al*. evaluated the impact of degassing on oil droplets formed by the ouzo effect for ternary systems of ethanol, water and different volatile hydrocarbons [193]. The concentration of oil droplets was found to be greater when they mixed degassed samples compared with non-degassed samples. This finding contradicts the results shown in Figure 5-9, where a lower number of particles were detected after mixing degassed solvents. This provide further reasons to discount the possibility that the

ouzo effect leads to the formation of the nanoparticles observed. Rather their origin is ascribed to adsorption of contaminants to the interface of bubbles, that upon dissolution leave behind the material accumulated at the interface in the form of a nanoparticle. A simple calculation reveals that bubbles larger than 1 micron in size with a sub monolayer coverage of contamination can easily accumulate enough material to form a 100 nm particle. It is worth noting that the maximum concentration of nanoparticles was obtained at 20 %v/v of ethanol here (0.93 mole fraction of water) which is consistent with Millare *et al*.[100] but at odds with the Jun Hu group [98] who reported the maximum concentration of nanoparticles at 8.3 %v/v of ethanol. The difference is likely due to differences in the type of contamination. The maximum gas supersaturation of the mixture occurs at 0.84 mole fraction of water[95]. Thus the maximum number of bubbles would be expected at 0.84 mole fraction of water. However, if the contaminants making up the nanoparticles are highly soluble in ethanol and poorly soluble in water the maximum yield of nanoparticles would be expected to be at a water mole fraction > 0.84 and dependent on the particular nature and concentration of the contaminants present. This is consistent with the results obtained here, where the production of nanoparticles is a maximum at 20 %v/v ethanol and decreases at higher ethanol concentrations.

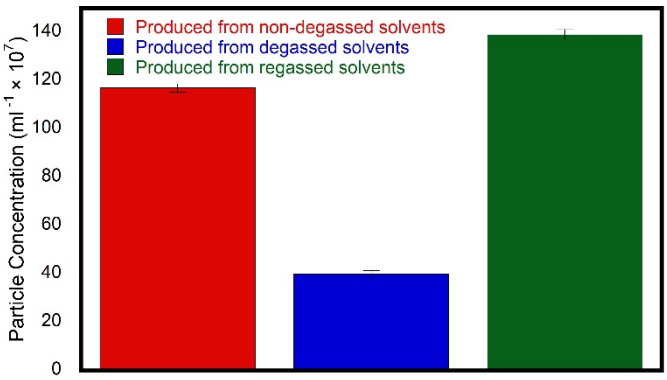

Figure 5-9. Comparison of the concentration of nanoparticles produced upon mixing (1) ethanol and water (red column), (2) mixing degassed ethanol and degassed water (blue

column), and (3) mixing ethanol and water that had been degassed and then allowed to re-gas (green column). The error bars here represent the standard error for five measurements obtained by the nanoparticle tracking analysis software. For Data DOI: 10.25911/5c11b2688d786

5.4 Summary

Mixing ethanol and water was found to produce long lived nanoparticles of the order of 100 nm in diameter, whose population reached a maximum at 20 %v/v ethanol, although an elaborate distillation system was used in this study to purify the ethanol. It is concluded that the nanoparticles produced were not bulk nanobubbles, based on two direct observations. First, the resonant mass measurement showed that all the particles were positively buoyant, but with a mean density of 0.91 ± 0.01 g/cm^3. Second, dynamic light scattering showed no significant change in the average diameter when pressure was applied. Similar to previous reports[98,100], the Nanosight showed a significant reduction in particle concentration upon mixing degassed ethanol and degassed water, suggesting that the formation of nanoparticles was directly associated with the supersaturation of dissolved gas. The findings from this study resolve the debate as to the nature of the nanoparticles produced when ethanol and water are mixed – they are not nanobubbles.

Chapter 6 Investigating the Possible Production of Long Lived Bulk Nanobubbles due to Supersaturation by a Gas Evolving Chemical Reaction

This chapter is reproduced with minor changes from:

M. Alheshibri, M. Jehannin, V. Coleman, V.S.J. Craig, Does Gas Supersaturation by a Chemical Reaction Produce Bulk Nanobubbles?, J. Colloid Interface Sci. 554 (2019) 388–395. doi: 10.1016/j.jcis.2019.07.016

6.1 Introduction

Several studies have indicated that nanobubbles can be generated using gas evolving chemical reactions[103,194–196].The White group[194–196] in a series of publications examined the electrochemical nucleation of nanobubbles on solid nanoelectrode surfaces. Nanobubbles were generated using the reduction of protons in acidic solutions[194], the oxidation of N_2H_4[195] and the decomposition of H_2O_2[196] to produce the gaseous products, hydrogen, nitrogen, and oxygen respectively. They reported that in their experiments, supersaturation levels of 310, 160 and 130 were required for the formation of hydrogen nanobubbles, nitrogen nanobubbles, and oxygen nanobubbles respectively. Gas evolving chemical reactions have also been reported as a method for producing bulk nanobubbles. For instance, Li *et al.*[103] used the chemical reaction

between ammonium chloride and sodium nitrite to produce nitrogen nanobubbles in bulk. They used cryo-electron microscopy to directly image nanoparticles trapped in amorphous ice generated by the chemical reaction. They found these nanoparticles formed only when they were trapped between two carbon films and concluded that these are bulk nanobubbles with diameters of 200–300 nm. The rate of nanoparticle generation was adjusted by changing the concentration of HCl in the solution. This technique is widely used and it is accepted that the rapid freezing process does not produce artefacts of this kind. However, it is important to investigate the generation of these nanoparticles in aqueous solution, to more rigorously examine the nature of the nanoparticles.

The experiments described in this chapter were performed first to see if nanoparticles are produced upon supersaturation of gas by a chemical reaction between aqueous solutions of ammonium chloride and sodium nitrite, and If nanoparticles are produced, established protocols in chapter 3 can be used to test these nanoparticles, to determine if they are nanobubbles.

6.2 Materials and Methods

6.2.1 Reagents

High grade purified water (ELGA Purelab Chorus 2) was used in this study. Sodium nitrite ($NaNO_2$) was purchased from Sigma-Aldrich (Reagent plus grade ≥ 99.0%), and ammonium chloride (NH_4Cl) was purchased from Ajax Finechem (AR grade 99.5%). Both were used without further purification. The NH_4Cl was reported to have impurities, as detailed in Table 6-1. Information on the impurities present in the $NaNO_2$ was not provided by the supplier. Glassware was cleaned with 10% NaOH for 10 minutes, before extensive rinsing with purified water. Aqueous solutions of $NaNO_2$ and NH_4Cl of different concentrations were prepared with

high purity water and filtered through a 20 nm syringe filter (0.02 μm Whatman Anotop 10 inorganic with an Al_2O_3 membrane) before use, in order to remove particles. As the syringe filters may on first use yield nanoparticles or contaminants, the syringe filters were pre-rinsed with 10 ml of pure water before use. HCl and NaOH (AR grade, Aldrich) were used to adjust the pH of the solution. In a typical experiment, 5 mls of an aqueous NH_4Cl solution (0.1−1 M) were added to a vial of 5 ml of an aqueous $NaNO_2$ solution at the same concentration. The vial was then sealed and shaken vigorously by hand for 30 − 60 seconds. This was taken as the time of mixing.

Table 6-1. Impurities present in NH_4Cl.

Impurity	**Percentage***	**Impurity**	**Percentage***
Potassium (K)	0.0050%	**Iron (Fe)**	0.0001%
Sodium (Na)	0.0050%	**Copper (Cu)**	0.0001%
Residue after ignition	0.0100%	**Phosphate (PO4)**	0.0002%
Calcium (Ca)	0.0010%	**Lead (Pb)**	0.0002%
Arsenic (As)	0.0003%	**Magnesium (Mg)**	0.0002%
Heavy metals	0.0005%	**Sulphate (SO_4)**	0.0020%

*The percentage here refer to the maximum limits of impurities. These impurities were reported by the supplier (Ajax Finechem) on the purchased container.

6.2.2 pH adjustment

Aqueous solution of (0.1 – 1 M) $NaNO_2$ (pH = 5.8 – 7.5), and (0.1 – 1 M) NH_4Cl (pH = 5 – 5.5) were used. Upon mixing, the solution had a pH of (5.5 – 6.5). When required, the pH was adjusted after mixing the reactants by the addition of either 0.5 M HCl or 0.5 M NaOH. The

acid and base solutions were filtered through a 20 nm filter before use. The pH of the solution was measured using a pH meter (smartCHEM-LAB, TPS, Australia).

6.2.3 Nanoparticle Tracking Analysis (NTA)

The size distribution and concentration of nanoparticles were measured using a NanoSight (NS300, Malvern, software Version 3.1) to perform Nanoparticle Tracking Analysis (NTA). Measurements were performed using a blue laser light source (70 mW, $\lambda = 405$ nm). A camera operating at 25 frames/s was used to record a video of the light scattered from nanoparticles in a flow field for 60 s. This enabled numerous nanoparticles to be tracked, measured, and counted. The sample was continuously introduced into the NanoSight measurement cell using a syringe pump (flow rate set to 30 – unspecified units). Each result presented here is the average of five measurements. The camera level was always set at 13, and the threshold was set at 3. The data was analyzed using a viscosity of 0.888 cP for water at 25 °C.

6.2.4 Resonant Mass Measurement (RMM)

Resonant mass measurements (RMM) were conducted using an Archimedes (Malvern Instruments, UK, ParticleLab software version 1.2) to determine the buoyant mass of individual nanoparticles. All experiments were performed at room temperature. Nanosensor chips with embedded channels having dimensions of $2 \times 2\ \mu m^2$ were used in all experiments. Prior to use, they were calibrated with polystyrene standard nanoparticles of diameter of 500 nm (Thermo Fisher Scientific). Data was acquired for 1 hour or until 150 particles had been detected using a threshold frequency change of $\pm 9 \times 10^{-3}$ Hz.

6.2.5 Dynamic light Scattering

A Zetasizer Nano ZS (Malvern) employing a 633-nm He-Ne laser at a scattering angle of 173°, was used to measure the size of particles in solution by dynamic light scattering. Particle size measurements were made with an automatic attenuator at a position of 4.65 mm from the cuvette wall. The dynamic light scattering measurements performed here are the average of three measurements, each consisting of 13 sets of data, each collected over a period of 10 s.

6.3 Results and Discussion

There are numerous chemical reactions that result in the production of gases. However, some of these chemical reactions can lead to the production of species that are not soluble in water and therefore have the potential for solid nanoparticle production, complicating the possible identification of nanobubbles resulting from supersaturation. Even when the chemical reaction itself does not produce insoluble species, it is important to consider the possible production of insoluble species between the reactants, products and contaminants. So for example, species that form insoluble salts with calcium or sulphate ions are best avoided. Another consideration is the type of gas produced. This study avoids reactions that produce CO_2, because CO_2 is far more soluble than most other gases. The production of oxygen from the disproportionation reaction of hydrogen peroxide was considered, as the only other species produced in this reaction is water, but the rate of this reaction is extremely slow at room temperature unless a catalyst is employed[197]. The chemical reaction between NH_4Cl and $NaNO_2$ was utilised in this study to produce nitrogen gas and NaCl which is a very soluble salt (solubility[198] 360 g/L).

$$NH_4Cl\ (aq) + NaNO_2\ (aq) \longrightarrow NaCl\ (aq) + 2H_2O\ (l) + N_2\ (g)$$

Furthermore, the chemical species involved in this reaction form highly soluble salts with most potential contaminant ions, reducing the possibility of nanoparticles of insoluble salts being produced as a result of side reactions. Additionally, the kinetics and mechanism of this reaction have been extensively investigated[199,200].

According to Nguyen *et al*.[199], the reaction between NH_4Cl and $NaNO_2$ in aqueous solutions is greatly dependent on pH and the concentration of the reactants. For example, decreasing the pH from 7 to 3 leads to an increase in the reaction rate by a factor of 4000. The reaction follows first order kinetics with respect to the concentration of ammonium chloride, and second order with respect to the concentration of sodium nitrite. The following rate expression has been proposed[199].

$$\text{Reaction rate} = Ae^{-E`/RT} a_{H^+}^{\alpha}\, C_{\mathrm{NH_4Cl}}^{\beta}\, C_{NaNO_2}^{\gamma} \qquad (6.1)$$

where A is the frequency factor, $E`$ is the Arrhenius activation energy, T is the temperature, R is the ideal gas constant, and α, β, and γ are the orders with respect to hydrogen ions, NH_4Cl and $NaNO_2$ concentrations, respectively. This rate expression is applicable to the pH range used in this study. Using the above rate expression, the amount of nitrogen produced from this reaction at room temperature can be calculated by integrating over time.

The calculated amount of N_2 gas produced over a period of an hour is presented as a function of the initial concentration of the reactants in Figure 6-1A and as a function of pH in Figure 6-1B. As shown, the rate of reaction can be readily manipulated by the choice of NH_4Cl and $NaNO_2$ concentration and the pH.

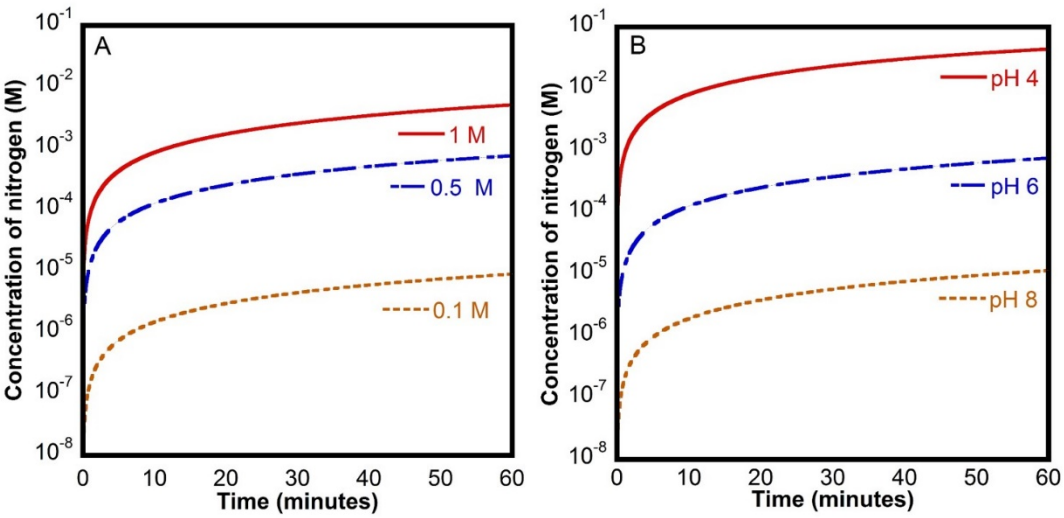

Figure 6-1. Calculated concentration of nitrogen produced versus time at T = 298 K for the chemical reaction between NH_4Cl and $NaNO_2$ at 0.1 M, 0.5 M and 1 M (pH = 6) (Panel A), and at pH 4, pH 6 and pH 8 when the concentration of the reactants is 0.5 M (Panel B). These calculations were made using equation 1 with $\alpha = 0.91$, $\beta = 0.95$, $\gamma = 1.81$, $E^{`} =$ 15.1 Kcal mol^{-1}, and $A = 5.3 \times 10^{10}$ (L mol^{-1})$^{1.76}$ s^{-1} (parameters taken from reference[199]). For data DOI:10.25911/5c7c9aa5eadd6

6.3.1 Nanoparticle Production

The size and concentration of nanoparticles in the solutions after filtration and before mixing were determined using nanoparticle tracking analysis (NTA, Nanosight NS300, Malvern) in order to establish the background level of nanoparticles. Typical total concentrations of particles in NH_4Cl and $NaNO_2$ solutions before mixing were $0.3 \pm 0.1 \times 10^6$ and $1.6 \pm 0.3 \times 10^6$ particles ml^{-1} respectively. This is near the detection limit of the instrument. The very low particle count is expected, given that the solutions had been filtered to remove all particles > 20 nm in size and this technique cannot detect particles smaller than 20 nm. Histograms of the nanoparticles measured in 0.5 M solutions of NH_4Cl and $NaNO_2$ prior to mixing and after filtering are presented in Figure 6-2.

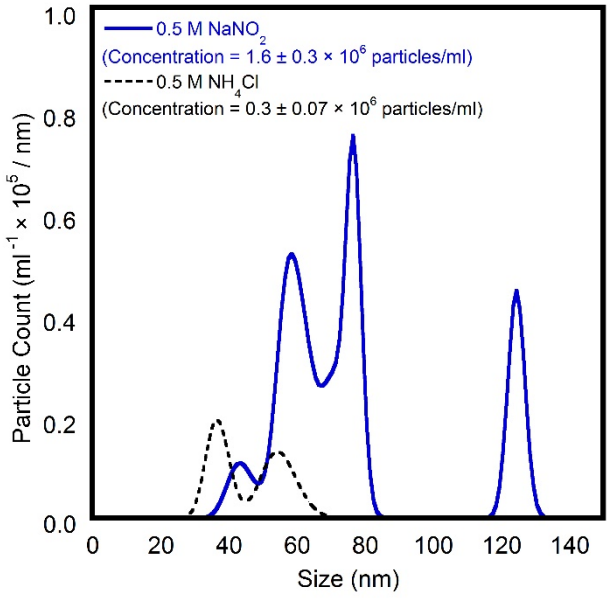

Figure 6-2. Size and concentration distribution (plotted using a bin width of 1 nm) obtained using Nanoparticle Tracking Analysis for each of the filtered reactant solutions (before mixing). The total concentration for each filtered reactant solution is reported in the legend. For data DOI:10.25911/5c807abac18c6

When the solutions were mixed, nanoparticles were readily detected at a concentration typically 2 orders of magnitude greater than in the reactant solutions as seen in Figure 6-3. It was evident that the concentration of nanoparticles had increased greatly due to the chemical reaction and the concentration of nanoparticles increased with increasing reactant concentration. The concentration of the particles produced and measured after 10 minutes was $73.8 \pm 0.9 \times 10^7$ particles ml^{-1} at 1 M, and $48.8 \pm 4 \times 10^7$ particles ml^{-1} at 0.5 M. When the concentration of the reactants was decreased to 0.1 M, a much lower concentration of nanoparticles was produced (i.e. $11.3 \pm 0.9 \times 10^7$ particles ml^{-1}) and the particles were significantly smaller.

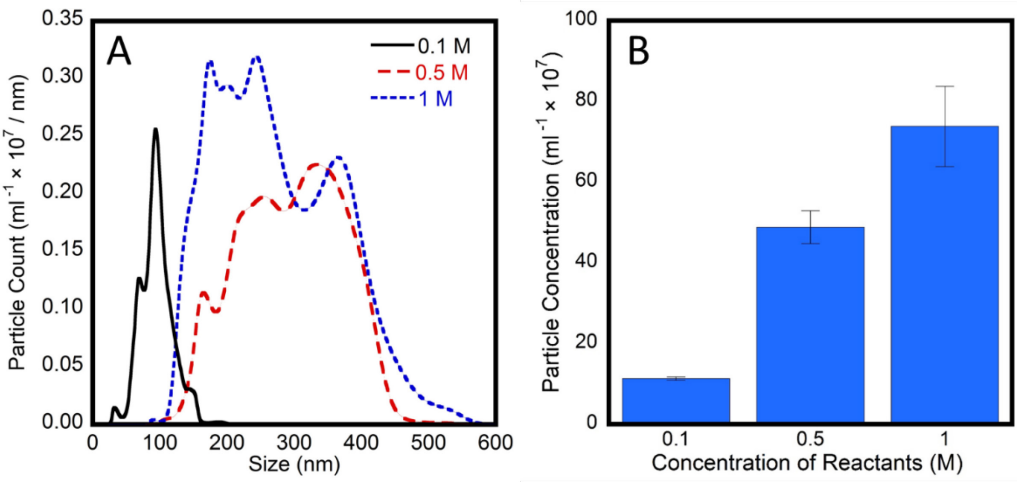

Figure 6-3. Histogram showing the particle size distribution (panel A) and concentration of nanoparticles measured as a function of the initial concentration of the reactants (panel B) measured using Nanoparticle Tracking Analysis for solutions containing NH_4Cl and $NaNO_2$ at equal concentrations of 0.1 M, 0.5 M and 1 M respectively. Measurements here were commenced 10 minutes after mixing the reactants. The displayed error bars correspond to the standard error for five measurements. For data DOI: 10.25911/5c7c982795eb4

The influence of pH on the formation and stability of nanoparticles was also investigated, as pH is known to strongly alter the reaction kinetics. The nanoparticle size was examined using dynamic light scattering and tracked as a function of time. As shown in Figure 6-4A, the size of the particles at pH = 5.9 increased with time, whereas when the reaction pH was adjusted after mixing to a higher value (i.e. pH = 8.7), the size of nanoparticles remained constant with time. This correlates with the reaction kinetics. At the higher pH the reaction rate is greatly decreased and the particle size no longer increases over time. Size measurements on the nanoparticles using NTA showed that the size distribution shifted toward larger particles over time when the pH was not adjusted (see Figure 6-4C), consistent with the DLS measurements. The size distribution data shows that the concentration of these nanoparticles decreased during the first 20 minutes from $55.5 \pm 4.0 \times 10^7$ particles/ml to $33.0 \pm 1.0 \times 10^7$ particles/ml and then continued to decrease to a concentration of $12.8 \pm 0.6 \times 10^7$ particles/ml after 60 minutes (see Figure 6-4B). On the contrary, the size distribution of the nanoparticles obtained at higher pH

was stable over time (see Figure 6-4D), and the concentration varied only slightly in the range of 20-30 × 10^7 particles/ml (see Figure 6-4B).

Several attempts were made to measure nanoparticles produced at pH = 4 directly after mixing, however reliable measurements could not be obtained. This we attribute to the presence of large bubbles in the sample, noting that such bubbles were visible to the naked eye. This is commensurate with the much higher reaction rate expected at the lower pH, due to catalysis by the hydronium ion.

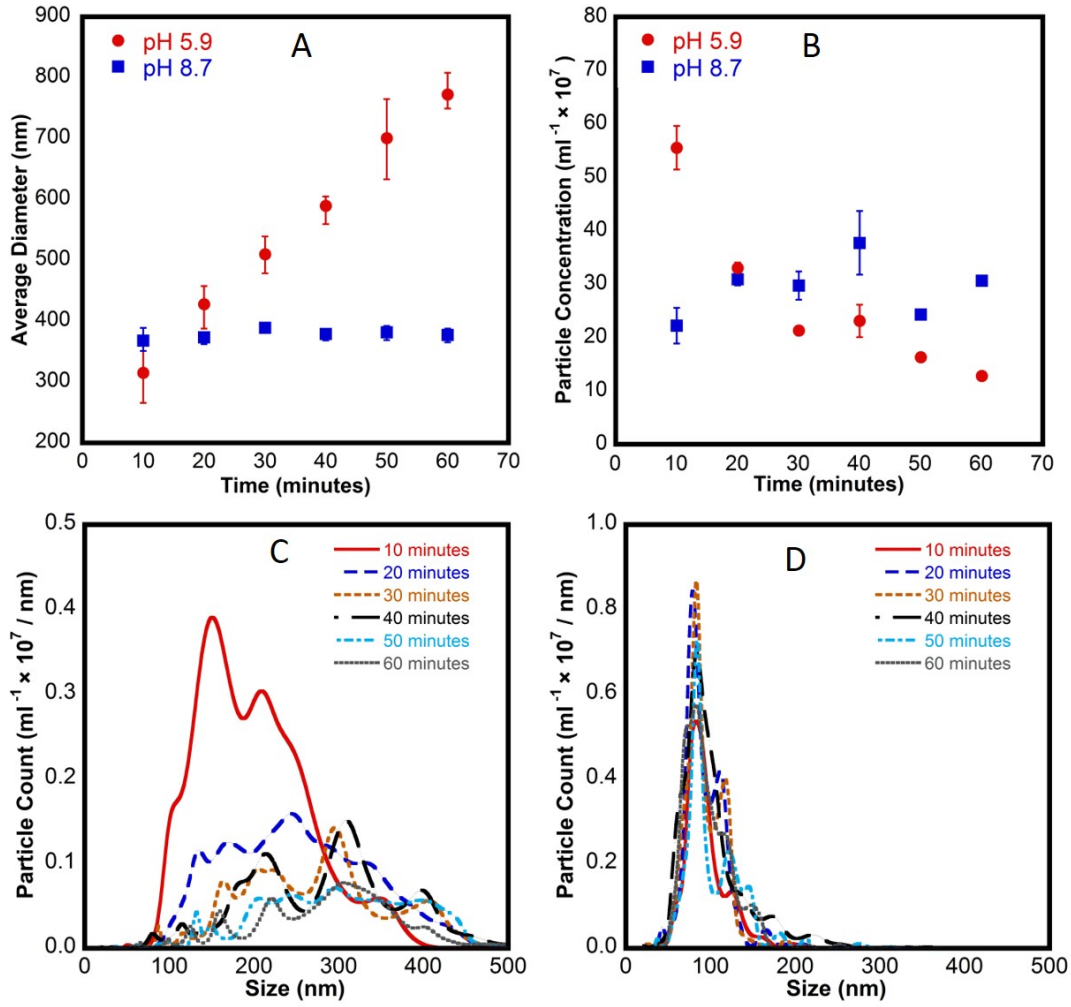

Figure 6-4. The effect of pH on nanoparticle size and concentration produced by the reaction of sodium nitrite and ammonium chloride at equal concentrations of 0.5 M. Panel A: Mean size of nanoparticles measured using dynamic light scattering over 60 minutes for pH 5.9 and 8.7 (The error bars correspond to the maximum and minimum values of three measurements). Panel B: Concentration of the nanoparticles measured using Nanoparticle

Tracking Analysis over a period of 60 minutes at pH 5.9 and 8.7 (The error bars correspond to the standard error for five measurements). Panel C-D: Histograms showing the particle distribution (plotted using a bin width of 1 nm) measured using the NanoSight over 60 minutes at pH 5.9 and pH 8.7 respectively. For data DOI:10.25911/5c7c989e1e54e

This demonstrates that the nanoparticles generated are pH and concentration dependent in a manner that is consistent with the kinetics of nitrogen gas evolution produced in the reaction (see Figure 6-1). This agreement indicates a strong relationship between gas supersaturation and nanoparticle production, however this correlation is not sufficient to conclude that the nanoparticles are gas filled nanobubbles. In order to determine the nature of these nanoparticles the nanoparticles that formed as a result of the chemical reaction were further characterized. In particular, the effect of external pressure on the particle size and resonant mass measurement was used to determine the density of the nanoparticles.

6.3.2 Nanoparticles under pressure

Due to the difference in compressibility between nanobubbles and other nanoparticles, the application of external pressure on candidate nanoparticles can be used to determine if the observed objects are nanobubbles (for further details, see chapter 2).

In this work, particles arising from a gas producing chemical reaction were measured at 1 atm of external pressure, then at 5 atm of external pressure and again at 1 atm pressure. As shown in Figure 6-5A, there is no evidence that the change in external pressure led to a change in particle size in solutions at pH = 5.9, however the particle size increased over time as the chemical reaction proceeded, therefore it is not possible to definitively determine the effect of applied pressure on particle size from these measurements. This problem can be overcome by mixing the reactants and then increasing the pH. At the higher pH, there is a dramatic reduction in the reaction rate and the particle sizes do not change over time, as shown in Figure 6-5B. The

average diameter at 1 atm pressure was 328 nm. Using the ideal gas law and the Laplace pressure (see equations 3.1 and 3.2 in §3.4.1), the expected effect of external pressure on bubble size can be calculated. Nanobubbles under the application of 5 atmospheres of pressure, with an interfacial tension of pure water (i.e. $\gamma = 72.0 \times 10^{-3}\ N\ m^{-1}$) and an initial size of 328 nm are expected to reduce in size to 283 nm. For this calculation, the interfacial tension for a pure air-water interface was used. This is the maximum surface tension that a nanobubble would be expected to have, and therefore the calculation reflects the *minimum* expected reduction in size for a nanobubble under the application of external pressure. In the calculation, a lower surface tension implies a lower Laplace pressure. This leads to a greater expected reduction in size, as the applied pressure is proportionally more significant. In contrast, the experimental data showed a negligible effect of pressure changes on size. This result indicates that these nanoparticles are incompressible which is incommensurate with them being gas filled nanobubbles.

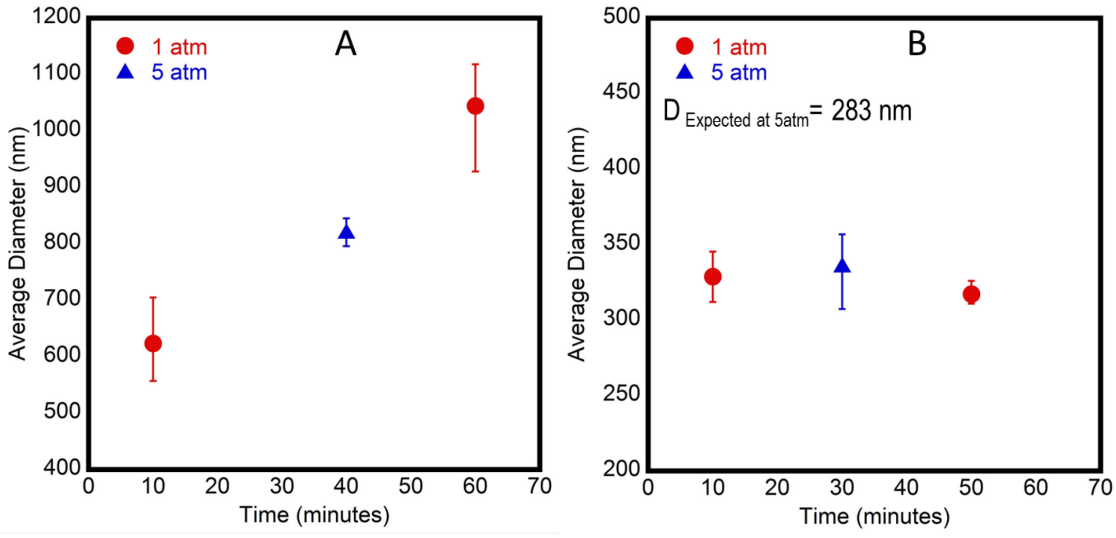

Figure 6-5. Particle size as a function of time determined using dynamic light scattering under an applied external pressure of 1 atm (red squares), and 5 atm (blue triangles) at pH 5.9 (Panel A) and pH 8.7 (Panel B). The pH of the solution was adjusted after mixing the reactants. Each data point is an average of three measurements, and the displayed error bars

correspond to the maximum and minimum values obtained. For data DOI: 10.25911/5c7c99149feae

6.3.3 Resonant Mass Measurement

Another direct technique can be applied to nanobubble candidates to evaluate the nanoparticle density. The Archimedes instrument employs a resonating cantilever with an internal microfluidic channel to determine the buoyant mass of particles in solution as they pass through the channel. The flow of nanoparticles through the sensor alters the resonant frequency of the cantilever. The resonant frequency decreases if the density of the nanoparticle is higher than the solvent and increases if the density of the nanoparticle is lower than the solvent. This is a convenient means of distinguishing heavy particles (i.e. negatively buoyant particles) from light particles (i.e. positively buoyant particles).

The nanoparticles resulting from the chemical reaction were measured using the resonant mass measurement (RMM). The RMM showed nanoparticles of concentration 16.3×10^7 particles ml^{-1} (see Figure 6-6). However, the measurement revealed only negatively buoyant particles. This indicates that the generated particles were not gaseous because the density of all the nanoparticles detected was *greater* than that of water.

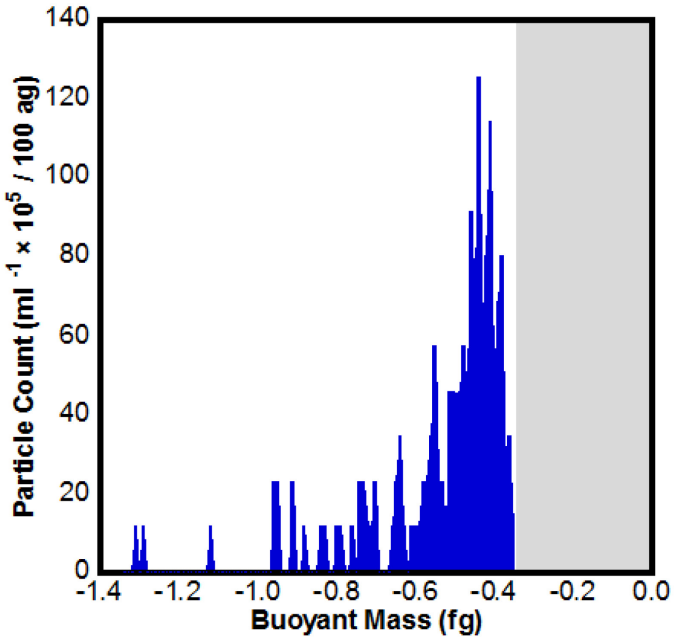

Figure 6-6. Typical buoyant mass distribution measured using resonant mass measurement for nanoparticles generated using the reaction of NH_4Cl and $NaNO_2$ at a concentration of 0.5 M . The concentration of particles was measured as 16.3×10^7 particles ml^{-1}. Due to the limited sensitivity of the Archimedes, particles with a buoyant mass of < |0.4| fg could not be detected (shaded gray region). No positively buoyant particles were detected, demonstrating that the particles have a density greater than that of the solution, which is incommensurate with the nanoparticles being nanobubbles. For data DOI:10.25911/5c7c998b40360

The results from the size determination under the application of external pressure and the resonant mass measurement are in agreement and demonstrate that the particles are *not gas filled nanobubbles,* but either solid nanoparticles or nanodroplets.

These particles result from the chemical reaction but are not nanobubbles. This begs the question as to what these nanoparticles are and how they are formed? Chapter 4 and Chapter 5 proposed a mechanism of generating nanoparticles from the supersaturation of dissolved gases. In this model, the generation of nanoparticles was directly related to the nucleation of bubbles due to supersaturation. Several steps are required. Short lived bubbles form as a result of supersaturation of dissolved gas in the solution. Contaminants present in solution diffuse to the

interface of these bubbles where they become attached. As each bubble dissolves the contaminants are concentrated at the interface, resulting in the formation of nanoparticles of the contaminant material when the bubble completely dissolves. Here the source of this contamination may be the salt solutions or it may arise from the purified laboratory water. Even in very high purity water there is sufficient contaminant material to adsorb to the interface of bubbles to change the hydrodynamic boundary condition from slip to no-slip[118,119].

Is the formation of these nanoparticles associated with supersaturation? For nitrogen in pure water, the solubility is 0.65 mM at atmospheric pressure and T = 298 K; however, the solubility of nitrogen in most electrolytes is generally lower because of the salting out effect[201] associated with electrostriction. Due to the lack of available data on the solubility of nitrogen in aqueous ammonium chloride and sodium nitrite solutions, the solubility of nitrogen in aqueous sodium chloride at the same ionic strength was used as an approximation for the solubility of nitrogen, (S_{N2}) in the nanoparticle solutions (S_{N2} = 0.63 mM @ [C_{NaCl}= 0.1 M] , S_{N2} = 0.56 mM @ [C_{NaCl}= 0.5 M], S_{N2} = 0.48 mM @ [C_{NaCl}= 1.0 M])[201]. The calculated saturation level produced over a period of an hour is presented as a function of initial concentration in Figure 6-7A, and as a function of pH in Figure 6-7B. The relationship between the formation of nanoparticles and the supersaturation becomes evident when looking at Figure 6-3 and Figure 6-7A. That is, the number of generated nanoparticles increased when the concentration of the reactants was higher (i.e. when the level of supersaturation was higher). The highest number of nanoparticles was achieved for reactants at an initial concentration of 1 M, where the corresponding saturation level at the time of the measurement was 2.78 (where a saturation of 1 is achieved when the dissolved nitrogen gas is at the equilibrium concentration). Furthermore, the nanoparticle concentration decreased by a factor of 1.5 when the supersaturation level decreased to 1.23 (ie 1.23 times the calculated saturation level at the initial concentration of 0.5 M at the time of the measurement). It is worth noting that some nanoparticles were observed at the initial

concentration of 0.1 M where the saturation level was calculated to be barely above 1. However, the error in the rate equation is significant and the level of saturation may be considerably greater within the 95% confidence interval. Thus, it is concluded that nanoparticle formation is directly related to the supersaturation of dissolved nitrogen resulting from the chemical reaction.

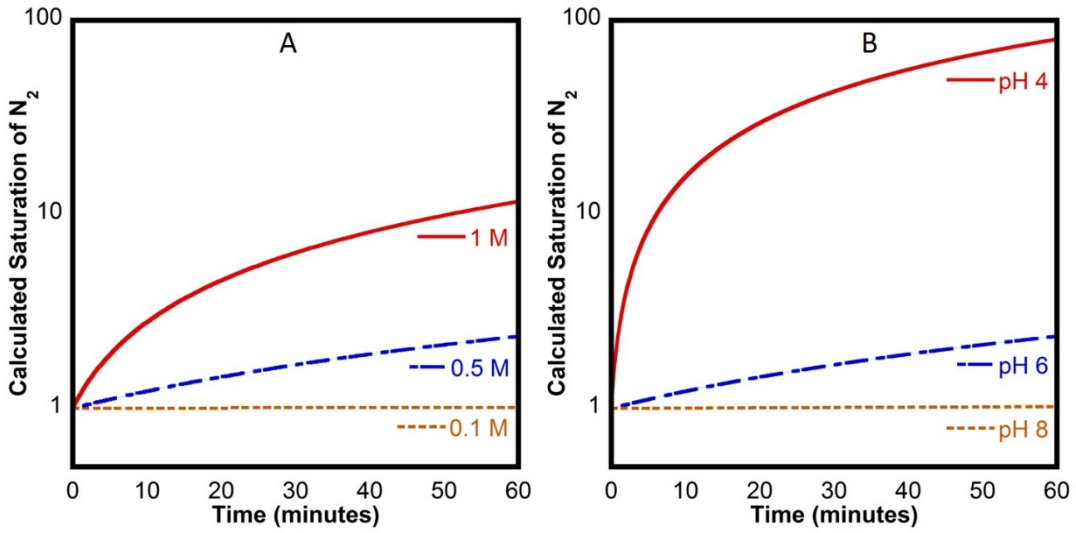

Figure 6-7. Calculated saturation of nitrogen produced over 60 minutes at T= 298 K for the chemical reaction between NH_4Cl and $NaNO_2$ at initial concentrations of 0.1 M, 0.5 M and 1 M (pH = 6) (Panel A), and at pH 4, pH 6 and pH 8 when the initial concentration of the reactants is 0.5 M (Panel B). The saturation level of N_2 was calculated using equation 6.1 and the solubility of nitrogen gas in solution was taken to be equivalent to that in aqueous sodium chloride at the same ionic strength (S_{N2} = 0.63 mM @ [C_{NaCl}= 0.1 M] , S_{N2} = 0.56 mM @ [C_{NaCl}= 0.5 M], S_{N2} = 0.48 mM @ [C_{NaCl}= 1.0 M])[201]. For data DOI: 10.25911/5c7c9a02b097a

6.4 Summary

This work has tested the hypothesis that supersaturation obtained by a chemical reaction between aqueous solutions of ammonium chloride and sodium nitrite produces long-lived nanosized bubbles in bulk. The formation of nanoparticles was consistent with the kinetics of nitrogen gas evolution produced in the reaction, where the nanoparticle size was shown to be dependent on the pH and concentration of the reactants. However, the chemical reaction was found to generate incompressible nanoparticles with a density larger than that of the solvent, confirming that these particles were not gas-filled bubbles.

Chapter 7 Conclusions and Future Work

7.1 Conclusions

The field of bulk nanobubbles has been challenged by a lack of direct methods that can differentiate nanobubbles from other nanoparticles in aqueous solutions, particularly as their long-term stability would seem to violate either the Laplace pressure or Henry's Law. This has caused ambiguity in the field and led to reports of long-lived bulk nanobubbles being treated with scepticism. To address this, this thesis has established a systematic study to examine reports of the existence of long-lived bulk nanobubbles in aqueous solutions. This required the development of a reliable protocol for testing candidate nanoparticle dispersions. The main experimental results and their implications are summarized below.

Two robust methods for differentiating long-lived nanobubbles from other nanoparticles were developed and applied in this thesis. The density of nanoparticles was determined using resonant mass measurement, and the size of nanoparticles was measured under the influence of external pressure to evaluate the compressibility of the nanoparticles. As the density and compressibility of gasses are very different from those of liquids and solids, these methods can be used to differentiate between nanobubbles and other nanoparticles.

These two methods were applied to nanobubbles armoured with a shell of surface active molecules *(*i.e. *armoured nanobubbles*) that have been used commercially in ultrasound imaging. The resonant mass measurement revealed a significant population of lipid-coated gas nanobubbles. These nanobubbles were shown to be gas entities by their response to the application of pressure. The hypothesis that the pressure response of nanobubbles can be used to differentiate them from other nanoparticles has been confirmed, even when the nanobubbles

were armoured with a shell of insoluble lipid. The pressure at which the gas within the nanobubbles condensed was shifted higher due to the mechanical resistance of the lipid shell which shields the bubble contents of up to ~ 0.8 atm of pressure. The presence of lipids of low solubility at the nanobubble-solution interface effectively results in a negative Laplace pressure which stabilizes the nanobubbles against dissolution.

The protocols developed here that measure the density and the pressure response of nanoparticles was also applied to investigate the existence of unarmoured bulk nanobubbles in systems that have been reported to contain long-lived bulk nanobubbles. These systems are:

- Nanoparticles produced by mechanical means that involve pressure cycling
- The mixing of ethanol and water
- Nitrogen supersaturation by chemical reaction

The determined density of the nanoparticles in these systems was inconsistent with them being gas-filled. Further, external pressure had no effect on the size of these nanoparticles. These experimental results have confirmed that these nanoparticles are not bulk nanobubbles despite references to nanoparticles produced by similar means in the literature being reported as bulk nanobubbles.

It has been demonstrated that that the supersaturation of dissolved gasses in these systems results in the formation of nanoparticles on the order of ~ 100 nm in diameter. These nanoparticles were shown to be stable for hours for those produced by chemical reaction and days for those produced by mechanical means and ethanol water mixing. A mechanism is proposed to explain the puzzling formation of these nanoparticles during the generation process that lead to gas supersaturation. In this mechanism, bubbles form during generation and attract contaminants to their interface. Complete dissolution of these bubbles leads to the formation of nanoparticles originating from the material that has accumulated at the interface. This model was supported by the results of experiments using degassed solutions. A significant reduction

in the number of nanoparticles was observed upon mixing degassed ethanol and degassed water. In addition, the number of nanoparticles was restored when mixing solvents that had been allowed to re-gas, indicating that the supersaturation is essential for forming these nanoparticles.

Finally, the results presented in this thesis showed that the long-term stability of nanobubbles was only observed when they were armoured with an insoluble material. Whilst the lack of evidence for nanobubbles in the systems studied here cannot be extrapolated to all systems, it does cast doubt on claims of long-lived unarmoured bulk nanobubbles, as there is no known mechanism for their stability and this work has explained how the formation of short lived bubbles can lead to the production of nanoparticles. The correlation between the generation process and the formation of nanoparticles is often cited as evidence of the formation of nanobubbles. This work demonstrated that this correlation is insufficient to conclude that the particles formed are nanobubbles. It is expected that adoption of the approach proposed in this thesis will progress the field by enabling claims of long-lived stable gas nanobubbles to be easily evaluated, eliminating the need to rely on indirect and circumstantial evidence. This will reduce the incidence of confusing and misleading reports. This will enable researchers to focus on systems in which the existence of nanobubbles has been proven and thereby facilitate a deeper understanding of bulk nanobubbles.

In summary, the following hypotheses were tested in this work, leading to the following conclusions

- The pressure response of nanobubbles can be used to differentiate them from other nanoparticles, even when the nanobubbles are armoured with a shell of insoluble lipid.

  Confirmed

- The density of nanoparticles can be determined using the resonant mass measurement method.

  Confirmed

- Long-lived bulk nanobubbles can be generated by mechanical means.

  Refuted on the samples studied

- The mixing of ethanol and water produces stable long-lived bulk nanobubbles.

  Refuted

- Supersaturation obtained by a chemical reaction produces long-lived nanosized bubbles in bulk.

  Refuted

7.2 Future work

This study focused on three particular methods that have been reported to produce nanobubbles. Other claims of long-lived bulk nanobubbles could be tested using the protocols developed in this thesis, for example it has been reported that increasing the temperature of aqueous solutions leads to the formation of bulk nanobubbles[45], a claim which was investigated during the present study. Around room temperature, increasing solution temperature leads to a reduction in the solubility of dissolved gasses. In these experiments, a closed cuvette of high purity water that had been kept at 6–10˚C in a glass flask for 24 hours was measured using dynamic light scattering both before and after a temperature change to 45˚C. However, reliable measurements could not be obtained because of the formation of larger bubbles. In the future, this experiment could be redesigned to remove or reduce the interference from larger bubbles. If nanoparticles

were evident, the protocol established in this study could then be used to investigate and determine if they were actually nanobubbles.

It has been shown in this thesis that the dissolution of short-lived bubbles produced by supersaturation is a mechanism for the formation of nanoparticles. This mechanism could also lead to the production of nanoparticles in natural processes wherever bubbles are formed, such as the breaking of ocean waves and at the base of waterfalls. Under these circumstances nanoparticles may be produced when bubbles accumulate surface-active material in solution and dissolve. Using carefully filtered natural waters, tracking analysis could be employed to investigate the concentration of nanoparticles before and after shaking or pouring of the samples. If nanoparticles are generated in this process it will indicate that huge numbers of nanoparticles may be produced in this manner.

It is possible that many of the properties ascribed to nanobubbles are in fact due to nanoparticles formed during processes designed to produce nanobubble, indicating that nanoparticles formed from the collapse of bubbles may have useful applications. Such nanoparticles are therefore likely to be common and widespread. Moreover, the process of concentrating material into a nanoparticle increases its chemical potential and, therefore, its chemical activity and biological availability. As such, these nanoparticles may be the active component responsible for benefits previously ascribed to nanobubbles, including plant growth and seed germination [30–37] and water remediation [12–17].

The results presented in this thesis shed light on a convenient method for producing nanoparticles by highlighting the potential use of supersaturation of dissolved gas for this purpose (see §4.3.4, §5.3, and §6.3). This approach has recently been utilized by Diao *et al*.[202] who report a method for generating hollow nanoparticles from material added to solution via supersaturation of dissolved gas[202]. In this study, supersaturation was achieved by mixing ethanol and water. Added particles of molybdenum carbide self-assembled at the interface of

the shrinking bubbles, form hollow spheres. The hollow region beneath the shell was confirmed using a field emission scanning electron microscope. The production of these hollow nanospheres correlated with the supersaturation of the dissolved gas. This conclusion was supported by the finding that hollow nanoparticles could not be generated when the saturation level was significantly decreased, demonstrating the need for bubble formation and the accumulation of material at the bubble interface. This indicates that the type of contaminant, its corresponding concentration and supersaturation of the dissolved gas are essential elements for the formation and constitution of nanoparticles. This process should be studied further by utilizing the supersaturation methods presented in this thesis to understand more precisely how such nanoparticles are formed and to what extent they can be controlled, with the potential for low-cost nanoparticle generation. This simple inexpensive method will likely attract researchers from different fields for nanoparticle formation to avoid the complex methods of producing nanoparticles that have been employed in laboratory and industry.

Further, the present study in this thesis could be expanded further with the potential aim of developing, stabilizing, destroying, and controlling the size of nanobubbles armoured with materials of interest ranging from solid coatings to lipid/polymer coatings via supersaturation of dissolved gas. Lipid/Polymer coated nanobubbles have a potential application in ultrasound imaging[3–8] and therapeutic drug delivery [6,9–11], while those with solid coatings have potential interest as hollow nanospheres, with shells of silica, metals, metal oxides or other complex solids, in a variety of applications such as catalysis[121,203,204], energy storage[205–210], sensors[211] and environmental remediation[212,213] because of their low density, large surface area, and high loading capacity[214].

This work has shown that that stable long-lived nanobubbles are only likely to exist when they have an armour of insoluble material. Whilst this rules out many potential applications of

nanobubbles, the demonstration that shrinking bubbles template nanoparticles opens up a whole new area for investigation.

References

(1) Epstein, P. S.; Plesset, M. S. On the Stability of Gas Bubbles in Liquid-Gas Solutions. *J. Chem. Phys.* **1950**, *18*, 1505–1509.

(2) Ljunggren, S.; Eriksson, J. C. The Lifetime of a Colloid-Sized Gas Bubble in Water and the Cause of the Hydrophobic Attraction. *Colloids Surfaces A Physicochem. Eng. Asp.* **1997**, *129–130*, 151–155.

(3) Wu, H.; Rognin, N. G.; Krupka, T. M.; Solorio, L.; Yoshiara, H.; Guenette, G.; Sanders, C.; Kamiyama, N.; Exner, A. A. Acoustic Characterization and Pharmacokinetic Analyses of New Nanobubble Ultrasound Contrast Agents. *Ultrasound Med. Biol.* **2013**, *39*, 2137–2146.

(4) Krupka, T. M.; Solorio, L.; Wilson, R. E.; Wu, H.; Azar, N.; Exner, A. A. Formulation and Characterization of Echogenic Lipid−Pluronic Nanobubbles. *Mol. Pharm.* **2010**, *7*, 49–59.

(5) Perera, R. H.; Solorio, L.; Wu, H.; Gangolli, M.; Silverman, E.; Hernandez, C.; Peiris, P. M.; Broome, A.-M.; Exner, A. A. Nanobubble Ultrasound Contrast Agents for Enhanced Delivery of Thermal Sensitizer to Tumors Undergoing Radiofrequency Ablation. *Pharm. Res.* **2014**, *31*, 1407–1417.

(6) Wang, Y.; Li, X.; Zhou, Y.; Huang, P.; Xu, Y. Preparation of Nanobubbles for Ultrasound Imaging and Intracelluar Drug Delivery. *Int. J. Pharm.* **2010**, *384*, 148–153.

(7) Suzuki, R.; Takizawa, T.; Negishi, Y.; Utoguchi, N.; Maruyama, K. Effective Gene Delivery with Novel Liposomal Bubbles and Ultrasonic Destruction Technology. *Int. J. Pharm.* **2008**, *354*, 49–55.

(8) Yin, T.; Wang, P.; Zheng, R.; Zheng, B.; Cheng, D.; Zhang, X.; Shuai, X. Nanobubbles for Enhanced Ultrasound Imaging of Tumors. *Int. J. Nanomedicine* **2012**, *7*, 895–904.

(9) Oeffinger, B. E.; Wheatley, M. A. Development and Characterization of a Nano-Scale Contrast Agent. *Ultrasonics* **2004**, *42*, 343–347.

(10) Misra, S. K.; Ghoshal, G.; Gartia, M. R.; Wu, Z.; De, A. K.; Ye, M.; Bromfield, C. R.; Williams, E. M.; Singh, K.; Tangella, K. V.; et al. Trimodal Therapy: Combining Hyperthermia with Repurposed Bexarotene and Ultrasound for Treating Liver Cancer. *ACS Nano* **2015**, *9*, 10695–10718.

(11) Meng, M.; Gao, J.; Wu, C.; Zhou, X.; Zang, X.; Lin, X.; Liu, H.; Wang, C.; Su, H.; Liu, K.; et al. Doxorubicin Nanobubble for Combining Ultrasonography and Targeted Chemotherapy of Rabbit with VX2 Liver Tumor. *Tumor Biol.* **2016**, *37*, 8673–8680.

(12) Wang, L.; Miao, X.; Ali, J.; Lyu, T.; Pan, G. Quantification of Oxygen Nanobubbles in Particulate Matters and Potential Applications in Remediation of Anaerobic Environment. *ACS Omega* **2018**, *3*, 10624–10630.

(13) Agarwal, A.; Ng, W. J.; Liu, Y. Principle and Applications of Microbubble and Nanobubble Technology for Water Treatment. *Chemosphere* **2011**, *84*, 1175–1180.

(14) Xia, Z.; Hu, L. Treatment of Organics Contaminated Wastewater by Ozone Micro-Nano-Bubbles. *Water* **2018**, *11*, 55.

(15) Li, H.; Hu, L.; Song, D.; Lin, F. Characteristics of Micro-Nano Bubbles and Potential Application in Groundwater Bioremediation. *Water Environ. Res.* **2014**, *86*, 844–851.

(16) Atkinson, A. J.; Apul, O. G.; Schneider, O.; Garcia-Segura, S.; Westerhoff, P. Nanobubble Technologies Offer Opportunities To Improve Water Treatment. *Acc. Chem. Res.* **2019**.

(17) Kyzas, G. Z.; Bomis, G.; Kosheleva, R. I.; Efthimiadou, E. K.; Favvas, E. P.; Kostoglou, M.; Mitropoulos, A. C. Nanobubbles Effect on Heavy Metal Ions Adsorption by Activated Carbon. *Chem. Eng. J.* **2019**, *356*, 91–97.

(18) Calgaroto, S.; Wilberg, K. Q.; Rubio, J. On the Nanobubbles Interfacial Properties and Future Applications in Flotation. *Miner. Eng.* **2014**, *60*, 33–40.

(19) Calgaroto, S.; Azevedo, A.; Rubio, J. Separation of Amine-Insoluble Species by Flotation with Nano and Microbubbles. *Miner. Eng.* **2016**, *89*, 24–29.

(20) Maoming, F.; Daniel, T.; Rick, H.; Zhenfu, L. Nanobubble Generation and Its Applications in Froth Flotation (Part IV): Mechanical Cells and Specially Designed Column Flotation of Coal. *Min. Sci. Technol. 20*, 641–671.

(21) Fan, M.; Tao, D. A Study on Picobubble Enhanced Coarse Phosphate Froth Flotation. *Sep. Sci. Technol.* **2008**, *43*, 1–10.

(22) Sobhy, A.; Tao, D. Nanobubble Column Flotation of Fine Coal Particles and Associated Fundamentals. *Int. J. Miner. Process.* **2013**, *124*, 109–116.

(23) Wu, L.; Han, Y.; Zhang, Q.; Zhao, S. Effect of External Electric Field on Nanobubbles at the Surface of Hydrophobic Particles during Air Flotation. *RSC Adv.* **2019**, *9*, 1792–1798.

(24) Fan, M.; Tao, D.; Honaker, R.; Luo, Z. Nanobubble Generation and Its Application in Froth Flotation (Part I): Nanobubble Generation and Its Effects on Properties of Microbubble and Millimeter Scale Bubble Solutions. *Min. Sci. Technol.* **2010**, *20*, 1–19.

(25) Fan, M.; Tao, D.; Zhao, Y.; Honaker, R. Effect of Nanobubbles on the Flotation of Different Sizes of Coal Particle. *Mining, Metall. Explor.* **2013**, *30*, 157–161.

(26) Nazari, S.; Shafaei, S. Z.; Gharabaghi, M.; Ahmadi, R.; Shahbazi, B.; Maoming, F. Effects of Nanobubble and Hydrodynamic Parameters on Coarse Quartz Flotation. *Int. J. Min. Sci. Technol.* **2019**, *29*, 289–295.

(27) Fan, M.; Tao, D. EFFECT OF NANOBUBBLES ON FLOTATION OF DIFFERENT DENSITY COAL. In *SME Annual Meeting*; 2014.

(28) FAN, M.; TAO, D.; HONAKER, R.; LUO, Z. Nanobubble Generation and Its Applications in Froth Flotation (Part II): Fundamental Study and Theoretical Analysis. *Min. Sci. Technol.* **2010**, *20*, 159–177.

(29) FAN, M.; TAO, D.; HONAKER, R.; LUO, Z. Nanobubble Generation and Its Applications in Froth Flotation (Part III): Specially Designed Laboratory Scale Column Flotation of Phosphate. *Min. Sci. Technol.* **2010**, *20*, 317–338.

(30) Khaled, A.; Ahmed, A.; Shi, X.; Hua, L.; Manzueta, L.; Qing, W.; Marhaba, T.; Zhang, W. Influences of Air, Oxygen, Nitrogen, and Carbon Dioxide Nanobubbles on Seed Germination and Plant Growth. *J. Agric. Food Chem.* **2018**, *66*, 5117–5124.

(31) Liu, S.; Oshita, S.; Kawabata, S.; Makino, Y.; Yoshimoto, T. Identification of ROS Produced by Nanobubbles and Their Positive and Negative Effects on Vegetable Seed Germination. *Langmuir* **2016**, *32*, 11295–11302.

(32) Schenk, H. J.; Steppe, K.; Jansen, S. Nanobubbles: A New Paradigm for Air-Seeding in Xylem. *Trends Plant Sci.* **2015**, *20*, 199–205.

(33) Liu, S.; Kawagoe, Y.; Makino, Y.; Oshita, S. Effects of Nanobubbles on the Physicochemical Properties of Water: The Basis for Peculiar Properties of Water Containing Nanobubbles. *Chem. Eng. Sci.* **2013**, *93*, 250–256.

(34) Ebina, K.; Shi, K.; Hirao, M.; Hashimoto, J.; Kawato, Y.; Kaneshiro, S.; Morimoto, T.; Koizumi, K.; Yoshikawa, H. Oxygen and Air Nanobubble Water Solution Promote the Growth of Plants, Fishes, and Mice. *PLoS One* **2013**, *8*, e65339.

(35) Zhou, Y.; Li, Y.; Liu, X.; Wang, K.; Muhammad, T. Synergistic Improvement in Spring Maize Yield and Quality with Micro/Nanobubbles Water Oxygation. *Sci. Rep.* **2019**, *9*, 5226.

(36) Liu, S.; Oshita, S.; Makino, Y.; Wang, Q.; Kawagoe, Y.; Uchida, T. Oxidative Capacity of Nanobubbles and Its Effect on Seed Germination. *ACS Sustain. Chem. Eng.* **2016**, *4*, 1347–1353.

(37) Liu, S.; Oshita, S.; Kawabata, S.; Thuyet, D. Q. Nanobubble Water's Promotion Effect of Barley (*Hordeum Vulgare* L.) Sprouts Supported by RNA-Seq Analysis. *Langmuir* **2017**, *33*, 12478–12486.

(38) Wu, Z.; Chen, H.; Dong, Y.; Mao, H.; Sun, J.; Chen, S.; Craig, V. S. J.; Hu, J. Cleaning Using Nanobubbles: Defouling by Electrochemical Generation of Bubbles. *J. Colloid Interface Sci.* **2008**, *328*, 10–14.

(39) Oh, S. H.; Yoon, S. H.; Song, H.; Han, J. G.; Kim, J.-M. Effect of Hydrogen Nanobubble Addition on Combustion Characteristics of Gasoline Engine. *Int. J. Hydrogen Energy* **2013**, *38*, 14849–14853.

(40) Oh, S. H.; Han, J. G.; Kim, J.-M. Long-Term Stability of Hydrogen Nanobubble Fuel. *Fuel* **2015**, *158*, 399–404.

(41) Häbich, A.; Ducker, W.; Dunstan, D. E.; Zhang, X. Do Stable Nanobubbles Exist in Mixtures of Organic Solvents and Water? *J. Phys. Chem. B* **2010**, *114*, 6962–6967.

(42) Leroy, V.; Norisuye, T. Investigating the Existence of Bulk Nanobubbles with Ultrasound. *ChemPhysChem* **2016**, *17*, 2787–2790.

(43) Kim, J.-Y.; Song, M.-G.; Kim, J.-D. Zeta Potential of Nanobubbles Generated by Ultrasonication in Aqueous Alkyl Polyglycoside Solutions. *J. Colloid Interface Sci.* **2000**, *223*, 285–291.

(44) Jin, F.; Ye, J.; Hong, L.; Lam, H.; Wu, C. Slow Relaxation Mode in Mixtures of Water and Organic Molecules: Supramolecular Structures or Nanobubbles? *J. Phys. Chem. B* **2007**, *111*, 2255–2261.

(45) Najafi, A. S.; Drelich, J.; Yeung, A.; Xu, Z.; Masliyah, J. A Novel Method of Measuring Electrophoretic Mobility of Gas Bubbles. *J. Colloid Interface Sci.* **2007**, *308*, 344–350.

(46) Kikuchi, K.; Tanaka, Y.; Saihara, Y.; Ogumi, Z. Study of Hydrogen Nanobubbles in Solution in the Vicinity of a Platinum Wire Electrode Using Double-Potential Step Chronoamperometry. *Electrochim. Acta* **2006**, *52*, 904–913.

(47) Kikuchi, K.; Ioka, A.; Oku, T.; Tanaka, Y.; Saihara, Y.; Ogumi, Z. Concentration Determination of Oxygen Nanobubbles in Electrolyzed Water. *J. Colloid Interface Sci.* **2009**, *329*, 306–309.

(48) Ohgaki, K.; Khanh, N. Q.; Joden, Y.; Tsuji, A.; Nakagawa, T. Physicochemical

Approach to Nanobubble Solutions. *Chem. Eng. Sci.* **2010**, *65*, 1296–1300.

(49) Ushikubo, F. Y.; Furukawa, T.; Nakagawa, R.; Enari, M.; Makino, Y.; Kawagoe, Y.; Shiina, T.; Oshita, S. Evidence of the Existence and the Stability of Nano-Bubbles in Water. *Colloids Surfaces A Physicochem. Eng. Asp.* **2010**, *361*, 31–37.

(50) Uchida, T.; Oshita, S.; Ohmori, M.; Tsuno, T.; Soejima, K.; Shinozaki, S.; Take, Y.; Mitsuda, K. Transmission Electron Microscopic Observations of Nanobubbles and Their Capture of Impurities in Wastewater. *Nanoscale Res. Lett.* **2011**, *6*, 295.

(51) Kobayashi, H.; Maeda, S.; Kashiwa, M.; Fujita, T. Measurement and Identification of Ultrafine Bubbles by Resonant Mass Measurement Method. In *Proceedings of SPIE*; Aya, N., Iki, N., Shimura, T., Shirai, T., Eds.; 2014; p 92320S.

(52) Lyklema, J. Interfacial Potentials: Measuring the Immeasurable? *Substantia* **2017**, *1*, 75–93.

(53) Takahashi, M. ζ Potential of Microbubbles in Aqueous Solutions: Electrical Properties of the Gas−Water Interface. *J. Phys. Chem. B* **2005**, *109*, 21858–21864.

(54) Kodama, Y.; Kakugawa, A.; Takahashi, T.; Kawashima, H. Experimental Study on Microbubbles and Their Applicability to Ships for Skin Friction Reduction. *Int. J. Heat Fluid Flow* **2000**, *21*, 582–588.

(55) Takeuchi, S.; Sato, T.; Kawashima, N. Nonlinear Response of Microbubbles Coated with Surfactant Membrane Developed as Ultrasound Contrast Agent—Experimental Study and Numerical Calculations. *Colloids Surfaces B Biointerfaces* **2002**, *24*, 207–216.

(56) Takahashi, M.; Kawamura, T.; Yamamoto, Y.; Ohnari, H.; Himuro, S.; Shakutsui, H. Effect of Shrinking Microbubble on Gas Hydrate Formation. *J. Phys. Chem. B* **2003**, *107*, 2171–2173.

(57) Creux, P.; Lachaise, J.; Graciaa, A.; Beattie, J. K. Specific Cation Effects at the Hydroxide-Charged Air/Water Interface. *J. Phys. Chem. C* **2007**, *111*, 3753–3755.

(58) Beattie, J. K.; Djerdjev, A. M.; Warr, G. G. The Surface of Neat Water Is Basic. *Faraday Discuss.* **2009**, *141*, 31–39.

(59) Petersen, P. B.; Saykally, R. J. Evidence for an Enhanced Hydronium Concentration at the Liquid Water Surface. *J. Phys. Chem. B* **2005**, *109*, 7976–7980.

(60) Buch, V.; Milet, A.; Vácha, R.; Jungwirth, P.; Devlin, J. P. Water Surface Is Acidic. *Proc. Natl. Acad. Sci. U. S. A.* **2007**, *104*, 7342–7347.

(61) Sengupta, S.; Moberg, D. R.; Paesani, F.; Tyrode, E. Neat Water–Vapor Interface: Proton Continuum and the Nonresonant Background. *J. Phys. Chem. Lett.* **2018**, *9*, 6744–6749.

(62) Nirmalkar, N.; Pacek, A. W.; Barigou, M. On the Existence and Stability of Bulk Nanobubbles. *Langmuir* **2018**, *34*, 10964–10973.

(63) Israelachvili, J. N. Intermolecular and Surface Forces; Academic Press, 2011.

(64) Craig, V. S. J. Very Small Bubbles at Surfaces—the Nanobubble Puzzle. *Soft Matter* **2011**, *7*, 40–48.

(65) Parker, J. L.; Claesson, P. M.; Attard, P. Bubbles, Cavities, and the Long-Ranged Attraction between Hydrophobic Surfaces. *J. Phys. Chem.* **1994**, *98*, 8468–8480.

(66) Zhang, X. H.; Khan, A.; Ducker, W. A. A Nanoscale Gas State. *Phys. Rev. Lett.* **2007**, *98*, 136101.

(67) Seo, D.; German, S. R.; Mega, T. L.; Ducker, W. A. Phase State of Interfacial

Nanobubbles. *J. Phys. Chem. C* **2015**, *119*, 14262–14266.

(68) Ducker, W. A. Contact Angle and Stability of Interfacial Nanobubbles. *Langmuir* **2009**, *25*, 8907–8910.

(69) Brenner, M. P.; Lohse, D. Dynamic Equilibrium Mechanism for Surface Nanobubble Stabilization. *Phys. Rev. Lett.* **2008**, *101*, 214505.

(70) Weijs, J. H.; Lohse, D. Why Surface Nanobubbles Live for Hours. *Phys. Rev. Lett.* **2013**, *110*, 054501.

(71) Zhang, X.; Chan, D. Y. C.; Wang, D.; Maeda, N. Stability of Interfacial Nanobubbles. *Langmuir* **2013**, *29*, 1017–1023.

(72) Liu, Y.; Wang, J.; Zhang, X.; Wang, W. Contact Line Pinning and the Relationship between Nanobubbles and Substrates. *J. Chem. Phys.* **2014**, *140*, 054705.

(73) Qian, J.; Craig, V. S. J.; Jehannin, M. Long-Term Stability of Surface Nanobubbles in Undersaturated Aqueous Solution. *Langmuir* **2019**, *35*, 718–728.

(74) Tan, B. H.; An, H.; Ohl, C.-D. Surface Nanobubbles Are Stabilized by Hydrophobic Attraction. *Phys. Rev. Lett.* **2018**, *120*, 164502.

(75) Sette, D.; Wanderlingh, F. Nucleation by Cosmic Rays in Ultrasonic Cavitation. *Phys. Rev.* **1962**, *125*, 409–417.

(76) Hemmingsen, E. A. Cavitation in Gas−supersaturated Solutions. *J. Appl. Phys.* **1975**, *46*, 213–218.

(77) Bunkin, N. F.; Bunkin, F. V. Bubbstons: Stable Microscopic Gas Bubbles in Very Dilute Electrolytic Solutions. *Sov. Phys. JETP* **1992**, *74*, 271–278.

(78) Bunkin, N. F.; Kochergin, A. V.; Lobeyev, A. V.; Ninham, B. W.; Vinogradova, O. I. Existence of Charged Submicrobubble Clusters in Polar Liquids as Revealed by Correlation between Optical Cavitation and Electrical Conductivity. *Colloids Surfaces A Physicochem. Eng. Asp.* **1996**, *110*, 207–212.

(79) Bunkin, N. F.; Lobeyev, A. V; Lyakhov, G. A.; Ninham, B. W. Mechanism of Low-Threshold Hypersonic Cavitation Stimulated by Broadband Laser Pump. *Phys. Rev. E* **1999**, *60*, 1681.

(80) Yang, C.; Dabros, T.; Li, D.; Czarnecki, J.; Masliyah, J. H. Measurement of the Zeta Potential of Gas Bubbles in Aqueous Solutions by Microelectrophoresis Method. *J. Colloid Interface Sci.* **2001**, *243*, 128–135.

(81) Jayaprakash, A.; Choi, J.-K.; Chahine, G. L.; Martin, F.; Donnelly, M.; Franc, J.-P.; Karimi, A. Scaling Study of Cavitation Pitting from Cavitating Jets and Ultrasonic Horns. *Wear* **2012**, *296*, 619–629.

(82) Dougherty, G. M.; Rose, K. A.; Tok, J. B.-H.; Pannu, S. S.; Chuang, F. Y. S.; Sha, M. Y.; Chakarova, G.; Penn, S. G. The Zeta Potential of Surface-Functionalized Metallic Nanorod Particles in Aqueous Solution. *Electrophoresis* **2008**, *29*, 1131–1139.

(83) Cho, S.-H.; Kim, J.-Y.; Chun, J.-H.; Kim, J.-D. Ultrasonic Formation of Nanobubbles and Their Zeta-Potentials in Aqueous Electrolyte and Surfactant Solutions. *Colloids Surfaces A Physicochem. Eng. Asp.* **2005**, *269*, 28–34.

(84) Mo, C.-R.; Wang, J.; Fang, Z.; Zhou, L.-M.; Zhang, L.-J.; Hu, J. Formation and Stability of Ultrasonic Generated Bulk Nanobubbles. *Chinese Phys. B* **2018**, *27*, 118104.

(85) Hain, N.; Wesner, D.; Druzhinin, S. I.; Schönherr, H. Surface Nanobubbles Studied by Time-Resolved Fluorescence Microscopy Methods Combined with AFM: The Impact

of Surface Treatment on Nanobubble Nucleation. *Langmuir* **2016**, *32*, 11155–11163.

(86) Kikuchi, K.; Nagata, S.; Tanaka, Y.; Saihara, Y.; Ogumi, Z. Characteristics of Hydrogen Nanobubbles in Solutions Obtained with Water Electrolysis. *J. Electroanal. Chem.* **2007**, *600*, 303–310.

(87) Kikuchi, K.; Takeda, H.; Rabolt, B.; Okaya, T.; Ogumi, Z.; Saihara, Y.; Noguchi, H. Hydrogen Particles and Supersaturation in Alkaline Water from an Alkali-Ion-Water Electrolyzer. *J. Electroanal. Chem.* **2001**, *506*, 22–27.

(88) Kikuchi, K.; Tanaka, Y.; Saihara, Y.; Maeda, M.; Kawamura, M.; Ogumi, Z. Concentration of Hydrogen Nanobubbles in Electrolyzed Water. *J. Colloid Interface Sci.* **2006**, *298*, 914–919.

(89) Postnikov, A. V.; Uvarov, I. V.; Penkov, N. V.; Svetovoy, V. B. Collective Behavior of Bulk Nanobubbles Produced by Alternating Polarity Electrolysis. *Nanoscale* **2018**, *10*, 428–435.

(90) Wang, Q.; Zhao, H.; Qi, N.; Qin, Y.; Zhang, X.; Li, Y. Generation and Stability of Size-Adjustable Bulk Nanobubbles Based on Periodic Pressure Change. *Sci. Rep.* **2019**, *9*.

(91) Mase, N.; Nishina, Y.; Isomura, S.; Sato, K.; Narumi, T.; Watanabe, N. Fine-Bubble-Based Strategy for the Palladium-Catalyzed Hydrogenation of Nitro Groups: Measurement of Ultrafine Bubbles in Organic Solvents. *Synlett* **2017**, *28*, 2184–2188.

(92) Oh, S. H.; Kim, J.-M. Generation and Stability of Bulk Nanobubbles. *Langmuir* **2017**, *33*, 3818–3823.

(93) Fang, Z.; Wang, L.; Wang, X.; Zhou, L.; Wang, S.; Zou, Z.; Tai, R.; Zhang, L.; Hu, J. Formation and Stability of Surface/Bulk Nanobubbles Produced by Decompression at Lower Gas Concentration. *J. Phys. Chem. C* **2018**, *122*, 22418–22423.

(94) Lou, S. T.; Ouyang, Z. Q.; Zhang, Y.; Li, X. J.; Hu, J.; Li, M. Q.; Yang, F. J. Nanobubbles on Solid Surface Imaged by Atomic Force Microscopy. *J. Vac. Sci. Technol. B* **2000**, *18*, 2573–2575.

(95) An, H.; Liu, G.; Atkin, R.; Craig, V. S. J. Surface Nanobubbles in Nonaqueous Media: Looking for Nanobubbles in DMSO, Formamide, Propylene Carbonate, Ethylammonium Nitrate, and Propylammonium Nitrate. *ACS Nano* **2015**, *9*, 7596–7607.

(96) Jin, F.; Li, J.; Ye, X.; Wu, C. Effects of PH and Ionic Strength on the Stability of Nanobubbles in Aqueous Solutions of α-Cyclodextrin. *J. Phys. Chem. B* **2007**, *111*, 11745–11749.

(97) Jin, F.; Ye, X.; Wu, C. Observation of Kinetic and Structural Scalings during Slow Coalescence of Nanobubbles in an Aqueous Solution. *J. Phys. Chem. B* **2007**, *111*, 13143–13146.

(98) Qiu, J.; Zou, Z.; Wang, S.; Wang, X.; Wang, L.; Dong, Y.; Zhao, H.; Zhang, L.; Hu, J. Formation and Stability of Bulk Nanobubbles Generated by Ethanol-Water Exchange. *ChemPhysChem* **2017**, *18*, 1345–1350.

(99) Millare, J. C.; Basilia, B. A. Nanobubbles from Ethanol-Water Mixtures: Generation and Solute Effects via Solvent Replacement Method. *ChemistrySelect* **2018**, *3*, 9268–9275.

(100) Millare, J. C.; Basilia, B. A. Dispersion and Electrokinetics of Scattered Objects in Ethanol-Water Mixtures. *Fluid Phase Equilib.* **2018**.

(101) Sedlák, M.; Rak, D. Large-Scale Inhomogeneities in Solutions of Low Molar Mass Compounds and Mixtures of Liquids: Supramolecular Structures or Nanobubbles? *J.*

Phys. Chem. B **2013**, *117*, 2495–2504.

(102) Uchida, T.; Liu, S.; Enari, M.; Oshita, S.; Yamazaki, K.; Gohara, K. Effect of NaCl on the Lifetime of Micro- and Nanobubbles. *Nanomaterials* **2016**, *6*, 31.

(103) Li, M.; Tonggu, L.; Zhan, X.; Mega, T. L.; Wang, L. Cryo-EM Visualization of Nanobubbles in Aqueous Solutions. *Langmuir* **2016**, *32*, 11111–11115.

(104) Bunkin, N. F.; Shkirin, A. V; Ignatiev, P. S.; Chaikov, L. L.; Burkhanov, I. S.; Starosvetskij, A. V. Nanobubble Clusters of Dissolved Gas in Aqueous Solutions of Electrolyte. I. Experimental Proof. *J. Chem. Phys.* **2012**, *137*, 054706.

(105) Burg, T. P.; Godin, M.; Knudsen, S. M.; Shen, W.; Carlson, G.; Foster, J. S.; Babcock, K.; Manalis, S. R. Weighing of Biomolecules, Single Cells and Single Nanoparticles in Fluid. *Nature* **2007**, *446*, 1066–1069.

(106) Nirmalkar, N.; Pacek, A. W.; Barigou, M. Interpreting the Interfacial and Colloidal Stability of Bulk Nanobubbles. *Soft Matter* **2018**, *14*, 9643–9656.

(107) Nirmalkar, N.; Pacek, A. W.; Barigou, M. Bulk Nanobubbles from Acoustically Cavitated Aqueous Organic Solvent Mixtures. *Langmuir* **2019**, *35*, 2188–2195.

(108) Johnson, B. D.; Cooke, R. C. Generation of Stabilized Microbubbles in Seawater. *Science (80-.).* **1981**, *213*, 209–211.

(109) Craig, V. S. J.; Ninham, B. W.; Pashley, R. M. The Effect of Electrolytes on Bubble Coalescence in Water. *J. Phys. Chem.* **1993**, *97*, 10192–10197.

(110) Craig, V. S. J.; Ninham, B. W.; Pashley, R. M. Effect of Electrolytes on Bubble Coalescence. *Nature* **1993**, *364*, 317–319.

(111) Henry, C. L.; Dalton, C. N.; Scruton, L.; Craig, V. S. J. Ion-Specific Coalescence of Bubbles in Mixed Electrolyte Solutions. *J. Phys. Chem. C* **2007**, *111*, 1015–1023.

(112) Yount, D. E.; Gillary, E. W.; Hoffman, D. C. A Microscopic Investigation of Bubble Formation Nuclei. *J. Acoust. Soc. Am.* **1984**, *76*, 1511–1521.

(113) Kim, C.; Qin, R.; Xu, J. S.; Wang, L. V.; Xu, R. Multifunctional Microbubbles and Nanobubbles for Photoacoustic and Ultrasound Imaging. *J. Biomed. Opt.* **2010**, *15*, 010510.

(114) Cai, W. B.; Yang, H. L.; Zhang, J.; Yin, J. K.; Yang, Y. L.; Yuan, L. J.; Zhang, L.; Duan, Y. Y. The Optimized Fabrication of Nanobubbles as Ultrasound Contrast Agents for Tumor Imaging. *Sci. Rep.* **2015**, *5*, 13725.

(115) Hernandez, C.; Abenojar, E.; Hadley, J.; de Leon, A.; Coyne, R.; Perera, R.; Gopalakrishnan, R.; Basilion, J. P.; Kolios, M.; Exner, A. Sink or Float? Characterization of Shell-Stabilized Bulk Nanobubbles Using Resonant Mass Measurement Technique. *Nanoscale* **2018**.

(116) Weijs, J. H.; Seddon, J. R. T.; Lohse, D. Diffusive Shielding Stabilizes Bulk Nanobubble Clusters. *ChemPhysChem* **2012**, *13*, 2197–2204.

(117) Yasui, K.; Tuziuti, T.; Kanematsu, W.; Kato, K. Dynamic Equilibrium Model for a Bulk Nanobubble and a Microbubble Partly Covered with Hydrophobic Material. *Langmuir* **2016**, *32*, 11101–11110.

(118) Parkinson, L.; Sedev, R.; Fornasiero, D.; Ralston, J. The Terminal Rise Velocity of 10–100 Mm Diameter Bubbles in Water. *J. Colloid Interface Sci.* **2008**, *322*, 168–172.

(119) Henry, C. L.; Parkinson, L.; Ralston, J. R.; Craig, V. S. J. A Mobile Gas-Water Interface in Electrolyte Solutions. *J. Phys. Chem. C* **2008**, *112*, 15094–15097.

(120) Li, T.; Kheifets, S.; Medellin, D.; Raizen, M. G. Measurement of the Instantaneous Velocity of a Brownian Particle. *Science* **2010**, *328*, 1673–1675.

(121) Perera, R. H.; Hernandez, C.; Zhou, H.; Kota, P.; Burke, A.; Exner, A. A. Ultrasound Imaging beyond the Vasculature with New Generation Contrast Agents. *Wiley Interdiscip. Rev. Nanomedicine Nanobiotechnology* **2015**, *7*, 593–608.

(122) Fan, X.; Wang, L.; Guo, Y.; Tong, H.; Li, L.; Ding, J.; Huang, H. Experimental Investigation of the Penetration of Ultrasound Nanobubbles in a Gastric Cancer Xenograft. *Nanotechnology* **2013**, *24*, 325102–325112.

(123) Zhang, X.; Liu, R.; Dai, Z. Multicolor Nanobubbles for FRET/Ultrasound Dual-Modal Contrast Imaging. *Nanoscale* **2018**, *10*, 20347–20353.

(124) Klibanov, A. L. Targeted Delivery of Gas-Filled Microspheres, Contrast Agents for Ultrasound Imaging. *Adv. Drug Deliv. Rev.* **1999**, *37*, 139–157.

(125) Klibanov, A. L. Ligand-Carrying Gas-Filled Microbubbles: Ultrasound Contrast Agents for Targeted Molecular Imaging. *Bioconjug. Chem.* **2004**, *16*, 9–17.

(126) Modi, K. K.; Jana, A.; Ghosh, S.; Watson, R.; Pahan, K. A Physically-Modified Saline Suppresses Neuronal Apoptosis, Attenuates Tau Phosphorylation and Protects Memory in an Animal Model of Alzheimer's Disease. *PLoS One* **2014**, *9*, e103606.

(127) Kalmes, A. A.; Ghosh, S.; Watson, R. L. A Saline-Based Theraputic Contaning Charge-Stabilized Nanostructures Protects Against Cardiac Ischemia/Reperfusion Injury. *J. Am. Coll. Cardiol.* **2013**, *61*, E106–E106.

(128) Mondal, S.; Martinson, J. A.; Ghosh, S.; Watson, R.; Pahan, K. Protection of Tregs, Suppression of Th1 and Th17 Cells, and Amelioration of Experimental Allergic Encephalomyelitis by a Physically-Modified Saline. *PLoS One* **2012**, *7*, e51869.

(129) Khasnavis, S.; Jana, A.; Roy, A.; Mazumder, M.; Bhushan, B.; Wood, T.; Ghosh, S.; Watson, R.; Pahan, K. Suppression of Nuclear Factor-KB Activation and Inflammation in Microglia by Physically Modified Saline. *J. Biol. Chem.* **2012**, *287*, 29529–29542.

(130) Choi, J. C.; Mega, T. L.; German, S.; Wood, A. B.; Watson, R. L. Electrokinetically Altered Normal Saline Modulates Ion Channel Activity. *Biophys. J.* **2012**, *102*, 683a.

(131) Ghosh, S.; Mega, T. L.; German, S.; Burke, L. M.; Diegel, M. L.; Wood, A. B.; Watson, R. L. Isotonic Saline Subjected to Taylor-Couette-Poiseuille Flow Demonstrates Anti-Inflammatory Activity in a Rat Model of Allergic Asthma. *J. Allergy Clin. Immunol.* **2011**, *127*, AB84–AB84.

(132) Mondal, S.; Ghosh, S.; Watson, R.; Pahan, K. RNS60, a Novel Therapeutic, Modifies T-Helper Cells and Inhibits Experimental Allergic Encephalomyelitis: Implications for Treating Multiple Sclerosis. *Neurology* **2012**, *78*, P05.116.

(133) Kalmes, A.; Ghosh, S.; Watson, R. Charge-Stabilized Nanostructures Reduce Ischemia-Reperfusion Injury in A Pig Model in Vivo. *Circulation* **2011**, *124*.

(134) Calgaroto, S.; Azevedo, A.; Rubio, J. Flotation of Quartz Particles Assisted by Nanobubbles. *Int. J. Miner. Process.* **2015**, *137*, 64–70.

(135) Ngai, T.; Xing, X.; Jin, F. Depletion Attraction between a Polystyrene Particle and a Hydrophilic Surface in a Pluronic Aqueous Solution. *Langmuir* **2008**, *24*, 13912–13917.

(136) Ghadimkhani, A.; Zhang, W.; Marhaba, T. Ceramic Membrane Defouling (Cleaning) by Air Nano Bubbles. *Chemosphere* **2016**, *146*, 379–384.

(137) Ushida, A.; Hasegawa, T.; Takahashi, N.; Nakajima, T.; Murao, S.; Narumi, T.;

Uchiyama, H. Effect of Mixed Nanobubble and Microbubble Liquids on the Washing Rate of Cloth in an Alternating Flow. *J. Surfactants Deterg.* **2012**, *15*, 695–702.

(138) Hassan, P. A.; Rana, S.; Verma, G. Making Sense of Brownian Motion: Colloid Characterization by Dynamic Light Scattering. *Langmuir* **2015**, *31*, 3–12.

(139) Podgoršak, E. B. (Ervin B. . Radiation Physics for Medical Physicists; 2006.

(140) Kerker, M. Scattering of Light and Other Electromagnetic Radiation; Elsevier Science, 2016.

(141) Bohren, C. F.; Huffman, D. R. Absorption and Scattering of Light by Small Particles; Wiley, 1983.

(142) Malloy, A.; Carr, B. NanoParticle Tracking Analysis - The Halo^{TM} System. *Part. Part. Syst. Charact.* **2006**, *23*, 197–204.

(143) Tixier, T.; Heppenstall-Butler, M.; Terentjev, E. M. Spontaneous Size Selection in Cholesteric and Nematic Emulsions. *Langmuir* **2006**, *22*, 2365–2370.

(144) Borm, P.; Klaessig, F. C.; Landry, T. D.; Moudgil, B.; Pauluhn, J.; Thomas, K.; Trottier, R.; Wood, S. Research Strategies for Safety Evaluation of Nanomaterials, Part V: Role of Dissolution in Biological Fate and Effects of Nanoscale Particles. *Toxicol. Sci.* **2006**, *90*, 23–32.

(145) Filipe, V.; Hawe, A.; Jiskoot, W. Critical Evaluation of Nanoparticle Tracking Analysis (NTA) by NanoSight for the Measurement of Nanoparticles and Protein Aggregates. *Pharm. Res.* **2010**, *27*, 796–810.

(146) Bhise, N. S.; Wahlin, K. J.; Zack, D. J.; Green, J. J. Evaluating the Potential of Poly(Beta-Amino Ester) Nanoparticles for Reprogramming Human Fibroblasts to Become Induced Pluripotent Stem Cells. *Int. J. Nanomedicine* **2013**, *8*, 4641–4658.

(147) Abdel-Hafez, S. M.; Hathout, R. M.; Sammour, O. A. Towards Better Modeling of Chitosan Nanoparticles Production: Screening Different Factors and Comparing Two Experimental Designs. *Int. J. Biol. Macromol.* **2014**, *64*, 334–340.

(148) Zhou, C.; Krueger, A. B.; Barnard, J. G.; Qi, W.; Carpenter, J. F. Characterization of Nanoparticle Tracking Analysis for Quantification and Sizing of Submicron Particles of Therapeutic Proteins. *J. Pharm. Sci.* **2015**, *104*, 2441–2450.

(149) Bai, S.; Murugesan, Y.; Vlasic, M.; Karpes, L. B.; Brader, M. L. Effects of Submicron Particles on Formation of Micron-Sized Particles During Long-Term Storage of an Interferon-Beta-1a Solution. *J. Pharm. Sci.* **2013**, *102*, 347–351.

(150) Ghonaim, H. M.; Li, S.; Blagbrough, I. S. N 1,N 12 -Diacyl Spermines: SAR Studies on Non-Viral Lipopolyamine Vectors for Plasmid DNA and SiRNA Formulation. *Pharm. Res.* **2010**, *27*, 17–29.

(151) Vallhov, H.; Gutzeit, C.; Johansson, S. M.; Nagy, N.; Paul, M.; Li, Q.; Friend, S.; George, T. C.; Klein, E.; Scheynius, A.; et al. Exosomes Containing Glycoprotein 350 Released by EBV-Transformed B Cells Selectively Target B Cells through CD21 and Block EBV Infection in Vitro. *J. Immunol.* **2011**, *186*, 73–82.

(152) Kittler, S.; Greulich, C.; Gebauer, J. S.; Diendorf, J.; Treuel, L.; Ruiz, L.; Gonzalez-Calbet, J. M.; Vallet-Regi, M.; Zellner, R.; Köller, M.; et al. The Influence of Proteins on the Dispersability and Cell-Biological Activity of Silver Nanoparticles. *J. Mater. Chem.* **2010**, *20*, 512–518.

(153) Montes-Burgos, I.; Walczyk, D.; Hole, P.; Smith, J.; Lynch, I.; Dawson, K.

Characterisation of Nanoparticle Size and State Prior to Nanotoxicological Studies. *J. Nanoparticle Res.* **2010**, *12*, 47–53.

(154) Kucherov, Y.; Hubler, G.; Michopoulos, J.; Johnson, B. Acoustic Waves Excited by Phonon Decay Govern the Fracture of Brittle Materials. *J. Appl. Phys.* **2012**, *111*, 023514.

(155) Hennart, S. L. A.; Hee, P. van; Wildeboer, W. J.; Meesters, G. M. H. Particle Size Characterization of an Extra Fine Milled Product. *Part. Part. Syst. Charact.* **2012**, *29*, 285–303.

(156) Khaydarov, R.; Khaydarov, R.; Gapurova, O.; Estrin, Y. A Novel Method of Continuous Fabrication of Aqueous Dispersions of Silver Nanoparticles. *Int. J. Nanoparticles* **2010**, *3*, 77.

(157) Hole, P.; Sillence, K.; Hannell, C.; Maguire, C. M.; Roesslein, M.; Suarez, G.; Capracotta, S.; Magdolenova, Z.; Horev-Azaria, L.; Dybowska, A.; et al. Interlaboratory Comparison of Size Measurements on Nanoparticles Using Nanoparticle Tracking Analysis (NTA). *J. Nanoparticle Res.* **2013**, *15*, 2101.

(158) Godin, M.; Bryan, A. K.; Burg, T. P.; Babcock, K.; Manalis, S. R. Measuring the Mass, Density, and Size of Particles and Cells Using a Suspended Microchannel Resonator. *Appl. Phys. Lett.* **2007**, *91*, 123121.

(159) Grover, W. H.; Bryan, A. K.; Diez-Silva, M.; Suresh, S.; Higgins, J. M.; Manalis, S. R. Measuring Single-Cell Density. *Proc. Natl. Acad. Sci. U. S. A.* **2011**, *108*, 10992–10996.

(160) Bryan, A. K.; Goranov, A.; Amon, A.; Manalis, S. R. Measurement of Mass, Density, and Volume during the Cell Cycle of Yeast. *Proc. Natl. Acad. Sci. U. S. A.* **2010**, *107*, 999–1004.

(161) Knudsen, S. M.; von Muhlen, M. G.; Manalis, S. R. Quantifying Particle Coatings Using High-Precision Mass Measurements. *Anal. Chem.* **2012**, *84*, 1240–1242.

(162) Patel, A. R.; Lau, D.; Liu, J. Quantification and Characterization of Micrometer and Submicrometer Subvisible Particles in Protein Therapeutics by Use of a Suspended Microchannel Resonator. *Anal. Chem.* **2012**, *84*, 6833–6840.

(163) Weinbuch, D.; Zölls, S.; Wiggenhorn, M.; Friess, W.; Winter, G.; Jiskoot, W.; Hawe, A. Micro–Flow Imaging and Resonant Mass Measurement (Archimedes) – Complementary Methods to Quantitatively Differentiate Protein Particles and Silicone Oil Droplets. *J. Pharm. Sci.* **2013**, *102*, 2152–2165.

(164) Kimoto, S.; Dick, W. D.; Syedain, Z.; Pui, D. Y. H.; Roberts, D. L. Effective Density of Silica Nanoparticle Size Standards. In *2014 International Aerosol Conference* ; Bustan, Korea, 2014.

(165) Maas, S. L. N.; de Vrij, J.; van der Vlist, E. J.; Geragousian, B.; van Bloois, L.; Mastrobattista, E.; Schiffelers, R. M.; Wauben, M. H. M.; Broekman, M. L. D.; Nolte-'t Hoen, E. N. M. Possibilities and Limitations of Current Technologies for Quantification of Biological Extracellular Vesicles and Synthetic Mimics. *J. Control. Release* **2015**, *200*, 87–96.

(166) Gross, J.; Sayle, S.; Karow, A. R.; Bakowsky, U.; Garidel, P. Nanoparticle Tracking Analysis of Particle Size and Concentration Detection in Suspensions of Polymer and Protein Samples: Influence of Experimental and Data Evaluation Parameters. *Eur. J. Pharm. Biopharm.* **2016**, *104*, 30–41.

(167) Tong, M.; Brown, O. S.; Stone, P. R.; Cree, L. M.; Chamley, L. W. Flow Speed Alters

the Apparent Size and Concentration of Particles Measured Using NanoSight Nanoparticle Tracking Analysis. *Placenta* **2016**, *38*, 29–32.

(168) Panchal, J.; Kotarek, J.; Marszal, E.; Topp, E. M. Analyzing Subvisible Particles in Protein Drug Products: A Comparison of Dynamic Light Scattering (DLS) and Resonant Mass Measurement (RMM). *AAPS J.* **2014**, *16*, 440–451.

(169) Sirsi, S.; Borden, M. Microbubble Compositions, Properties and Biomedical Applications. *Bubble Sci. Eng. Technol.* **2009**, *1*, 3–17.

(170) Yalkowsky, S. H.; Dannenfelser, R. M. Aquasol Database of Aqueous Solubility. *Coll. Pharmacy, Univ. Arizona, Tucson, AZ* **1992**.

(171) Krupka, T. M.; Solorio, L.; Wilson, R. E.; Wu, H.; Azar, N.; Exner, A. A. Formulation and Characterization of Echogenic Lipid-Pluronic Nanobubbles. *Mol. Pharm.* **2010**, *7*, 49–59.

(172) Gnyawali, V.; Moon, B.-U.; Kieda, J.; Karshafian, R.; Kolios, M. C.; Tsai, S. S. H. Honey, I Shrunk the Bubbles: Microfluidic Vacuum Shrinkage of Lipid-Stabilized Microbubbles. *Soft Matter* **2017**, *13*, 4011–4016.

(173) Duncan, P. B.; Needham, D. Test of the Epstein-Plesset Model for Gas Microparticle Dissolution in Aqueous Media: Effect of Surface Tension and Gas Undersaturation in Solution. *Langmuir* **2004**, *20*, 2567–2578.

(174) Brown, J. A. Physical Properties of Perfluoropropane. *J. Chem. Eng. Data* **1963**, *8*, 106–108.

(175) Mountford, P. A.; Sirsi, S. R.; Borden, M. A. Condensation Phase Diagrams for Lipid-Coated Perfluorobutane Microbubbles. *Langmuir* **2014**, *30*, 6209–6218.

(176) Crane, J. M.; Putz, G.; Hall, S. B. Persistence of Phase Coexistence in Disaturated Phosphatidylcholine Monolayers at High Surface Pressures. *Biophys. J.* **1999**, *77*, 3134–3143.

(177) Hernandez, C.; Lilly, J. L.; Nittayacharn, P.; Hadley, J.; Coyne, R.; Kolios, M.; Exner, A. A. Ultrasound Signal from Sub-Micron Lipid-Coated Bubbles. In *2017 IEEE International Ultrasonics Symposium (IUS)*; IEEE, 2017; pp 1–4.

(178) Folzer, E.; Khan, T. A.; Schmidt, R.; Finkler, C.; Huwyler, J.; Mahler, H.-C.; Koulov, A. V. Determination of the Density of Protein Particles Using a Suspended Microchannel Resonator. *J. Pharm. Sci.* **2015**, *104*, 4034–4040.

(179) Oettinger, D.; Ault, J. T.; Stone, H. A.; Haller, G. Invisible Anchors Trap Particles in Branching Junctions. *Phys. Rev. Lett.* **2018**, *121*, 054502.

(180) Yount, D. E.; Strauss, R. H. Bubble Formation in Gelatin: A Model for Decompression Sickness. *J. Appl. Phys.* **1976**, *47*, 5081–5089.

(181) Hemmingsen, E. A. Cavitation in Gas−supersaturated Solutions. *J. Appl. Phys.* **1975**, *46*, 213–218.

(182) Craig, V. S. J. Formation of Micronuclei Responsible for Decompression Sickness. *J. Colloid Interface Sci.* **1996**, *183*, 260–268.

(183) Beck, T. W.; Daniels, S.; Paton, W. D. M.; Smith, E. B. Detection of Bubbles in Decompression Sickness. *Nature* **1978**, *276*, 173–174.

(184) Helm, I.; Karina, G.; Jalukse, L.; Pagano, T.; Leito, I. Comparative Validation of Amperometric and Optical Analyzers of Dissolved Oxygen: A Case Study. *Environ. Monit. Assess.* **2018**, *190*, 313.

(185) Tuziuti, T.; Yasui, K.; Kanematsu, W. Influence of Increase in Static Pressure on Bulk Nanobubbles. *Ultrason. Sonochem.* **2017**, *38*, 347–350.

(186) Borkent, B. M.; Dammer, S. M.; Schönherr, H.; Vancso, G. J.; Lohse, D. Superstability of Surface Nanobubbles. *Phys. Rev. Lett.* **2007**, *98*, 204502.

(187) Brotchie, A.; Zhang, X. H. Response of Interfacial Nanobubbles to Ultrasound Irradiation. *Soft Matter* **2011**, *7*, 265–269.

(188) Berkelaar, R. P.; Dietrich, E.; Kip, G. A. M.; Kooij, E. S.; Zandvliet, H. J. W.; Lohse, D. Exposing Nanobubble-like Objects to a Degassed Environment. *Soft Matter* **2014**, *10*, 4947.

(189) Zhang, X. H.; Li, G.; Maeda, N.; Hu, J. Removal of Induced Nanobubbles from Water/Graphite Interfaces by Partial Degassing. *Langmuir* **2006**, *22*, 9238–9243.

(190) Vitale, S. A.; Katz, J. L. Liquid Droplet Dispersions Formed by Homogeneous Liquid-Liquid Nucleation: "The Ouzo Effect." *Langmuir* **2003**, *19*, 4105–4110.

(191) Khattab, I. S.; Bandarkar, F.; Fakhree, M. A. A.; Jouyban, A. Density, Viscosity, and Surface Tension of Water+ethanol Mixtures from 293 to 323K. *Korean J. Chem. Eng.* **2012**, *29*, 812–817.

(192) Alheshibri, M.; Craig, V. S. J. Differentiating Between Nanoparticles and Nanobubbles by Evaluation of the Compressibility and Density of Nanoparticles. *J. Phys. Chem. C* **2018**, *122*, 21998–22007.

(193) Sowa, B.; Zhang, X. H.; Kozielski, K.; Hartley, P. G.; Maeda, N. Influence of Dissolved Atmospheric Gases on the Spontaneous Emulsification of Alkane−Ethanol−Water Systems. *J. Phys. Chem. C* **2011**, *115*, 8768–8774.

(194) Chen, Q.; Luo, L.; Faraji, H.; Feldberg, S. W.; White, H. S. Electrochemical Measurements of Single H2 Nanobubble Nucleation and Stability at Pt Nanoelectrodes. *J. Phys. Chem. Lett.* **2014**, *5*, 3539–3544.

(195) Chen, Q.; Wiedenroth, H. S.; German, S. R.; White, H. S. Electrochemical Nucleation of Stable N2 Nanobubbles at Pt Nanoelectrodes. *J. Am. Chem. Soc.* **2015**, *137*, 12064–12069.

(196) Ren, H.; German, S. R.; Edwards, M. A.; Chen, Q.; White, H. S. Electrochemical Generation of Individual O2 Nanobubbles via H2O2 Oxidation. *J. Phys. Chem. Lett.* **2017**, *8*, 2450–2454.

(197) Aubry, J. M.; Cazin, B. Chemical Sources of Singlet Oxygen. 2. Quantitative Generation of Singlet Oxygen from Hydrogen Peroxide Disproportionation Catalyzed by Molybdate Ions. *Inorg. Chem.* **1988**, *27*, 2013–2014.

(198) Lide, D. R. CRC Handbook of Chemistry and Physics; CRC Press, 2006.

(199) Nguyen, D. A.; Iwaniw, M. A.; Fogler, H. S. Kinetics and Mechanism of the Reaction between Ammonium and Nitrite Ions: Experimental and Theoretical Studies. *Chem. Eng. Sci.* **2003**, *58*, 4351–4362.

(200) Kartnaller, V.; Romualdo, M. V.; Lobo, V. T. V.; Cajaiba, J. Kinetic Modeling of a Heat Generator for the Fluidization of Paraffin Deposits Using In-Line Infrared Spectroscopy with the Development of a Graphical User Interface. *Energy & Fuels* **2016**, *30*, 3660–3665.

(201) Battino, R.; Rettich, T. R.; Tominaga, T. The Solubility of Nitrogen and Air in Liquids. *J. Phys. Chem. Ref. Data* **1984**, *13*, 563–600.

(202) Diao, L.; Qin, J.; Zhao, N.; Shi, C.; Liu, E.; He, F.; Ma, L.; Li, J.; He, C. "Ethanol–Water Exchange" Nanobubbles Templated Hierarchical Hollow β-Mo $_2$ C/N-Doped Carbon Composite Nanospheres as an Efficient Hydrogen Evolution Electrocatalyst. *J. Mater. Chem. A* **2018**, *6*, 6054–6064.

(203) Xu, X.; Zhang, Z.; Wang, X. Well-Defined Metal-Organic-Framework Hollow Nanostructures for Catalytic Reactions Involving Gases. *Adv. Mater.* **2015**, *27*, 5365–5371.

(204) Joo, J. B.; Zhang, Q.; Dahl, M.; Zaera, F.; Yin, Y. Synthesis, Crystallinity Control, and Photocatalysis of Nanostructured Titanium Dioxide Shells. *J. Mater. Res.* **2013**, *28*, 362–368.

(205) Lai, X.; Halpert, J. E.; Wang, D. Recent Advances in Micro-/Nano-Structured Hollow Spheres for Energy Applications: From Simple to Complex Systems. *Energy Environ. Sci.* **2012**, *5*, 5604–5618.

(206) Yang, H.; Yin, Y. Shaping Nanostructures for Applications in Energy Conversion and Storage. *ChemSusChem* **2013**, *6*, 1781–1783.

(207) Luo, J.; Xia, X.; Luo, Y.; Guan, C.; Liu, J.; Qi, X.; Ng, C. F.; Yu, T.; Zhang, H.; Fan, H. J. Rationally Designed Hierarchical TiO2@Fe2O3 Hollow Nanostructures for Improved Lithium Ion Storage. *Adv. Energy Mater.* **2013**, *3*, 737–743.

(208) Jiang, Z.-J.; Jiang, Z. Fabrication of Nitrogen-Doped Holey Graphene Hollow Microspheres and Their Use as an Active Electrode Material for Lithium Ion Batteries. *ACS Appl. Mater. Interfaces* **2014**, *6*, 19082–19091.

(209) Ren, H.; Yu, R.; Wang, J.; Jin, Q.; Yang, M.; Mao, D.; Kisailus, D.; Zhao, H.; Wang, D. Multishelled TiO2 Hollow Microspheres as Anodes with Superior Reversible Capacity for Lithium Ion Batteries. *Nano Lett.* **2014**, *14*, 6679–6684.

(210) Xu, S.; Hessel, C. M.; Ren, H.; Yu, R.; Jin, Q.; Yang, M.; Zhao, H.; Wang, D. α-Fe2O3 Multi-Shelled Hollow Microspheres for Lithium Ion Battery Anodes with Superior Capacity and Charge Retention. *Energy Environ. Sci.* **2014**, *7*, 632–637.

(211) Wang, L.; Lou, Z.; Fei, T.; Zhang, T. Zinc Oxide Core–Shell Hollow Microspheres with Multi-Shelled Architecture for Gas Sensor Applications. *J. Mater. Chem.* **2011**, *21*, 19331.

(212) Wang, Y.; Wang, G.; Wang, H.; Liang, C.; Cai, W.; Zhang, L. Chemical-Template Synthesis of Micro/Nanoscale Magnesium Silicate Hollow Spheres for Waste-Water Treatment. *Chem. - A Eur. J.* **2010**, *16*, 3497–3503.

(213) Kim, S.-C.; Lee, D.-K. Preparation of TiO2-Coated Hollow Glass Beads and Their Application to the Control of Algal Growth in Eutrophic Water. *Microchem. J.* **2005**, *80*, 227–232.

(214) Wang, X.; Feng, J.; Bai, Y.; Zhang, Q.; Yin, Y. Synthesis, Properties, and Applications of Hollow Micro-/Nanostructures. *Chem. Rev.* **2016**, *116*, 10983–11060.

(215) Pashley, R. M.; Karaman, M. E. Applied Colloid and Surface Chemistry; John Wiley & Sons, Ltd: Chichester, UK, 2004.

(216) Gennes, P.-G. de.; Brochard-Wyart, F.; Quéré, D. Capillarity and Wetting Phenomena : Drops, Bubbles, Pearls, Waves; Springer, 2004.

(217) Montgomery, D. C.; Runger, G. C. Applied Statistics and Probability for Engineers; Wiley, 2011.

Appendix

A.1 Derivation of the Laplace Law for a spherical bubble

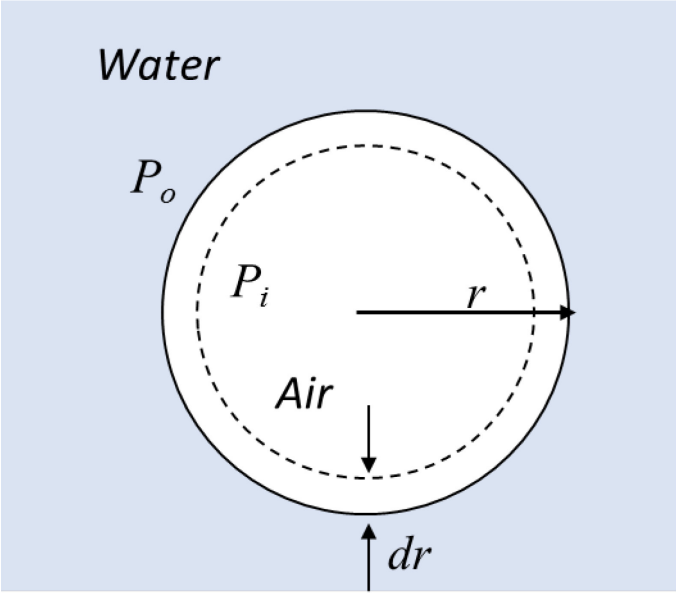

Figure A.1. Schematic of an air bubble submerged in water. The bubble radius is r, the pressure outside the bubble is P_o and the pressure inside the bubble is P_i. A change in bubble radius dr will lead to a change in both volume and surface area.

Consider a stable air bubble formed in water with radius r (see Figure A.1). At equilibrium, a infinitesimal change in radius (*dr)* leads to no change in the free energy (*dG)*.

Now let us assume a small decrease in radius dr. The surface energy of the system will be decreased by the reduction in surface area of the bubble. At equilibrium this is balanced by increasing the pressure inside the bubble. Therefore, the bubble will obtain an equilibrium when the free energy gained due to a reduced surface area δW_S is balanced by the work done against pressure difference, δW_P. The change in free energy of the system at equilibrium is then

described by the sum of the decrease in work corresponding to the interfacial area, δW_S, and the work done against the pressure difference[215] δW_P. The formula is given in Equation A.2:

$$dG = -\delta W_S + \delta W_P \quad \text{(A.1)}$$

The part of the work corresponding to the interfacial area δW_S is

$$\delta W_S = \gamma dA \quad \text{(A.2)}$$

A here is the surface area of a sphere ($4\pi r^2$), and the change in the surface area for a bubble shrinking by an infinitesimal dr is described by

$$dA = 8\pi r dr \quad \text{(A.3)}$$

Substituting the values for dA in equation A.2 leads to:

$$\delta W_S = 8\pi r dr \gamma \quad \text{(A.4)}$$

To obtain δW_P, a basic thermodynamic definition of pressure - volume (PV) work is

$$\delta W_P = PdV \quad \text{(A.5)}$$

Here the component of the work inside and outside the bubble respectively are

$$\delta W_{Pi} = P_i dV_i \quad \text{(A.6)}$$

And

$$\delta W_{Po} = P_o dV_o \quad \text{(A.7)}$$

The change of internal volume dV_i is equal to the change of external volume dV_o but opposite in sign

$$dV_i = -dV_o = dV \quad \text{(A.8)}$$

Thus

$$\delta W_P = P_i dV_i + P_o dV_o = \Delta P dV \quad \text{(A.9)}$$

From the geometry for a sphere

$$\frac{dV}{dr} = 4\pi r^2 \tag{A.10}$$

Rearranging

$$dV = 4\pi r^2 dr \tag{A11}$$

The combination of equation A.9 and A.11 leads to

$$\delta W_P = \Delta P 4\pi r^2 dr \tag{A.12}$$

Substituting the equations (A.4) and (A.12) into equation A.1, leads to:

$$dG = -8\pi r dr\gamma + \Delta P 4\pi r^2 dr \tag{A.13}$$

At equilibrium,

$$\frac{dG}{dr} = 0 \tag{A.14}$$

Thus

$$(\Delta P)4\pi r^2 = 8\pi\gamma r \tag{A.15}$$

$$\Delta P = \frac{2\gamma}{r} \tag{A.16}$$

Equation A.16 is the Laplace equation for a single spherical interface. The derivation described above is a simple derivation of Laplace law for a sphere[215,216], as this study only consider spherical bubbles. Laplace laws for other curved surfaces are reported by De Gennes *et al*. [40]

A.2 Armoured nanobubbles under pressure

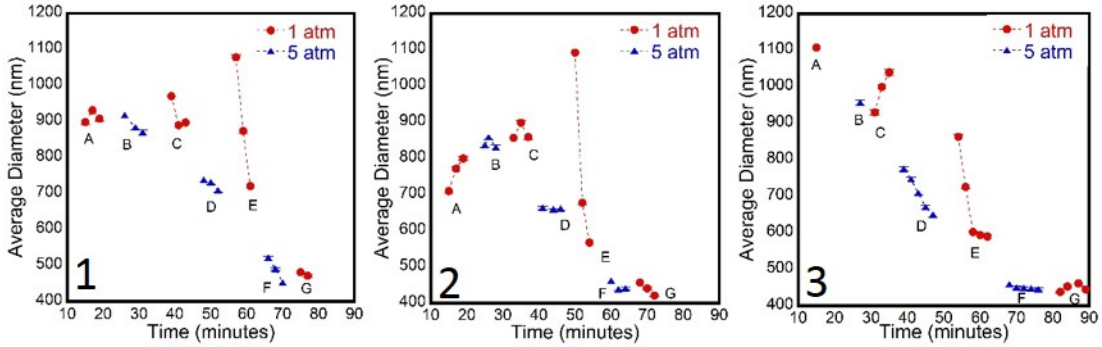

Figure A.2. Measurements demonstrating the effect of pressure cycling between an external pressure of 1.0 atm and 5.0 ± 0.1 atm on the diameter of lipid coated nanobubbles using dynamic light scattering in the presence of other nanoparticles. The red points and the blue points represent the average diameter measured at 1.0 atmosphere and 5.0 atmospheres of pressure respectively. Each point represents a single measurement as the change in size was relatively fast when depressurizing the sample. The error bars shown are for 1 standard deviation calculated from the average of the relative standard deviation of all the data shown in Figure 3-3.

A.3 Determination of the error in the Intercept and slope

The standard error in the determination of the intercept and the slope from linear regression was used to calculate the 95% confidence interval[217] when determining the density of nanoparticles by extrapolation/interpolation.

$$\text{Error} = \text{b} \pm t_{\alpha/2,\text{n}-2}\, \text{S}_{eb} \qquad \text{(A.17)}$$

Where b is the estimate of the intercept, $t_{\alpha/2,n-2}$ is the t distribution with $\alpha = 0.05$ for a 95% confidence interval, n-2 is the degrees of freedom, where n is the number of data points, and S_{eb} is the standard error of the estimate.